UNIVERSITY OF OKLAHOMA

GRADUATE COLLEGE

MECHANISMS AND RATES OF STRENGTH RECOVERY IN LABORATORY FAULT ZONES

A Dissertation

SUBMITTED TO THE GRADUATE FACULTY

in partial fulfillment of the requirements for the

degree of

Doctor of Philosophy

By

SANKAR KUMAR MUHURI
Norman, Oklahoma
2001

UMI Number: 3028811

UMI®

UMI Microform 3028811

Bell & Howell Information and Learning Company
300 North Zeeb Road
P.O. Box 1346
Ann Arbor, MI 48106-1346

MECHANISMS AND RATES OF STRENGTH RECOVERY IN LABORATORY FAULT ZONES

A Dissertation APPROVED FOR THE SCHOOL OF GEOLOGY AND GEOPHYSICS

BY

ACKNOWLEDGEMENTS

I am thankful for the advice, guidance and collaboration of my thesis advisor Dr. Thomas A. Dewers. His scientific curiosity and attitude resulted in pursuit on my part of certain aspects of the study that I would otherwise never embark upon. Indeed, without his encouragement and motivation during the not so bright times this study may not have been completed in quite the same way.

I wish to thank Dr. Thurman E. Scott (Jr.) for his support during my research and the numerous brain-storming sessions related to advanced techniques and instrumentation in rock mechanics and interpretation of results. I am also grateful for the encouragement and expert suggestions provided by Dr. Ze'ev Reches from thousands of miles away. His patient help during writing parts of the study is much appreciated. Dr. Scott and Dr. Reches were both active members of my Ph.D. Committee and their many tangible and intangible opinions and ideas helped immensely.

Thanks also to Dr. Judson Ahern for being part of my advisory committee and for his constructive criticisms about earlier versions of parts of this document. Thanks to Dr. Jean-Claude Roegiers and Dr. Douglas Elmore for their time, suggestions and for being a part of the committee.

I am very appreciative of the financial support of my Doctoral program by the Rock Mechanics Institute (RMI) and the member companies that were a part of the Oklahoma University Rock Mechanics Consortium, the School of Geology and Geophysics for providing me with financial support and for the opportunity to teach and travel to professional meetings. Thanks to Phillips Petroleum Co. for a fellowship during my Ph.D. studies and to Geological Society of America, OU Graduate College and the UOSA for student research grants. Parts of the research were funded by the National Science Foundation, Petroleum Research Funds administered by the American Chemical Society, and the United States Geological Survey under the National Earthquake Hazards Reduction Program through grants to Dr. Tom Dewers.

Many other people contributed to this research through discussions, suggestions, and help in running instruments. Thanks to Dr. Dave Stearns for numerous discussions on this research, a variety of topics in structural geology and outside of it. I remain indebted to Pete Keller, Brian Silver and John Brumley for their help at the OU RMI laboratory. Bill Chissoe and Dr. George Morgan for help with electron microscopy. My special thanks to Donna Mullins for all her support during my years at this University.

I wish to dedicate this work to my parents for their many sacrifices, moral support during my education. I wish to thank my many friends, relatives and teachers both here in the US and in India without whom my life may not have been the same. Lastly, I would like to thank Satavisa, my soul mate without her presence this would not have been enjoyable or even possible.

TABLE OF CONTENTS

LIST OF TABLES

LIST OF FIGURES

ABSTRACT

The life cycle of a typical fault zone consists of repeated catastrophic seismic events during which much of the slip is accommodated interspersed with creep during the inter-seismic cycle. Fault strength is regenerated during this period as a result of several time-dependent, fluid assisted deformation mechanisms that are favored by high stresses along active fault zones. The strengthening is thought to be a function of the sum total of the rates of recovery due to these multiple creep processes as well as the rate of tectonic loading.

Mechanisms and rates of strength recovery in laboratory fault zones were investigated in this research with the aid of several experimental designs. It was observed that wet faults recover strength in a time-dependent manner after slip due to operative creep processes. Subsequent loading results in unstable failure of a cohesive gouge zone with large associated stress drops. The failure process is similar to that observed for intact rocks. Dry laboratory faults in contrast do not recover strength and slip along them is always stable with no observable drop in stress.

Strengthening in laboratory faults proceeds in a manner that is a logarithmic function of time. The recovery is attributable to fluid mediated mechanisms such as pressure solution, crack sealing and Ostwald ripening that collectively cause a reduction in porosity and enhance lithification of an

unconsolidated gouge. Rates for the individual deformation mechanisms investigated in separate experimental setups were also observed to be a non-linear function of time. Pressure solution and Ostwald ripening are especially enhanced due to the significant volume fraction of fine particles within the gouge created due to cataclasis during slip.

The results of this investigation may be applied to explain observations of rapid strengthening along large, active crustal fault zones such as parts of the San Andreas Fault system in California and the Nojima fault in Japan. Presence of fault seals in clean hydrocarbon reservoirs with minor clay content as in several North Sea fields may also be a manifestation of similar deformation processes.

Chapter 1

Introduction, objectives and evidence for fault strengthening

Introduction

Fault zone dynamics are generally cast in terms of mechanical processes such as cataclasis (grain comminution) and compaction. Popular earthquake models over the past 20 years have stemmed from an extensive laboratory research program where the frictional properties of artificial faults have been determined from short-term experiments mostly performed at room temperature. The understanding derived from these experiments has resulted in the rate- and state- variable friction constitutive relationship that has dominated thinking on the mechanisms of fault reactivation (earthquake source mechanics). A dominant part of this work was performed with bare rock surfaces, at room temperature, and over limited time duration (minutes to hours). In nature, on the other hand, fault reactivation occurs at depths and elevated temperatures, fault surfaces are usually coated with rock flour (fault gouge), and the slip characteristics change over a wide range of time scales. Central to the issue of fault reactivation is the mechanical role of fault gouge that accommodates the displacement on the fault. Some authors have recently alluded to the role of thermally activated chemical processes such as pressure solution, Ostwald ripening, cementation, and microfracture healing in dictating the mechanical strength of fault zones as well as their hydrological properties. In addition, numerous field studies on exhumed fault zones, mines and borehole data point to the operation of the above chemical processes in tandem with mechanical processes such as cataclasis. The fine-grained nature of most fault gouge suggests presence of an extremely reactive chemical system in the presence of suitable fluids that may alter friction. It is thus necessary to study the deformation of fault gouge in the presence of reactive fluids to get a realistic picture for the various operative mechanisms and their roles in fault reactivation.

Objectives

The primary objectives of this study are to investigate (a) how faults in the laboratory regain strength or heal due to operative time-dependent chemical processes in the gouge zone, (b) the permeability evolution of laboratory faults in time, (c) evolution of particle size distribution (PSD) in time, and (d) time-dependent mechanisms that may lead to mechanical strength recovery, permeability and textural evolution. Secondary objectives will include development of constitutive relationships for creep in common mineral-water systems, comparison with published data, and a preliminary investigation of Ostwald ripening as a potential mechanism for healing and sealing of fault zones.

The development of these objectives will be undertaken in the following chapters that have been prepared as individual articles. Chapter 1 (current chapter) presents an overview of the healing mechanisms and strength of crustal faults, present experimental knowledge from previous work, and evidences for healing of faults in both experiments and nature.

In chapter 2 the time–dependent creep in 4 minerals viz. quartz, calcite, gypsum and halite is investigated, comparing data in the literature with experimental data from this study. An effort is made to emphasize the phenomenological similarities in these minerals that have widely different chemical compositions, crystal structure and physical properties.

This sets the stage for chapter 3 where gypsum has been used as the fault gouge material in long-term, cyclic (hold-slide-hold) loading experiments spanning up to couple of months. It is illustrated that fault reactivation is characterized by an increase in strength during consecutive loading periods and that this re-strengthening only occurs in the presence of water due to diverse healing (lithification) processes such as pressure solution and grain contact welding, cementation and recrystallization via Ostwald ripening, crack sealing etc.

Chapter 4 addresses the issue of fault sealing especially in relatively clean sandy reservoirs. The close relationship between fault strength recovery and the evolution of porosity and permeability is illustrated. The potential for development of fault seals from generation of cement within the fault zone is addressed.

Chapter 5 deals with the evolution of particle size distribution (PSD) during shear and post-slip hold periods in relatively short-term (few minutes to ten hours) experiments. The evolution of PSD parameters such as mean, spread, skewness and fractal dimension are investigated and attention is drawn at the contrasting characteristics in evolution of such parameters during shear (time independent deformation) and during periods of quiescence (creep).

The subject of investigation in chapter 6 is compaction creep of granular calcite aggregates over a range of extrinsic (effective pressure, temperature) and intrinsic (grain size) parameters. Creep is important in the evolution of fault zones and several mechanisms such as pressure solution and or fracturing (time-dependent?), crack healing, and Ostwald ripening may operate in tandem during creep. An effort is made to characterize the conditions over which specific creep mechanisms dominate overall behavior.

Background

Friction, gouge, and earthquakes

Slip on a pre-existing fault occurs when the shear stress (τ) equals the product of the normal stress (σ) and the coefficient of static friction (μ). This rather simple model arises from a linear Coulomb failure criterion assuming negligible cohesion. The popular stick-slip model of earthquakes (spring-slider block system) invokes slip with stress drops separated by periods of quiescence (Bridgeman, 1936, 1951; Brace and Byerlee, 1966). Friction on the fault is thought to govern the stick-slip motion. Considerable attention has thus been devoted to the measurement of the coefficient of friction μ under simulated conditions in the laboratory. Slip velocity, fault surface roughness, gouge properties (particle size distribution, degree of consolidation), normal stress, and shear strain all affect friction coefficient μ (Dieterich, 1979, 1992; Byerlee et al., 1978; Marone et al., 1990; Fredrich and Evans, 1992; Marone and Kilgore, 1993). Frictional sliding experiments on bare rock against rock surfaces, or those separated by a layer of granular gouge, have attempted to measure changes in static friction with change in slip velocity in slide-hold-slide type experiments (Dieterich, 1979, 1992; Ruina, 1983). The coefficient of static friction μ is found to obey an empirical form that is logarithmic with time of contact (Dieterich, 1979). The rate- and state- variable friction model grew from this body of work. In this model, the instantaneous increase in μ due to an increase in slip velocity is termed '*a*' parameter, this is followed by a decrease in μ to a new steady state value that is the '*b*' parameter and the distance over which this new value is achieved is the characteristic displacement or d_c. The results, though reproducible in various laboratories and in different experimental procedures (double direct shear, rotary shear, triaxial), produced about 5% change in friction value per decade of hold time (Cao and Aki, 1986; Karner et al., 1997). However, estimates of seismic stress drops increase by factor of 2-5 per decade increase in earthquake recurrence interval (Sammis and Steacy, 1994). Reasons for this discrepancy have been attributed to a greater degree of roughness in natural faults (Sammis and Steacy, 1994), presence of a granular fault gouge (Sammis et al., 1986; An and Sammis, 1994), and action of thermally activated, fluid mediated chemical processes that may alter frictional properties of gouge over geologic time (Fredrich and Evans, 1992).

Several workers have attempted sliding friction experiments under hydrothermal conditions (Chester and Higgs, 1992; Fredrich and Evans, 1992; Blanpied et al., 1991, Karner et al., 1997; Olsen et al., 1998). The frictional strength in these experiments reveals complex behavior, *e.g.* Chester and Higgs (1992) noted increasing strength and velocity weakening (decrease in μ with increase in velocity) from 23-300°C and slightly decreasing strength from 300-600°C. In contrast, Fredrich and Evans (1992) noted an increase in strength with both hold time and temperature. Karner et al., (1997) reported no time-dependent strength increase for experiments deformed and healed at high temperatures (636°C). These experiments however, were conducted at elevated temperatures generally higher than typical seismogenic zones where different kinetic mechanisms may be dominant. This may explain some of the apparently conflicting observations between the above studies. Olsen et al., (1998) show healing of gouge accompanied by an increase in strength and decrease in permeability in experiments on mixed feldspar-quartz gouge under triaxial conditions over period of four days. The healing according to these workers is due to the precipitation of clay minerals and consequent permeability reduction, similar to observations on natural fault zones (Chester et al., 1993).

Some important deformation mechanisms

Cataclasis and Particle Size Distribution (PSD)

Cataclasis, a common deformation mechanism involves both rigid body motions and grain comminution. The mechanism of cataclasis in the upper crust leads to formation of fault gouge. Cataclasis also occurs along with recrystallization and neomineralization at greater depths. The close association of faulting and cataclasis has led to numerous studies of both natural and experimental fault zones (Engelder, 1974; Sibson, 1979; Logan, 1981; Robertson, 1983; Rutter et al., 1986; Sammis et al., 1986 and 1987; Logan and Teufel, 1986; Chester and Logan, 1986; Power et al., 1988; Biegel et al., 1989; Marone and Scholz, 1989; Scholz, 1990; Chester et al, 1993). Gouge is mostly restricted to one or more sub parallel to oblique sheet-like forms that are sites of localized slip within larger shear (fault) zones (Chester and Logan, 1986 and 1987). Cataclastic gouge zones are an intrinsic part of faulting of intact rocks and subsequent slip along fractures (Aydin and Johnson, 1982; Lockner et al., 1992), as also slip along precut surfaces (Logan and Teufel, 1986). Frictional sliding or slip along faults leads to an increased degree of grain comminution and thickening of gouge zones (Robertson, 1983; Wallace and Morris, 1986; Scholz, 1990). Thickening of the gouge zone is assumed to reflect accumulated wear of the host blocks (Marone and Scholz, 1989; Scholz, 1990). A fault zone may exhibit a foliated or zoned structure with progressively greater degree of comminution towards the fault core with a layer of ultracataclasite indicating extreme slip localization (Chester and Logan, 1986 and 1987; Chester et al., 1993).

Fault gouge is poorly sorted and may range in particle size from coarse boulder to fine silt or clay (Rutter et al., 1986; Sammis et al., 1987). Both experimental and natural fault gouge occurring in crystalline rocks exhibit a fractal or power-law PSD especially for the finer gouge fraction (Sammis et al., 1987). Fractal dimension for both natural and experimental gouge zones has been observed to be around 2.6 (Sammis et al., 1987; Biegel et al., 1989). In order to explain the observed fractal distribution Sammis et al. (1987), proposed a model where fractures in dense aggregates are most likely when neighboring particles are similar in size. Fault rocks that often exhibit preserved isolated large fragments floating inside a fine-grained matrix tend to favor the above (An and Sammis, 1994; Hadizadeh, 1994; Kennedy and Logan, 1997). Yet another grain comminution model invokes that fracturing is largely independent of size except for a grinding limit at which the probability of further breakage is reduced (An and Sammis, 1994). Experimental gouge zones with large shear strains ($\gamma >$ 1.5, shear strain γ, is the resolved displacement along the experimental fault plane divided by the initial gouge thickness) do not exhibit a power-law distribution, and PSD attains a steady state with onset of shear localization. However, at lower shear strains ($\gamma < 1.3$) PSD follows a fractal distribution (Marone and Scholz, 1989).

The micromechanical model for friction focuses on surface asperities of faults. However, fault surfaces are always covered with powdered rock flour or gouge. Laboratory studies indicate that sliding behavior may be related to soil-like behavior of gouge. By analogy to soil-mechanics tests, a direct relationship between the upper fractal limit of gouge and the characteristic displacement parameter has been proposed (Sammis and Biegel, 1989). The coefficient of friction, μ shows an apparent inverse relationship with gouge thickness in experiments. For rough fault surfaces γ is larger and dependent on PSD. The transient parameter *a*, is also markedly larger (about 3 times) for rough fault surfaces compared to smoother fault surfaces (Biegel et al., 1989; Marone et al., 1990). These differences are interpreted to be result of a homogeneous distribution of strain across the gouge layer as evidenced by lack of Reidel shear like structures when the fault surfaces are rough. Generation of a power-law type PSD reduces probability of further fracturing, as grains are likely to be surrounded by dissimilar sizes. This causes evolution from fracture (dilatancy) to slip or from velocity strengthening to weakening (Biegel et al., 1989). Higher strain rates promote dilatancy that could account for creation of porosity during seismic events while lower strain rates induces compaction in experimental gouge (Morrow and Byerlee, 1989).

Pressure Solution

Pressure Solution (also solution-transfer creep) which may also include processes such as free face dissolution, water-film diffusion, stress corrosion cracking and crack healing has been held responsible for driving compactional porosity loss in sedimentary basins (Houseknecht, 1988; Tada and Siever, 1989; Spiers and Schutjens, 1990; Dewers and Hajash, 1995; among others) and fault zones (Sleep, 1995; Sleep and Blanpied, 1992). Pressure solution is thought to be important in driving formation of spatially organized over-pressured compartments in fault zones (Sleep, 1995; Byerlee, 1993; Rice, 1992). Genesis of stylolites and clay seams have also been attributed to solution-transfer mechanism (Heald, 1955; Dewers and Ortoleva, 1994). Pressure solution textures are ubiquitous in sediments and have been commonly noticed in fault zone rocks (Chester and Logan, 1986; Fredrich and Evans, 1992). Two basic hypotheses usually argued are the Weyl (1959) and the Bathurst (1958) treatises. These differ in the thermodynamic driving forces as well as the rate-limiting kinetic mechanisms that combine to yield creep rates. The Water Film Diffusion Model (Tada et al., 1987) addresses back to the Weyl theory where the driving force is the normal stress at grain contacts separated by a thin film of water having properties essentially similar to bound water in lattice structures. The kinetic rate-limiting step in this model is diffusive mass transfer. The Free Face Pressure Solution Model (Tada et al., 1987) on the other hand is driven by dislocation strain energy or elastic strain energy (prior to yielding) and the kinetics is controlled by reaction or diffusion through the pore fluid. Experimental evidence suggests that both processes are active in nature (Tada and Siever, 1986; Hickman and Evans, 1991; Dewers and Hajash, 1995). In fault zones the complexity is increased by evolution of rock textures that may result in a shift in the dominant mechanism of pressure solution.

Ostwald Ripening

Surface tension forces become an important driving force for very small particles or particles with a high surface area to mass ratio and play a role in diagenesis and crack healing (Maliva and Siever, 1988; Morse and Casey, 1988; Steefel and Van Capellen, 1990; Dove, 1995). As finer sized particles are more soluble than their coarser counterparts fluid-particle interaction coupled with diffusion can cause coarser particles to further grow at the expense of finer ones. Grain crushing experiments conducted by Dewers and Hajash (1995), with quartz show an almost instantaneous increase in silica concentration following crushing that quickly decreased to background concentration levels over time scale of days. Fault gouge containing a distribution of particles from sub-micron to boulder size is susceptible to chemical ripening wherein smaller particles dissolve and are a potential source of cement or overgrowths on larger grains. This may be important immediately after slip with the large proportion of fine particles serving as a source for rapid cementation. Very little information is available on Ostwald ripening in fault zones but few workers have tried to address its potential relevance (Sleep, 1995). In fault zone cores with narrow and highly granulated shear zones embedded in a fractured (but not granulated) damage zone, Ostwald ripening may drive mass transfer from the finer-grained fault zone core to the coarser damage zone.

Evidence of Healing in Experimental Faults

Quartz powder was sheared between Sioux quartzite sliding blocks in a series of hydrothermal, triaxial experiments at elevated temperatures (230-636°C) and pressures (confining pressure of 250 MPa and pore water pressure of 75 MPa) by Karner et al. (1997). These experiments were initially "held" under hydrostatic pressure for a period of time (several hours) at elevated temperatures followed by shearing. Observable strengthening occurred in experiments that were healed at elevated temperature (636°C) and then sheared at lower temperature (230°C). Several experiments showed a stress drop suggesting unstable failure of the gouge at peak strength. Experiments that were healed at lower temperature (230°C) and subsequently sheared exhibited no marked strengthening. Frictional strengthening rates of 0.1 per decade change in healing time was obtained and attributed to lithification processes possibly due to pressure solution mechanisms. Samples that were healed and then deformed at the higher temperature (636°C) showed lower absolute strengths as well as no time-dependent healing. A frictional weakening however was observed for experiments that were healed under shear (triaxial) loading. According to the authors alternate shear and healing (cyclic or hold-slide-hold loading) inhibits lithification and frictional strengthening.

Similar experiments were run using quartzo-feldspathic gouge (mixture of 90% labradorite and 10% quartz) and stainless steel slider blocks by Olsen et al. (1998). Experiments were run mostly at 250°C and an effective pressure of 50 MPa (confining pressure of 60 MPa and pore pressure of 10 MPa).

Experiments were loaded to a stable sliding behavior and then healed (hold) for a period of 2 days at reduced levels of axial load. During the hold periods the pore fluid was cycled continuously for permeability measurements by the steady-state method. As a result of the high proportion of feldspar and its breakdown to clays at elevated temperature during healing an increase in frictional strength was observed. The amount of strengthening was commensurate with the amount of sealing or reduction in permeability. Permeability reduction due to precipitation of clay minerals was noted to be faster initially. A dependency of increase in frictional strength on the hold periods was not observed in these experiments. Interestingly, though an increase in frictional strength (sliding friction strength) was noted in these experiments no unstable failure or stress drop was observable. The authors suggested that the mechanism of "precipitation-sealing" may explain the under-prediction of laboratory estimates of healing based on dry friction laws relative to natural faults. Furthermore, they were of the view that such a mechanism may preserve abnormally high pore fluid pressures within fault gouge zones.

More recently, Bos et al. (2001, 2000) conducted rotary shear, cyclic loading (slide-hold-slide) experiments using halite and kaolinite mixtures in varying proportions. The experiments were done at room temperature and atmospheric pore pressure under drained conditions. Halite in these experiments was chosen as an analogue to experimentally model fault rheology at conditions simulating the brittle-ductile transition. The kinetics of halite-water chemical reaction is well constrained. The experimental conditions were chosen so that pressure solution and cataclasis dominate over dislocation creep mechanisms. Healing or increase in shear strength of the synthetic gouge zones was observed. The authors also noted slip instability and an abrupt reduction in fault strength on reaching the peak strength. This behavior was confined to gouge mixtures that had very little or no kaolinite and also to experiments using a reactive pore fluid (brine). An increase in the amount of kaolinite appeared to promote stable sliding along the gouge zone similar to observations by Olsen et al. (1998) described previously. The strengthening in experimental fault zones was attributed to pressure solution in samples that were devoid of clays or had small amount of the same. The microstructures suggested shear along kaolinite foliation planes as well as pressure solution and cataclasis. Apparently, an excess of clay minerals inhibit pressure solution by significantly reducing halite-halite grain contacts. As clay minerals are ubiquitous in fault zones the authors raise questions about the usefulness of laboratory-derived healing data from monomineralic fault gouge for modeling crustal dynamics.

Evidence of Healing in Crustal Faults

Various authors have presented evidence for re-strengthening or healing of crustal faults recently. Time-lapse seismic surveys of the Landers fault ruptured during the magnitude (M) 7.5 event of 1992 reveal an increase in the seismic velocity with time (Li et al., 1998). During this study P, S, and fault zone "trapped" or guided waves were excited by near-surface sources in 1994 and

1996. The data was recorded on a three-component geophone array located across the surface trace of the Johnson Valley fault. Increase in both the P and S wave velocity has been observed to the tune of 0.5 - 1.5% for identical shot-receiver pairs in the period between 1994 and 1996. This reduction in velocity has been argued to be the result of an approximately 1% reduction in the number of cracks over this time interval.

A different form of data presented by Massonnet et al. (1994) using InSAR interferometry to detect evidence of time-dependent closure of fractures after the Landers 1992 earthquake led to a similar observation. They used two different radar images taken a month after and a year after the Landers event and noted 30 cm of fault-normal collapse during this time interval. The collapse was interpreted as indicating post-earthquake closure of cracks that dilated during the seismic event or immediately prior to it.

Repeated S-wave splitting (birefringence) surveys were conducted along the Nojima fault that ruptured during the 1995 Hyog-ken Nanbu (M) 7.2 earthquake (also known as the Kobe earthquake) by Tadokoro et al. (1999). The magnitude of S-wave anisotropy or splitting in various azimuths is an index of the intensity and orientation of fractures present in the rock volume. The data can be recast as rose-diagrams for depicting fracture orientations. Time-lapse measurements of S-wave birefringence over a period of 33 months reveal near complete healing of shear fractures adjacent to the Nojima fault that were opened during the earthquake (Tadokoro et al., 1999; Tadokoro and Ando, 2000). At stations located about 1 km away from the Nojima fault the crack orientations inferred from S-wave splitting were dominantly E-W, which is also the direction of the regional maximum horizontal compressive stress. In closer proximity to the fault (within 500 m), the dominant fracture orientation was parallel to the fault strike (N45-50E). These fractures of shear origin are related to the Kobe event. Moreover, such fractures were found to be non-existent around active faults that ruptured during an earthquake in 1596. Tadokoro et al. (1999) argued this to be due to complete healing of shear fractures around this latter fault. Following more surveys Tadokoro and Ando (2000) noted that the shear fractures that were observed in proximity to the Nojima fault completely disappeared within 33 months after the Kobe earthquake. This observation suggests that healing of these fractures is an extremely rapid event relative to the earthquake recurrence interval for such crustal faults.

References

An, L.J., Sammis, C.G., 1994. Particle size distribution of cataclastic fault materials from southern California: A 3-D study. Pure and Applied Geophysics 143, 203-227.

Aydin, A., Johnson, A.M., 1978. Development of faults as zones of deformation bands and as slip surfaces in sandstone. Pure and Applied Geophysics 116, 672-683.

Bathurst, R.G.C., 1958. Diagenetic fabrics in some British Dinantian limestones: Liverpool Manchester. Geological Journal 2, 11-36.

Biegel, R.L., Sammis, C.G., Dietreich, J.H., 1989. The frictional properties of a simulated gouge having a fractal particle distribution. Journal of Structural Geology 11, 827-846.

Blanpied, M.L., Lockner, D.A., Byerlee, J.D., 1991. Fault stability inferred from granite sliding experiments at hydrothermal conditions. Geophysical Research Letters 18, 609-612.

Bos, B., Spiers, C.J. 2000. Effect of phyllosilicates on fluid-assisted healing of gouge-bearing faults. Earth and Planetary Science Letters 184, 199-210.

Bos, B., Spiers, C.J. 2001. Experimental investigation into the microstructural and mechanical evolution of phyllosilicate-bearing fault rock under conditions favoring pressure solution. Journal of Structural Geology 23, 1187-1202.

Brace, W.F., Byerlee, J.D., 1966. Stick-slip as a mechanism for earthquakes. Science 153, 990-992.

Bridgeman, P.W., 1936. Shearing phenomena at high pressure of possible importance to geology. Journal of Geology 44, 653-669.

Bridgeman, P.W., 1951. Some implications for geophysicists of high-pressure phenomena. Geological Society of America Bulletin 62, 533-536.

Byerlee, J.D., 1978. Friction in rocks. Pure and Applied Geophysics 116, 718-727.

Byerlee, J.D., 1993. Model for episodic flow of high-pressure water in fault zones before earthquakes. Geology 21, 303-306.

Cao, T., Aki, K., 1986. Effect of slip rate on stress drop. Pure and Applied Geophysics 124, 515-529.

Chester, F.M., Logan, J.M., 1986. Implications for the mechanical properties of brittle faults from observations of the Punchbowl fault zone. Pure and Applied Geophysics 124, 79-106.

Chester, F.M., Logan, J.M., 1987. Composite planar fabric of gouge from the Punchbowl Fault, California. Journal of Structural Geology 9, 621-634.

Chester, F.M., Higgs, N.G., 1992. Multimechanism friction constitutive model for ultrafine quartz gouge at hypocentral conditions. Journal of Geophysical Research 97, 1859-1870.

Chester, F.M., Evans, J.P., Biegel, R.L., 1993. Internal structure and weakening mechanisms of the San Andreas Fault. Journal of Geophysical Research 98, 771-786.

Dewers, T.A., Hajash, A., 1995. Rate laws for water-assisted compaction and stress-induced water-rock interaction in sandstones. Journal of Geophysical Research 100, 13093-13112.

Dewers, T.A., Ortoleva, P., 1994. Formation of stylolites, marl/limestone alternations, and clay seams accompanying chemical compaction of argillaceous carbonates. In: Chilingarian G.V., Wolf, K.H. (Eds.), Diagenesis IV, Developments in Sedimentology 51, Elsevier, pp. 155-216.

Dieterich, J.H., 1979. Modeling of rock friction: 1. Experimental results and constitutive equations. Journal of Geophysical Research 84, 2161-2168.

Dieterich, J.H., 1992. Earthquake nucleation on faults with rate- and state- dependent strength. Tectonophysics 211, 115-134.

Dove, P.M., 1995. Geochemical controls on the kinetics of quartz fracture at subcritical tensile stresses. Journal of Geophysical Research 100, 22349-22359.

Engelder, J.T., 1974. Cataclasis and the Generation of Fault Gouge. Geological Society of America Bulletin 85, 1515-1522.

Fredrich, J.T., Evans, B., 1992. Strength recovery along simulated faults by solution transfer processes. In Tillerson, W.R., Wawersik, W.R., (Eds), Rock Mechanics Proceedings of the 33rd US Symposium, Balkema, pp. 121-130.

Hadizadeh, J., 1994. Interaction of cataclasis and pressure solution in a low-temperature carbonate shear zone. Pure and Applied Geophysics 143, 255-280.

Heald, M.T., 1955. Stylolites in sandstones. Journal of Geology 63, 101-114.

Hickman, S.H., Evans, B., 1991. Experimental pressure solution in halite: the effect of grain/interphase boundary structure. Journal of Geological Society London 148, 549-560.

Houseknecht, D.W., 1988. Intergranular pressure solution in four quartzose sandstones. Journal of Sedimentary Petrology 58, 228-246.

Karner, S.L., Marone, C., Evans, B., 1997. Laboratory study of fault healing and lithification in simulated fault gouge under hydrothermal conditions. Tectonophysics 277, 41-55.

Kennedy, L.A., Logan, J.M., 1997. The role of veining and dissolution in the evolution of fine grained mylonites; the McConnell Thurst, Alberta. Journal of Structural Geology 19, 785-797.

Li, Y.G., Vidale, J.E., Aki, K., Fei, X., Burdette, T.R., 1998. Evidence of shallow fault zone strengthening after the 1992 M7.5 Landers, California, earthquake. Science 279, 217-219.

Lockner D.A., Byerlee, J.D., Kuksenko, V., Ponomarev, A., Sidrin, A. 1992. Observations of quasi-static fault growth from acoustic emissions. In: Evans, B., Wong T.-F. (Eds), Fault Mechanics and Transport Properties of Rocks, Academic, San Diego, California, pp. 3-31.

Logan, J.M., Teufel, L.W., 1986. The effect of normal stress on the real area of contact during frictional sliding in rocks. Pure and Applied Geophysics 116, 964-989.

Logan, J.M., 1981. Laboratory and field investigations of fault gouge. Open File Report US Geological Survey 85 p.

Maliva, R.G., Siever, R., 1988. Mechanisms and controls of silicification of fossils in limestones. Journal of Geology 96, 387-398.

Marone, C., Kilgore, B., 1993. Scaling of critical slip distance to seismic faulting with shear strain in fault zones. Nature 362, 681-621.

Marone, C., Raleigh, C.B., Scholz, C.H., 1990. Frictional behavior and constitutive modeling of simulated fault gouge. Journal of Geophysical Research 95, 7007-7025.

Marone, C., Scholz, C.H., 1989. Particle-size distribution and microstructures within simulated fault gouge. Journal of Structural Geology 11, 799-814.

Massonnet, D., Fiegl, K., Rossi, M., Adragna, F., 1994. Radar interferometric mapping of deformation in the year after the Landers earthquake. Nature 369, p. 227-230.

Morrow, C.A., Byerlee, J.D., 1989. Experimental studies of compaction and dilatancy during frictional sliding on faults containing gouge. Journal of Structural Geology 11, 815-825.

Morse, J.W., Casey, W.H., 1988. Ostwald processes and mineral assemblages in sediments. American Journal of Science 288, 537-560.

Olsen, M.P., Scholz, C.H., Leger, A., 1998. Healing and sealing of a simulated fault gouge under hydrothermal conditions: implications for fault healing. Journal of Geophysical Research 103, 7421-7430.

Power, W.L., Tullis, T.E., Weeks, J.D., 1988. Roughness and wear during brittle faulting. Journal of Geophysical Research 93, 15,268-15,278.

Rice, J.R., 1992. Fault stress states, pore pressure distributions, and weakness of the San Andreas Fault. In: Evans, B., Wong, T-F., (Ed) Fault Mechanics and Transport Properties of Rocks, pp. 475-503.

Robertson, E.C., 1983. Relationship of fault displacement to gouge and breccia thickness. AIME Transactions 35, 1426-1432.

Ruina, A., 1983. Slip instability and state variable friction laws. Journal of Geophysical Research 88, 10359-10370.

Rutter, E.H., Maddock, R.H., Hall, S.H., White, S.H., 1986. Comparative microstructures of natural and experimentally produced clay-bearing fault gouges. Pure and Applied Geophysics 124, 3-30.

Sammis, C.G., Osborne, R.H., Anderson, J.L., Banerdt, M., White, P., 1986. Self-similar cataclasis in the formation of fault gouge. Pure and Applied Geophysics 124, 53-78.

Sammis, C.G., King, G., Biegel, R., 1987. Kinematics of gouge deformation. Pure and Applied Geophysics 125, 777-812.

Sammis, C.G., Biegel, R.L., 1989. Fractals, fault gouge and friction. Pure and Applied Geophysics 131, 255-271.

Sammis, C.G., Steacy, S.J., 1994. The micromechanism of friction in a granular layer. Pure and Applied Geophysics 142, 777-794.

Scholz, C. H., 1990. The mechanics of earthquakes and faulting, Cambridge, 433p.

Sibson, R.H., 1979. Fault rocks and structure as indicators of shallow earthquake source processes. In: Speed, R.C. (Ed), Proceedings of Conference VIII, Open File Report, US Geological Survey, pp. 276-304.

Sleep, N.H., 1995. Ductile creep, compaction, and rate and state dependent friction within major fault zones. Journal of Geophysical Research 100, 13065-13080.

Sleep, N.H., Blanpied, M.L., 1992. Creep, compaction, and the weak rheology of major faults. Nature 359, 687-692.

Spiers, C.J., Schutjens, P.M.T.M., 1990. Densification of crystalline aggregates by fluid-phase diffusional creep. In Barber, D.J., Meredith, P.G. (Eds.), Deformation Processes in Minerals, Ceramics and Rocks, Unwin Hyman, pp. 334-353

Steefel, C.I., Van Cappellen, P., 1990. A new kinetic approach to modeling water-rock interaction: the role of nucleation, precursors and Ostwald ripening. Geochimica Cosmochimica Acta 54, 2657-2677.

Tada, R., Siever, R., 1986. Experimental knife-edge pressure solution of halite. Geochimica Cosmochimica Acta 50, 29-36.

Tada, R., Siever, R., 1989. Pressure solution during diagenesis. Annual Reviews Earth Planetary Science Letters 17, 89-118.

Tada, R., Maliva, R., Siever, R., 1987. A new mechanism for pressure solution in porous quartzose sandstone. Geochimica Cosmochimica Acta 51, 2295-2301.

Tadokoro, K., Ando, M., Umeda, Y., 1999. S wave splitting the aftershock region of the 1995 Hyogo-ken Nanbu earthquake. Journal of Geophysical Research 104, 981-992.

Tadokoro, K., Ando, M., 2000. Evidence for rapid fault healing derived from temporal changes in S wave splitting. EOS Transactions American Geophysical Union 2000 Fall Meeting 81, F1173.

Wallace R.E., Morris H.T., 1986. Characteristics of faults and shear zones in deep mines. Pure and Applied Geophisics 124, 107-127.

Weyl, P.K., 1959. Pressure solution and force of crystallization - a phenomenological theory. Journal of Geophysical Research 64, 2001-2025.

Chapter 2

Granular aggregate creep in water-saturated porous halite, gypsum, calcite and quartz aggregates: a unifying rate law

Abstract

Volumetric time-dependent consolidation or creep is an important mechanism for transforming sediments into rocks. Analyses of experimental data on halite, gypsum, and quartz volumetric creep in the literature, coupled with new experimental data on calcite, shows that volume strain accumulates in a similar manner during drained, hydrostatic, compaction creep in all four minerals. This behavior is describable by a single constitutive equation that links rate of volume strain (or porosity loss) to the variables of total volume strain, grain size and applied effective pressure. It is based on a logarithmic strain-time relationship that permits quantification of aggregate strain history. Volume strain in porous aggregates undergoing pressure solution (or other possible mechanisms) is manifest as grain contact widening and porosity loss, and results in a gradual decline in strain rate of the aggregate with time or increasing strain. Quantifying the influence of this strain on creep rate allows

separation of strain effects from those of other variables, notably grain size and effective pressure. The proposed rate equation describes laboratory drained, hydrostatic compaction experiments in all four minerals to an excellent degree over fairly wide ranges in conditions at stresses below those known to cause purely mechanical pore collapse. The observation that rates correlate with solubility suggests that a similar mechanism dominates in all four minerals over the ranges of conditions studied, independent of the obvious differences in crystal classes, the rate-controlling mechanism for dissolution/precipitation kinetics in bulk water, and mineral hardness.

Introduction

Sediments become rocks by a variety of pathways, including some combination of chemically or biologically driven cementation and mechanical consolidation that together result in porosity loss and increasing lithification. On the mechanical side, one can differentiate among time-independent mechanisms for porosity loss (such as elastic compression, grain boundary sliding and pore collapse) and time-dependent mechanisms (which might include pressure solution, sub critical crack growth and crack-healing). Time-dependent compaction creep is presented in this chapter.

In addition to contributing to porosity loss in sedimentary basins, rates and mechanisms of sediment consolidation creep are of interest in such diverse arenas as fault zone strengthening or healing and earthquake recurrence (Sleep, 1995; Byerlee, 1993), sea-floor subsidence above petroleum reservoirs

(Boade et al., 1989; Menghini, 1989), and suitability of nuclear waste disposal sites. Creep behavior of evaporite minerals such as halite and gypsum are important as these can serve as detachment horizons in foreland thrust belts. Halokinetic structures developed during creep in salt domes trap economic hydrocarbon deposits.

In this chapter, a systematic analysis of laboratory experimental data from drained, hydrostatic compaction on well sorted, granular, porous aggregates of calcite, quartz, gypsum, and halite systems reveals an underlying similarity in how effective pressure, volume strain, and grain size influence volumetric creep rates. A constitutive equation (or "creep law") originally proposed for quartz sand compaction by Dewers and Hajash (1995), is shown to accurately describe aspects of halite, calcite and gypsum aggregate compaction as well. This suggests that a unique mechanism or combination of mechanisms is acting during compaction creep in all mineralogies examined in spite of the obvious differences in crystal chemistries, rate controlling dissolution kinetic mechanisms, solubilities, etc. At higher effective pressures or non-hydrostatic stress conditions creep in several of the investigated minerals occurs by a combination of mechanisms such as grain microfracturing and pressure solution. Finally, it is suggested that many aspects of crustal rock deformation can be studied on much more amenable time scales using evaporite minerals like halite. Creep laws such as the one proposed here are necessary to make appropriate time- and "mineralogy"- scaling relationships between laboratory and geologic time scales.

Hydrostatic Creep in Nature and Experiments

Creep in solids versus porous aggregates

The contrast between single mineral, solid aggregate, and porous aggregate creep should be clarified at the outset. Creep in solids is usually discussed in terms of an initial or primary stage, characterized by work hardening, or a slowing of strain-rate with increasing strain, a secondary stage sometimes called steady-state creep, and a tertiary stage involving an acceleration in strain-rate leading to failure (Jaeger and Cook, 1979; Cristescu and Hunsche, 1998). In the time-dependent consolidation of porous aggregates, it is really the first stage that is applicable. Volumetric creep of porous aggregates under hydrostatic loading arguably never reaches a steady-state, as long as porosity exists, because the local loading conditions at grain contacts are always changing with progressive creep.

Functional dependence of creep rate on time

Dewers and Hajash (1995) propose a constitutive relationship between the time-rate of change of volume strain (or porosity decline) and the variables of volume strain, temperature, effective pressure and aggregate grain size from experiments on well-rounded natural quartz sand. This rate equation was based on the observation that volume strain accumulated at a constantly decreasing rate according to the following expression:

$$\varepsilon_v - \varepsilon_v^{\,0} = a\ln(1+\frac{t-t_0}{b}) \qquad (1)$$

where ε_v and ε_v^0 are volume strains at times t, and t_0 respectively, and 'a' and 'b' are curve-fit coefficients. Differentiating equation (1) with respect to time yields the following for the time rate of change of strain

$$\frac{d\varepsilon_v}{dt} = \frac{a}{b+t} = \frac{a}{b}\exp\{-\frac{\varepsilon_v - \varepsilon_v^{\ 0}}{a}\} \tag{2}$$

This shows that the rate of volume strain decreases with the exponential of volume strain.

As found by Dewers and Hajash (1995), in experiments run with similar grain size, temperature and effective pressure, and in experiments which have experienced cyclic loading, ε_v^0 represents any permanent volume strain at the initiation of time-dependent creep at constant effective pressure. This allows comparison of results between experiments at different total volume strains, because in (2), the time rate of change of total strain is separable into strain-dependent and strain-independent parts. Letting ε_v^{lim} represent the "limiting" rate of volume change, i.e. that initial rate at zero strain, (2) can be expressed as:

$$\frac{d\varepsilon_v}{dt} = \varepsilon_v^{\ \mathrm{lim}} \exp(\frac{-\varepsilon_v}{a}) \quad \text{where } \varepsilon_v^{\ \mathrm{lim}} \equiv \frac{a}{b}\exp(\frac{\varepsilon_v^{\ 0}}{a}) \tag{3}$$

This forms the basis of the constitutive equation by accounting for the influence of strain, as ε_v^{lim} is held to be an intrinsic property of the aggregate-water system independent of volume strain or porosity. Equation (3) yields a linear relationship when plotted as ln(strain rate) versus strain; examples of this are shown in Figure 2.1. In volumetric creep of fine grained quartz and calcite aggregates, a linear relationship is obtained, with a y-intercept equaling the $\ln(\varepsilon_v^{lim})$ and slope of a^{-1} as defined in equation (3). Deviations from this behavior are observed for coarser grained aggregates, and are discussed below.

Multiple-Mode Deformation

Multiple mechanisms involved such as pressure solution, microfracturing and sub-critical crack growth and healing contribute to the overall granular creep rate. Experimental set-up in different studies are tailored such that a single mechanism *e.g.* pressure solution may be dominant. This is achieved by application of low effective pressure that minimizes accumulation of volume strain via grain fracturing. However, it is nearly impossible to negate such other mechanisms from occurring in a given experimental set-up. Especially common is the role of grain fracturing and grain boundary sliding early in the loading and creep process. Schutjens (1991) data on hydrostatic compaction of granular quartz aggregate at 300°C is compared with that of data on granular creep of angular calcite (Iceland spar) at room temperature conducted as a part of this study. Figure 2.1a shows volume strain-rate plotted against volume strain from hydrostatic compaction creep of calcite from this study. When two different grain sizes 250-500 μm (medium) and 125-250 μm (fine) size are compared it is observed that the medium grain size exhibits an initial creep phase characterized by high strain rates (shallow slope in Fig. 2.1a) followed by a period of slow accumulation of volume strain.

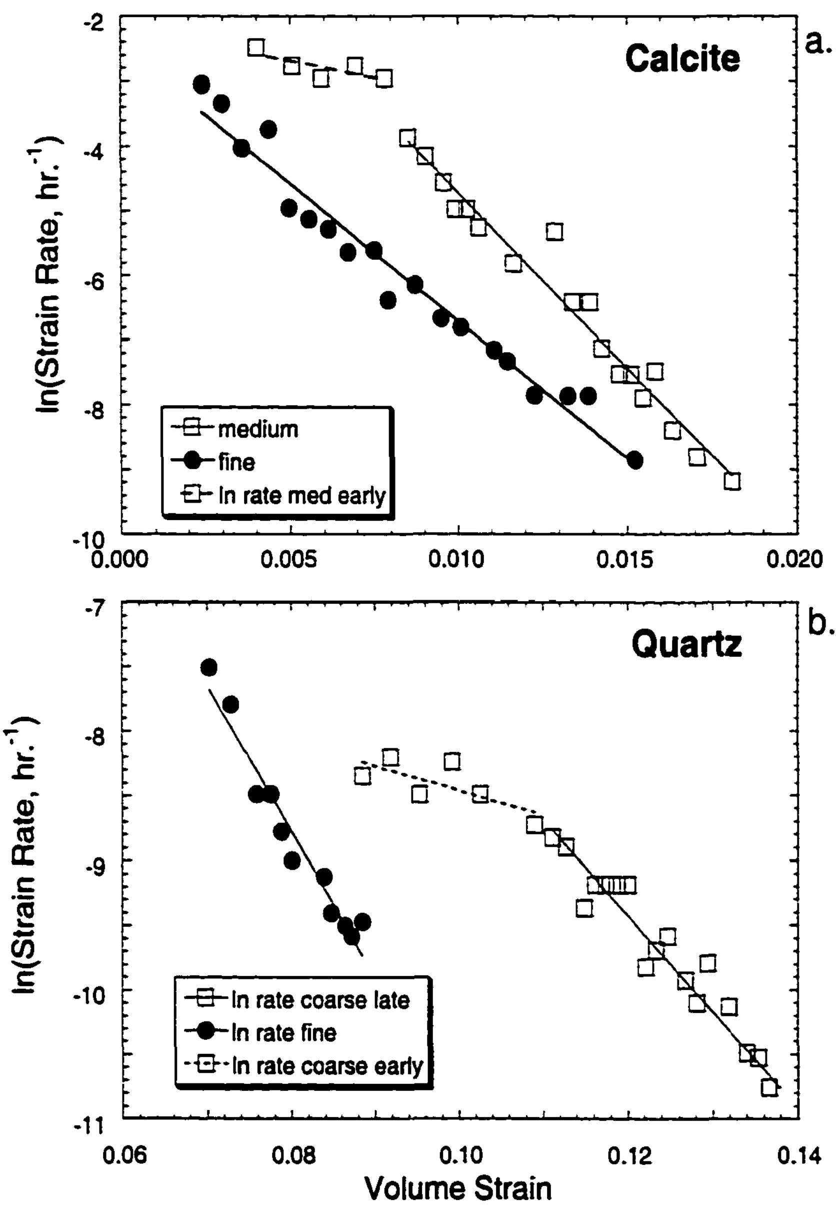

Fig. 2.1a: Strain rate plotted against volume strain for creep data on calcite (this study). The coarser grained aggregate has an initial high rate (shallow slope) followed by a lower rate (steep slope), while the finer grained aggregate lacks the initial high rate of creep. (b) Similar behavior as above exhibited by creep of quartz aggregate (Schutjens, 1991). Transient high strain rates initially in both minerals are due to contributions of grain boundary sliding, crack growth and twinning (in the case of calcite).

This early rapid phase is absent in creep of the fine aggregate. It is suggested that grain fracturing, intra-crystalline plastic twinning (common in calcite) and grain boundary sliding dominate this initial rapid phase of strain accumulation. Pressure solution is the primary mechanism during the latter phase. Interestingly, intensity of twinning in calcite has been observed to be inversely dependent on grain size (Railsback, 1992). This has been attributed to the fact that finer sizes require higher resolved shear stress to twin compared to coarser grains (Newman, 1994; Rowe and Rutter, 1990). That this combination of mechanisms is not unique to these experiments is made obvious by a comparison with granular creep of quartz aggregates at elevated temperature (Schutjens data plotted in Fig. 2.1b). This data set also indicates that coarse (90-110 μm) aggregates show an initial rapid phase of strain-accumulation while the finer sized (40 μm) aggregates typically exhibit a constant steep slope in volume strain rate - strain space. This slow accumulation of time-dependent volume strain has been suggested to be intrinsic to the pressure-solution creep process (de Meer and Spiers, 1995; Dewers and Hajash, 1995 among many others). In this chapter results from this phase of slow time-dependent deformation attributed to pressure solution is further analyzed.

Volume Creep in Aggregates of Four Mineralogies

Strain-time relations

The volume strain-time relationship in hydrostatic creep of granular aggregates of quartz (Dewers and Hajash, 1995), halite (Spiers and Schutjens, 1990), gypsum (de Meer and Spiers, 1995) and calcite (this study in Fig. 2.2 a through d) is compared. Examples of data from Dewers and Hajash (1995) that display this dependence of quartz are shown in Figure 2.2a. In Figure 2.2b, example data from volumetric creep in halite aggregates obtained from Spiers and Schutjens (1991; their Figure 12.5) is plotted. There is an excellent agreement between the equation (solid line) and the data. A similar logarithmic dependence of convergence (strain) on time can also be shown from the single crystal experiments of Hickman and Evans (1991; see their Figures 8, 9, and 14) and in the aggregate experiments of Raj (1982; his Figure 4).

Data for hydrostatic, wet creep of gypsum aggregates from de Meer and Spiers (1995) is plotted in Figure 2.2c. The strain-time relation fits time-dependent compaction behavior of all of their experiments very well. Aggregate creep from hydrostatic experiments conducted on calcite (this study) is shown in Figure 2.2d. The strain-time behavior of two different stress-stepping experiments (at atmospheric pore pressure and elevated pore pressure of 13.8 MPa) is plotted. These experiments have the added complexity in that even at low effective pressures, there is significant volume strain that results due to flow by microfracturing and spalling of angular corners, twinning at grain contacts and grain boundary sliding. Nonetheless, time dependent strain (early strain accounted for in the value of ε_v^0) accumulates according to the same logarithmic strain-time dependence.

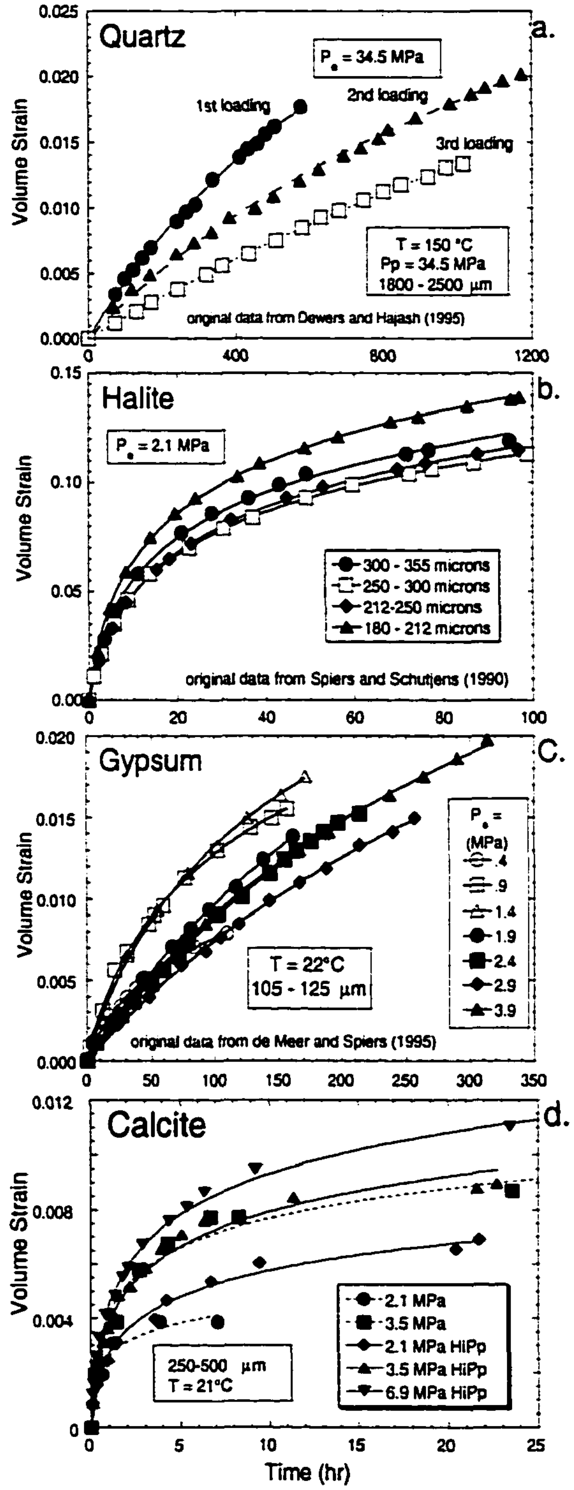

Fig. 2.2: Volume strain – time plots for (a) quartz, (b) halite, (c) gypsum and, (d) calcite. Lines show fits to logarithmic strain-time relation discussed in text.

Effective pressure dependence

In Figure 2.3 (a through d) the limiting strain rate dependence as defined in equation 3 for the four minerals is investigated. Data for quartz (Dewers and Hajash, 1995) is plotted in Figure 2.3a and illustrates that the limiting strain rate has an exponential dependence on effective pressure. Similar data for halite (Spiers and Scutjens, 1990) is shown in Figure 2.3b. As was found in the case of quartz sands (Dewers and Hajash, 1995), ε_v^{lim} increases as an exponential function of effective pressure, very different from the common linear dependence often invoked in models (e.g. Hickman and Evans, 1995; de Meer and Spiers, 1995). A similar dependence of strain rate (i.e., displacement or convergence rate) on effective pressure can be seen in the data on halite pressure solution from Gratier (1993; his Figure 3). Data for three different grain size fractions from gypsum aggregate experiments (de Meer and Spiers, 1995) have been analyzed to investigate the limiting strain rate-effective pressure dependence for gypsum. It can be observed from Figure 2.3c that the three different grain sizes follow a similar exponential dependence of initial strain rate on effective pressure with progressively higher strain rates for finer grain sizes. Calcite experiments (this study) show some interesting similarities with the other minerals investigated especially for low (atmospheric) pore pressure tests (Fig. 2.3d). An excellent fit to the P_e-dependence of the creep law is obtained. This suggests that, even with the initially dominant deformation mechanism of twinning and microfracturing, time-dependent compaction in calcite proceeds by similar systematics as discussed above for quartz, halite and gypsum.

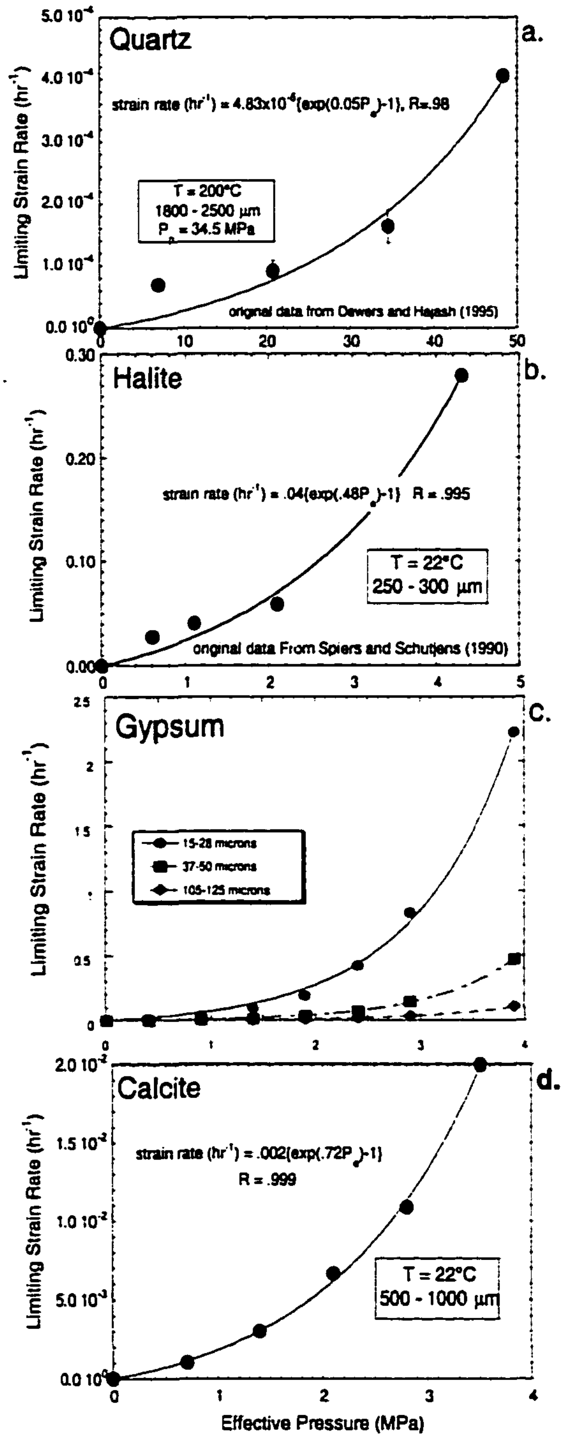

Fig. 2.3: Limiting strain rate plotted against effective pressure for (a) quartz, (b) halite, (c) gypsum and, (d) calcite creep. Creep in each of these minerals can be represented by an exponential dependence of strain rate on effective pressure.

The experiment at elevated pore pressure where larger effective pressure steps (2.1, 3.4, 4.8, 6.9 MPa) are imposed shows similar strain-time behavior (discussed before in Fig. 2.2d) but does not fit limiting strain rate-P_e relationship as well especially at higher effective pressures possibly due to the dominating influence of other creep mechanisms such as time-dependent crack growth. This is discussed further in chapter 6.

Grain size dependence

It has long been suggested that grain size exerts a strong influence on the presence or absence of pressure solution textures in sandstones, limestones, and other lithologies (Tada and Siever, 1989). In Figure 2.4, grain size dependencies of limiting strain rates for all four mineralogies are illustrated. Each show a power law dependence on the inverse grain size raised to the power ~2.3. This agreement shows that the usually assumed inverse-grain size raised to an integer power of three (the water-film diffusion model) or one (the free-face model) are an oversimplification, and may be pointing out additional complexity in the structure of grain boundary physical chemistry involved in the pressure solution process.

Summary Rate Expressions

Based on the above functional dependencies of accumulated volume strain on strain, effective pressure, and grain size, a multivariate regression is

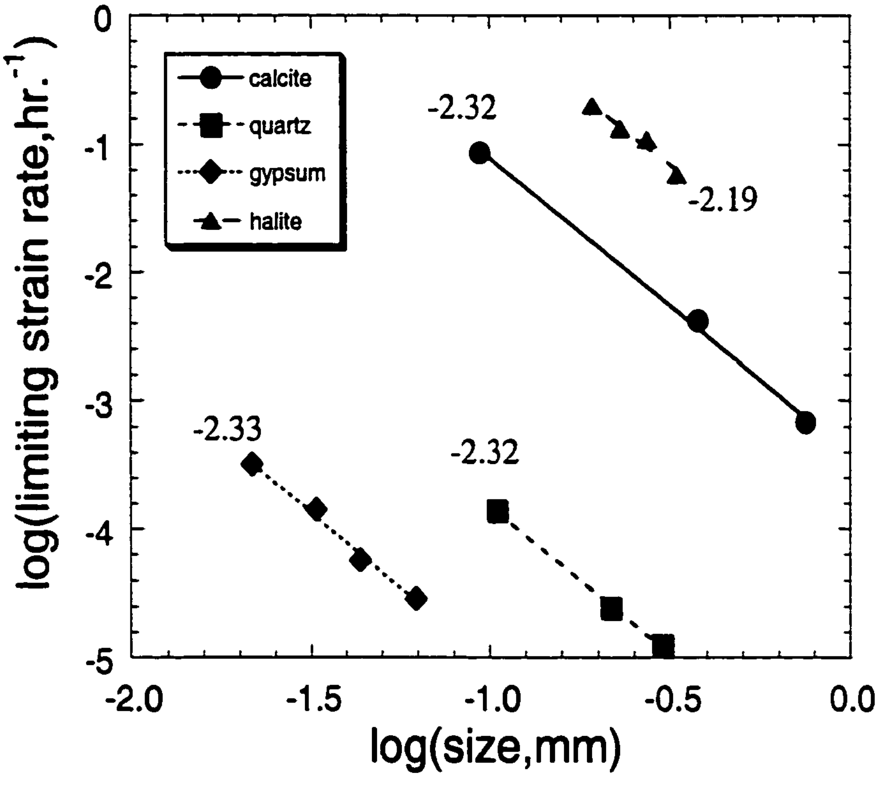

Fig. 2.4: Limiting strain rate plotted against grain size for all minerals. Note the consistent slope for the 4 minerals that are analyzed.

performed using available data sets and the following equation involving five fit parameters:

$$\varepsilon_v - \varepsilon_v^0 = z_1 \ln\left\{1 + \frac{z_2 e^{-\varepsilon_v^0 / z_1}}{z_3 d^{z_4}} (e^{z_3 P_e} - 1)(t - t_o)\right\} \qquad (4)$$

Table 2.1: Multivariate curve fitting results. The grain size exponent (z_4) is constant at 2.3 based on results from Figure 2.4 in method 2.

	Method 1				Method 2		
Mineral	z_1	z_2	z_3	z_4	z_1	z_2	z_3
Quartz[1]	0.016	8.30e-5	1.57e-3	1.6	0.016	1.70e-5	1.58e-3
Gypsum[2]	0.018	1.40e-5	1.16	1.7	0.013	2.72e-6	1.79
Halite[3]	0.030	1.66e-3	0.48	3.0	0.033	4.04e-3	0.39

[1] T = 150°C, P_p = 34.5 MPa, maximum P_c = 34.5 MPa, maximum ε_v equals 0.08 , 90 data points (R=.98 and .92 for 2 cases)

[2] T = 22°C, P_p = 0.1 MPa, maximum P_c = 3.9 MPa, maximum ε_v equals 0.19 , 294 data points (R=.97 and .95)

[3] T = 22°C, P_p = 0.1 MPa, maximum P_c = 4.2 MPa, maximum ε_v equals 0.22, 122 data points (R=.99 and .99)

original data from Dewers and Hajash (1995)[1], de Meers and Spiers (1995)[2], Schutjens (1991)[3]

This was done in two ways, both of which employ a Levenberg-Marquardt algorithm. In the first method, equation (4) is fitted with a variable z_4 (grain size exponent) coefficient, and in the second, the z_4 coefficient is fixed at 2.3, as suggested in Figure 2.4. The results of both methods, the quality of fit, and the range of applicable conditions for each mineral are listed in Table 2.1.

The quality of fit in both methods suggests that unique grain size dependence may not be obtainable from this method as a range of grain size coefficients (z_4) yield statistically indistinguishable fits. This points out that caution must be applied in using the exact grain size dependence to infer a rate-limiting mechanism to the creep process. For example, a z_4 value close to unity is used to infer a free-face pressure solution mechanism (Tada and Siever, 1986; Shimuzu, 1995; Paterson, 1995) or precipitation as a rate limiting step in the solution mass-transfer process (de Meer and Spiers, 1999), while a coefficient close to three is suggestive of a water film diffusion mechanism (Tada and Siever, 1989; Shimuzu, 1995; Paterson, 1995).

Discussion and Conclusions

Due to abundant grain contact textures, Spiers and Schutjens (1990), Dewers and Hajash, (1995) and de Meer and Spiers (1995) suggest solution-transfer as the dominant mechanism in their creep experiments on halite, quartz and gypsum respectively. The similarities between experimental quartz, halite and gypsum compaction all under isotropic loading, is strong evidence that the same mechanism is responsible in both. It should be noted that volumetric strain rates for halite at room temperature are 3 to 4 orders of magnitude faster than those for quartz at 150°C and two orders of magnitude faster than gypsum, a difference that interestingly correlates with the differences in their respective solubilities at experimental conditions (~6 molal for halite, 2 10^{-2} molal for gypsum, and ~2 10^{-3} molal for quartz).

Despite all of the published accounts of creep behavior, and a variety of derived creep laws for various experimental designs, it appears that there are striking similarities in how aggregates of a range of mineralogies compact in a time-dependent fashion. As pressure solution by definition involves a stress- or strain-mediated water-rock interaction, this similarity is all the more interesting given the differences in rate controlling mechanisms involved in water-mineral reaction at unstressed (or "free") grain facets for the different minerals. Interfacial reaction at halite-water interfaces occurs so rapidly that the overall kinetics of halite dissolution in water is limited by transport (diffusion) of dissolved products away from the interface. Gypsum reaction occurs much more slowly; its dissolution kinetics in water exhibits a mixed surface reaction/transport control (Raines and Dewers, 1997). Calcite dissolution in water, under the temperature, pH and pCO_2 conditions used in the experiments, is limited by the surface reaction rate, as is quartz-water reaction. The similarities in rate laws governing volume creep shown here suggest that the operational rate controlling step limiting the creep rate in all four mineral systems is not just simply related to the kinetic step limiting free-face reaction rates. Finally, this study suggests that many quantitative aspects of wet creep (pressure solution?) processes thought to be active during diagenesis and metamorphism of crustal rocks can be explored on laboratory time scales using far more rapidly compacting evaporite minerals.

References

Bathurst, R. G. C., 1958. Diagenetic fabrics in some British Dinantian limestones. Liverpool Manchester Geological Journal 2, 11-36.

Boade, R.R., Chin, Y.L., Seimers, W.T., 1989. Forecasting of Ekofisk reservoir compaction and subsidence by numerical simulation. Journal of Petroleum Technology, 723-728.

Byerlee, J. D., 1993. Model for episodic flow of high-pressure water in fault zones before earthquakes. Geology 21, 303-306.

Cristescu, N.D., Hunsche, U., 1998. Time Effects in Rock Mechanics, Wiley, New York, 342p.

de Meer, S., Spiers, C., 1995. Creep of wet gypsum aggregates under hydrostatic loading conditions. Tectonophysics 245, 171-183.

de Meer, S., Spiers, C., 1999. Influence of pore-fluid salinity on pressure solution creep in gypsum. Tectonophysics, 308, 311-330.

Dewers, T.A., Hajash, A., 1995. Rate laws for water-assisted compaction and stress-induced water-rock interaction in sandstones. Journal of Geophysical Research 100, 13093-13112.

Gratier, J.P., 1993. Experimental pressure solution of halite by an indenter technique. Geophysical Research Letters 20, 1647-1650.

Hickman, S.H., Evans, B., 1991. Experimental pressure solution in halite: the effect of grain/interphase boundary structure. Journal Geological Society of London 148, 549-560.

Hickman, S.H., Evans, B., 1995. The kinetics of pressure solution at halite-silica interfaces and intergranular clay films. Journal of Geophysical Research 100, 13113-13,132.

Jaeger, J.C. Cook, N.G.W., 1979. Fundamentals of Rock Mechanics. Chapman and Hall, New York, 593p.

Menghini, M.L., 1989. Compaction monitoring in the Ekofisk area chalk fields. Journal of Petroleum Technology, 735-739.

Newman, J., 1994. The influence of grain size and grain size distribution on methods for estimating paleostresses from twinning in carbonates. Journal of Structural Geology16, 1589-1601.

Paterson, M.S., 1995. A theory for granular flow accommodated by material transfer via an intergranular fluid. Tectonophysics 245, 135-151.

Railsback, B., 1993. Control of crystal shape and size on formation of twin lamellae in calcite: implications for deep burial diagenetic fabrics in limestones. Carbonates and Evaporites 8, 156-162.

Raines, M., Dewers, T., 1997. Mixed transport/reaction control of gypsum dissolution kinetics and the development of gypsum karst. Chemical Geology 140, 29-48.

Raj, R., 1982. Creep in polycrystalline aggregates by matter transport through a liquid phase. Journal of Geophysical Research 87, 4731-4739.

Rowe, K.J., Rutter, E.H., 1990. Paleostress estimation using calcite twinning: experimental calibration and application to nature. Journal of Structural Geology 12, 1-17.

Schutjens, P.M.T.M., 1991. Experimental compaction of quartz sand at low effective stress and temperature conditions. Journal of the Geological Society of London 148, 527-539.

Shimizu, I., 1995. Kinetics of pressure solution creep in quartz: theoretical considerations. Tectonophysics 245, 121-134.

Sleep, N.H., 1995, Ductile creep, compaction, and rate and state dependent friction within major fault zones: Journal of Geophysical Research, v. 100, 13065-13080.

Spiers, C.J., Schutjens, P.M.T.M., 1990. Densification of crystalline aggregates by fluid-phase diffusional creep. In: Barber, D.J., Meredith, P.G. (Eds), Deformation Processes in Minerals, Ceramics and Rocks, Unwin-Hyman, Boston, pp. 334-353.

Tada, R., Siever, R., 1986. Experimental knife-edge pressure solution of halite. Geochimica Cosmochimica Acta 50, 29-36.

Tada, R., Siever, R., 1989. Pressure solution during diagenesis. Annual Reviews Earth Planetary Science Letters 17, 89-118.

Chapter 3

Strength recovery and slip instability of laboratory faults: an earthquake mechanism

Abstract

It has become evident that healing of fault zones occurs rapidly after a seismic event; and it is likely that the associated strengthening controls subsequent earthquake instabilities. Fault zone healing by chemical processes and its effects on strength and sliding stability are investigated here utilizing laboratory faults. The experiments include up to 15 cycles of hold-slide-hold loading of precut sandstone cylinders with gypsum gouge. Experiments with water-saturated gouge display (1) systematic increase of gouge shear strength, with up to 25% strengthening during the longest cycle (twelve days); (2) unstable yielding of the gouge with large stress drops; (3) common evidence for cementation, crack sealing, recrystallization, porosity reduction and grain welding in gouge loaded for long hold times; and (4) non-linear increase of stress drop magnitudes with increasing hold time. All these features are absent in identical tests with dry gypsum gouge. It is proposed that these laboratory faults are direct analogs of crustal faults as equivalent chemical processes are active in both experiments and crust. Observations of fault-zone strengthening from these room temperature gypsum experiments may be extended to crustal

materials such as quartz in seismogenic conditions as the kinetic rate constants for gypsum and quartz are within a few orders of magnitude. It follows that crustal fault-zones are progressively lithified during interseismic stages and the extent of this lithification controls slip instability and stress drop magnitude during earthquakes.

Introduction and Experimental Method

The nature of slip along an active fault is controlled by a complex combination of mechanical and chemical processes (Blanpied et al., 1998; Dieterich and Kilgore, 1994; Hadizadeh, 1994). The dominant mechanical processes in a sliding fault-zone include wear of asperities, grain crushing and grain rotations (Mair and Marone, 2000; Dieterich and Kilgore, 1994; Marone and Scholz, 1989; Power et al., 1988; Byerlee et al., 1978). The likely time-dependent chemical processes that result in lithification of gouge materials, include cementation, recrystallization, pressure solution, crack sealing and grain contact welding (Sleep and Blanpied, 1992; Olsen et al., 1998). This research investigates the effects of chemical processes on strength and sliding stability of laboratory fault-zones. Month-long experiments of cyclical holding and sliding were conducted on precut sandstone cylinders with water-saturated or dry gypsum gouge. This experimental design is common for rock friction testing (Byerlee et al., 1978) and in gouge healing studies (Olsen et al., 1998; Karner et al., 1997), although most of the latter studies examine strength evolution over a single hold-slide sequence (Karner et al., 1997). The present experiments include multiple cycles of loading, up to 15 hold-slide-hold cycles for a single sample, and up to six orders of magnitude of hold periods (up to 10^6 s). It is argued that the present experiments capture aspects of gouge behavior under conditions of mid-crustal seismogenic depth, and as such are phenomenologically similar to earthquakes along crustal faults.

The experiments were conducted using cylinders of Berea sandstone, 25 mm in diameter and 60 mm in length with a surface-ground precut at 30° to the sample long axis (inset in Fig. 3.1a). The sandstone has an initial porosity of ~20% and permeability of ~100 millidarcies at experimental conditions. These high values facilitate gouge-sandstone pore pressure equilibration during the experiments. The 4mm-thick gouge layer in each experiment was composed of natural gypsum sand (White Sands National Monument, New Mexico, USA) with mean particle size of 125 μm. Distilled water was used as pore fluid. Experiments were run at room temperature in a triaxial cell under confining pressure and pore pressures of 20.7 MPa and 6.9 MPa respectively. The samples were subjected to hold-slide-hold cycles with hold periods ranging from 10s to 10^6s, and axial strain rates of $2.6 \cdot 10^{-5}$ s^{-1} for sliding cycles. Each experiment began with a hydrostatic hold period, with subsequent hold periods under axial (shear) loading. In a slide stage, samples were axially shortened to a pre-determined strain. During hold periods, confining pressure and pore pressure were maintained constant, while axial load was allowed to relax. The resulting pore volume loss was monitored using a volumometer with a resolution of 0.0047 cm^3. Four experiments were run with water-saturated samples and one with a nominally dry sample. The present experiments were conducted using gypsum gouge due to its fast reaction rates in water. Room temperature (dissolution) rate constants for gypsum-water reaction (10^{-7} moles/cm^2.s, Raines and Dewers, 1997; Jeschke et al., 2001) fall within a few orders of magnitude for crustal materials like quartz at seismogenic conditions (10^{-9} moles/cm^2.s at 300°C, Dove and Crerar, 1990).

Results

Results of an experiment with 15 hold-slide cycles conducted in the presence of pore water and a dry experiment (4 cycles) are shown in Figure 3.1a and 3.1b respectively. In the wet experiment, the sample was pre-loaded hydrostatically under mean stress of 20.7 MPa and then axially loaded until sliding was initiated. The initial hydrostatic loading produced a non-linear stress-strain curve reflecting the compaction of the initially unconsolidated gouge[6]. The stress-strain curves of the subsequent cycles display the following features (shown schematically in Fig. 3.2a). First, the shear stress increases up to P_i, the peak shear stress of the i^{th} cycle (segment I in Fig. 3.2a). The slope of this quasi-linear segment is 14.5 GPa, which approximates the weighted Young's modulus of Berea sandstone with 4mm thick gypsum gouge. This slope indicates negligible inelastic gouge deformation during segment I. Second

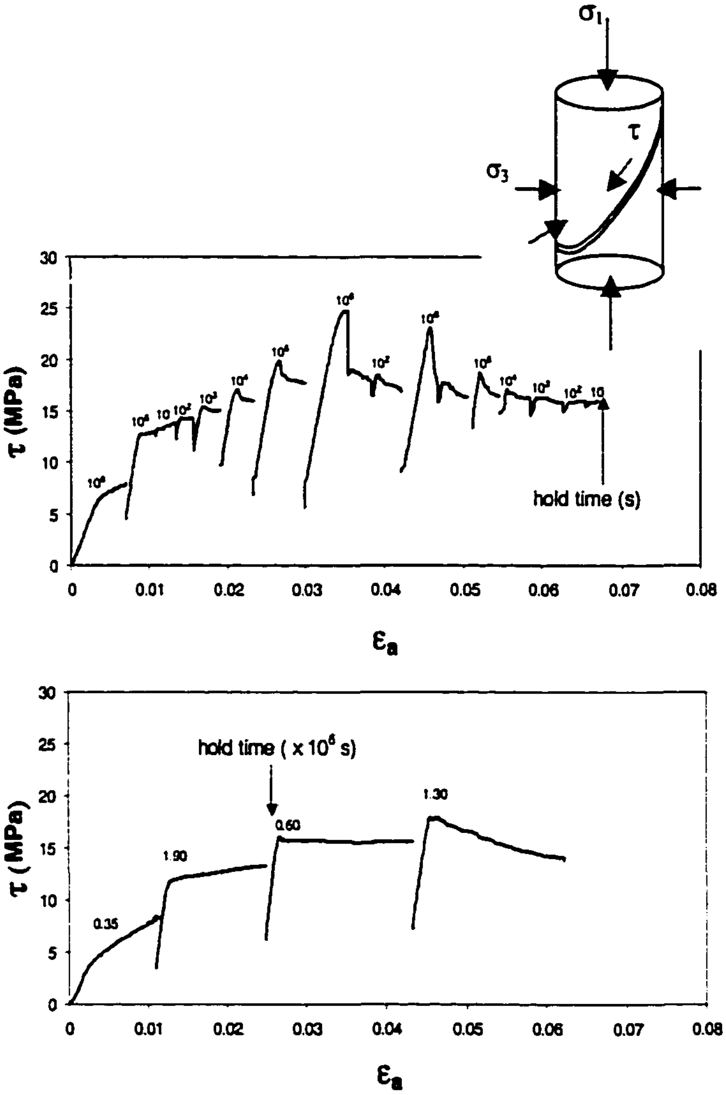

Fig. 3.1: Shear stress in hold-slide-hold tests in sandstone samples with gypsum gouge deformed at room temperature. The shear stress (τ) calculated for the fault plane is plotted against axial strain (ε_a). The hold duration (in seconds) for a hold period preceding a sliding event is noted. Inset shows schematic set-up of sample (25 mm diameter by 60 mm long), with principal stress directions and sense of slip along precut oriented at 30° to the axial loading axis (σ_1). (a) Water saturated, drained sample subjected to fifteen hold-slide cycles. Note the increase in peak strength, residual strength and the amount of stress drop (defined in text) with increase in hold time. (b) Dry sample subjected to four hold-slide cycles. In each cycle the shear stress builds up rapidly followed by stable sliding along the sawcut. Notable is the absence of marked peak strength (cohesion), although the residual strength increases similarly to the first seven loading cycles in (a).

(segment II), after P_i, the shear stress drops appreciably with an associated increase of pore volume (dilatancy, not shown). Third (segment III), the shear stress remains at a near constant level (S_i) that reflects stable sliding within the gouge. Finally during segment IV (the hold period), the shear stress relaxes. The hold periods in Figure 3.1a were increased in order-of-magnitude steps from 10s to 10^6s (twelve days), and following a short hold time of 10^2s, they were decreased from 10^6s to 10s. The observed peak stresses and stress drops are proportional to the hold duration as will be discussed in detail later.

One experiment (Fig. 3.1b) was run with a nominally dry sample subjected to the same effective loading conditions as in the previous tests. After an initial compaction phase, the gouge was subjected to four hold-slide cycles with hold periods of 10^5s to 10^6s. During the initial loading phase of each cycle, the shear stress increases with a quasi-linear slope of 14.7 GPa similar to the water-saturated tests shown in Figure 3.1a. Following the initiation of sliding, the stress-strain slope decreases to a quasi-constant value that reflects stable sliding along the dry gouge zone. Similar stress-strain behavior is observed in previous precut experiments over shorter durations (Logan et al., 1992). One can clearly note that the peak stress and the subsequent stress drop that dominate water-saturated tests (Fig. 3.1a) are absent in tests run with nominally dry gouge (Fig. 3.1b). This difference is attributed to chemical processes that could operate at measurable rates only in the water-saturated tests. Mechanical processes such as rigid body grain motion and microfracture-related granulation would have been active in both wet and dry tests.

To quantify the strength variations seen in Figure 3.1, three strengthening parameters for the i^{th} hold-slide cycle are defined (Fig. 3.2a). The 'gouge strengthening', $(\Delta\tau_P)_i = (P_i - S_{i-1})$, reflects the increase of cohesive shear strength during the hold time. The 'slip strengthening', $(\Delta\tau_S)_i = (S_i - S_{i-1})$, is the change of stable sliding strength between consecutive cycles. The 'stress-drop', $(\Delta\tau_D)_i = (P_i - S_i)$, is the difference between the peak strength and the sliding strength during a given cycle.

These strengthening parameters were determined for hold-slide-hold cycles in the four long-term, water-saturated experiments and the single dry experiment; they are shown in Figure 3.2b as a function of hold time. Even though the data points are scattered, two clear trends emerge. First, the slip strengthening ($\Delta\tau_S$) saturates to a constant value of approximately 3 MPa early in each experiment and then becomes independent of hold time. Second, the gouge strengthening ($\Delta\tau_P$) does not saturate but continues to increase with hold time. In contrast to the slip strengthening, the gouge strengthening is a reversible function of hold time, decreasing proportionately as hold time is lessened (Fig. 3.1a). The solid line shows the fit of the gouge strengthening data in all experiments to a logarithmic function of hold time, but other relationships are possible. The slip strengthening of dry experiments (three triangles in Fig. 3.2b) is similar in magnitude to that of the water-saturated tests for hold times greater than 10^3s (solid squares). This suggests that slip strengthening results from the action of mechanical processes on the gouge

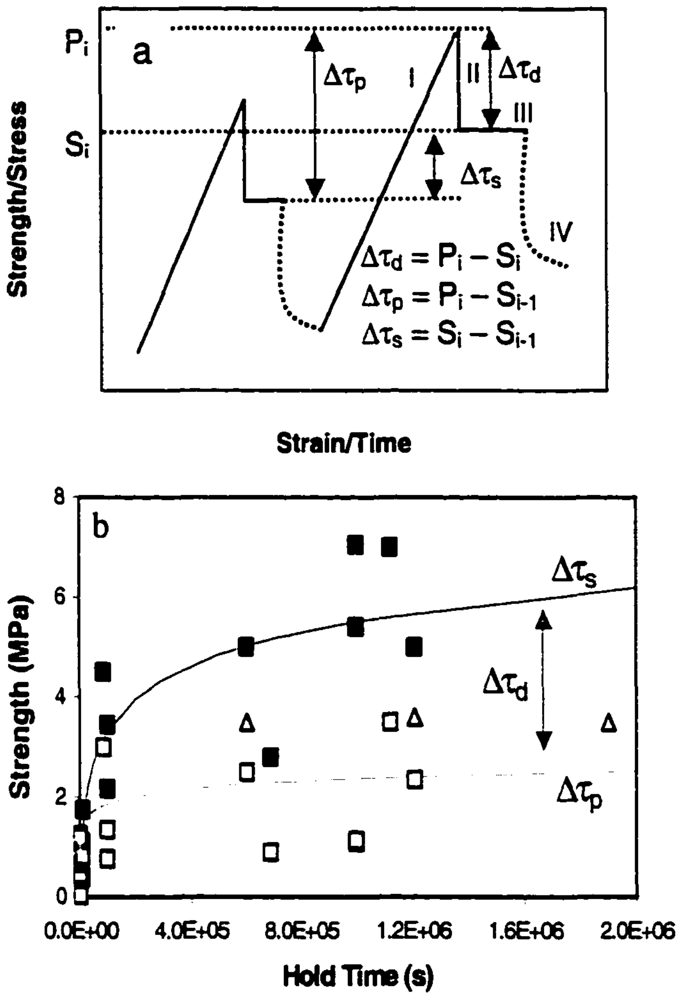

Fig. 3.2: Strengthening and hold times in wet and dry samples. (a) Schematic illustration of a typical strength profile for a slide-hold cycle. Stage I: rapid increase in shear stress during loading until peak strength is attained; Stage II: an abrupt stress drop at failure; Stage III: stable sliding at the residual strength for that slide event; Stage IV: the shear stress relaxes rapidly at first and then slowly during the hold period. Also shown the three strength parameters defined in the text: 'gouge strengthening' ($\Delta\tau_p$), 'slip strengthening' ($\Delta\tau_s$) and 'stress drop' ($\Delta\tau_d$). (b) Strengthening parameters ($\Delta\tau_p$-solid symbols and $\Delta\tau_s$-open symbols) plotted as a function of hold times; included are results from four water saturated experiments (squares) and one dry experiment (triangles). $\Delta\tau_s$ for both wet and dry experiments remain fairly constant over the range of hold periods. $\Delta\tau_p$ for wet experiments increases as a function of hold time. Solid curve represents fit of $\Delta\tau_p$-hold time data to a logarithmic function of the form $\Delta\tau_p$ (MPa) = 0.98 ln{0.0003 · hold time (s) + 1}. Dashed curve represents fit of $\Delta\tau_s$-hold time data to a similar function of the form $\Delta\tau_s$ (MPa) = 0.22 ln{0.06 · hold time (s) + 1}.

material and in this respect is equivalent to 'frictional healing' in the rate- and state-dependent friction formulation (Marone and Scholz, 1989; Mair and Marone, 2000; Sleep and Blanpied, 1992; Dieterich, 1979). The time evolution of peak strength and subsequent stress drops show that significant strengthening operates only in the presence of water and is thus indicative of water-assisted chemical processes.

Further contrast between wet and dry behavior is evident from microstructural observations. SEM photomicrographs (Fig. 3.3) show a total obliteration of porosity in the deformed wet gouge (Fig. 3.3a) in contrast to remnant intergranular porosity in deformed dry gouge (dark areas denoted *p* in Fig. 3.3b). Dry gouge displays extensive microfracturing and granulation as well as intracrystalline plastic deformation (*i* in Fig. 3.3b). These features, produced during loading in all experiments, are (virtually) absent in the water-saturated, long hold-time experiments. For example, rounded grain boundaries (marked *g* in Fig. 3b) are distinct in dry gouge while in wet gouge the grain boundaries are barely conspicuous and appear to be welded together (marked *wb* in Fig. 3.3a). This behavior presumably results from a combination of plastic flow, grain interpenetration, grain boundary migration, and stress- or strain-induced solution mass transfer (*c* in Fig. 3.3a). Open microfractures are observed in the deformed dry gouge (*f* in Fig. 3.3b), whereas the wet gouge exhibits trails of fluid inclusions resulting from healing of microfractures (*hf* in Fig. 3.3a).

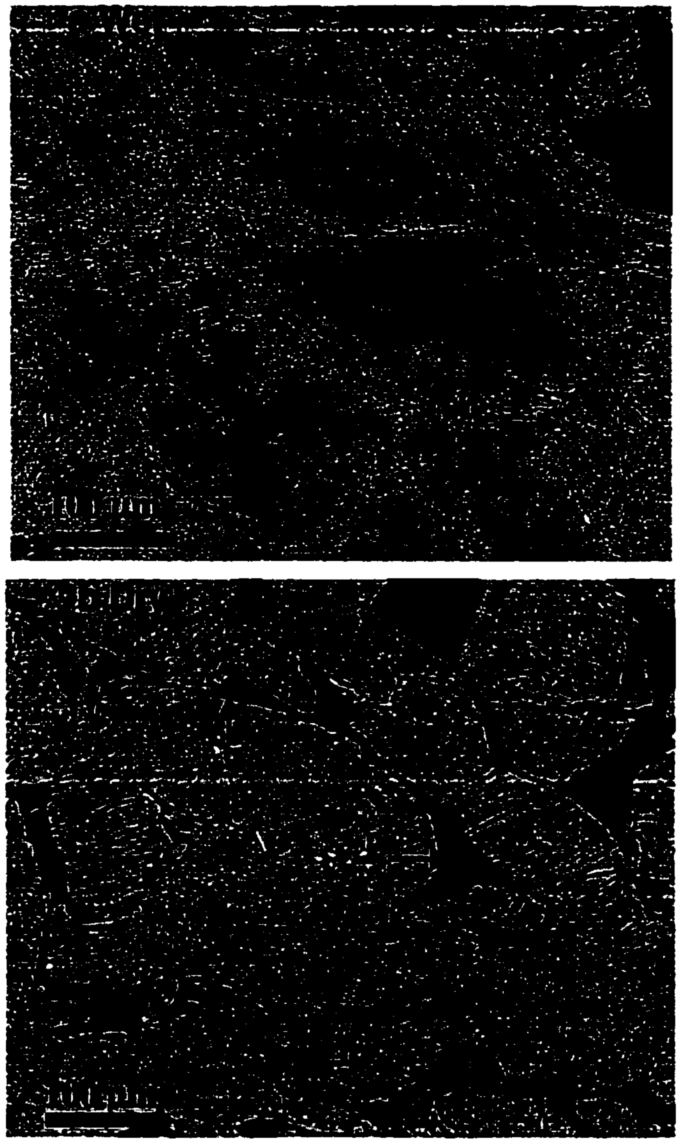

Fig 3.3: Backscattered scanning electron (SEM) photomicrograph showing contrast in texture between experimental gouge deformed wet (a) and dry (b). The wet gouge is characterized by welded grains that obscure original boundaries (wb), healed microfractures indicated by fluid inclusion trails (hf) and recrystallization (c). Note distinct grain boundary (g), intergranular pore space (p) and abundant open microfractures (f) and intracrystalline deformation (i) in dry gouge and their absence in wet gouge. Deformation conditions were similar in both cases (P_e=13.8 MPa, about 60 days, and 7% axial shortening).

Implications for Earthquake Mechanics

The mechanical data (Fig. 3.1a and 3.1b) and the microstructural observations (Fig. 3.3) demonstrate that lithification effectively strengthens fault gouge. Apparently, this strengthening is so efficient that the stress-strain curve of an individual cycle in wet tests (with hold time on the order of 10^5 s or longer as in Fig. 3.2a) is similar in shape to the equivalent curve of a failure test of intact (semi-brittle to brittle) rock (Scott and Nielsen, 1991; Bernabe and Brace, 1990). The shear stress-axial strain curve of a single loading cycle (after a long hold period > 10^5s) in the wet experiments described here and similar relations for deformation of an intact rock sample exhibits a quasi-linear, primarily elastic load increase up to a maximum strength (P_i in present experiments and ultimate strength in triaxial deformation of intact rock samples). The peak strength is followed by failure, strain softening, stress drop and stable sliding on the newly formed shear surface (Fig. 3.2a). In intact rock tests, the failure may be highly unstable and associated with a 20% to 50% stress drop (Scott and Nielsen, 1991; Bernabe and Brace, 1990).

Unstable slip between two separate blocks is regarded as the laboratory analogue of crustal earthquakes. Almost invariably this unstable slip is analyzed as a frictional phenomenon (Byerlee et al., 1978; Power et al., 1988; Karner et al., 1997), frequently utilizing the formulation of 'rate- and state-dependent' friction (Marone and Scholz, 1989; Mair and Marone, 2000; Sleep and Blanpied, 1992; Dieterich, 1979). The slip instability is attributed to an experimentally welldocumented reduction of the friction coefficient with increase of slip velocity. The present experiments and analysis propose an alternative mechanism for the slip instability that is based on three central observations. First, slip instability occurs only in water-saturated gouge (segment II in the stress-strain curve in Fig. 3.1a and 3.2a). Second, the intensity of slip instability depends on the hold time (stress drop in Fig. 3.2b). Third, the slip instability does not depend on slip velocity as wet and dry samples were subjected to the same loading rates. These observations indicate that the slip instability is due to time-dependent chemical activity (e.g., cementation). Mechanical processes alone (active in both dry and wet samples) could not have generated the observed magnitude of instability. Further, our experiments and those of other workers[10] indicate that chemical processes are more effective than mechanical processes such as frictional healing in (Mair and Marone 2000; Dieterich 1979) in fault-zone strengthening.

Could gouge lithification by chemical processes also be the origin of slip instability during crustal earthquakes (Reches, 1999)? This question is partly addressed in recent investigations of time-dependent changes of fault properties. Analysis of shear wave anisotropy of the 1995 Kobe earthquake area indicates that fault-parallel fractures (NE-SW) dominated the rupture zone for a period of about one year after the earthquake (Tadokoro et al., 1999; Tadokoro and Ando, 2000). In later measurements, 33-45 months after the event[17] this set disappeared, and a new set (E-W) emerged; the latter is oriented parallel to the regional fracture set. Tadokoro et al. (1999), attribute this change to healing of the Nojima fault zone (that produced the 1995 Kobe earthquake). According to the present analysis (Fig. 3.1, 3.2 and 3.3), the Nojima fault observations (Tadokoro et al., 1999; Tadokoro and Ando, 2000) can be interpreted as indicating the filling of open fractures and other chemical processes. This mechanism is supported by direct observations in samples collected in boreholes drilled into the Nojima fault (Moore et al., 2000). These samples show extensive fracture fill by carbonate minerals with up to six episodes of vein filling (Moore et al., 2000). The observations of the Nojima fault show that chemical processes operate at fast rates. In less than three years these processes apparently cemented the earthquake-induced fractures and strengthened the fault-zone to allow new fracturing. Other indicators of in-situ chemical cementation are the temporal variations of the seismic velocity of trapped waves in active fault-zone (Li et al., 1998). They conducted two repeated surveys (1994 and 1996) of the Johnson Valley fault zone that slipped during the 1992 Landers earthquake. The analysis of the trapped waves revealed that the P- and S-wave velocities increased by 0.5-1.5% between the two surveys, suggesting a reduction of crack density (Li et al., 1998). Future measurements of similar phenomena would allow accurate evaluation of the time needed to fully regain fault-zone cohesion and strength.

The hold-slide-hold cycling on water-saturated fault-gouge in the present experiments is an appealing analog for earthquake slip instability. Continued lithification by time-dependent chemical processes during a ten-to-hundred year inter-seismic period would re-form a fault zone into intact rock. The slip instability during subsequent rupture would then be best described as failure of a brittle, cohesive fault-zone. The competition between rates of tectonic loading and rates of lithification could determine the time-to-failure and earthquake recurrence[23]. It appears that earthquake modeling must incorporate time-dependent chemical lithification to generate realistic explanations of the earthquake process.

References

Bernabe, Y., Brace, W.F., 1990. Deformation and fracture of Berea Sandstone. In: Duba, A.G., Durham, W.B., Handin, J.W., Wang, H.F. (Eds), The Brittle Ductile Transition in Rocks: The Heard Volume. American Geophysical Union Monograph 56, 91-101.

Blanpied, M.L., Marone, C.J., Lockner, D.A., Byerlee, J.D., King, D.P., 1998. Quantitative measure of the variation in fault rheology due to fluid-rock interactions. Journal of Geophysical Research 103, 9691-9712.

Byerlee, J., Mjachkin, V., Summers, R., Voevoda, O., 1978. Structures developed in fault gouge during stable sliding and stick-slip. Tectonophysics 44, 161-171.

Dieterich, J.D., Kilgore, B., 1994. Direct observation of frictional contacts; new insights for state-dependent properties. Pure and Applied Geophysics 143, 283-302.

Dieterich, J.D., 1979. Modeling of rock friction: 1. Experimental results and constitutive equations. Journal of Geophysical Research 103, 2161-2168.

Dove, P.M., Crerar, D.A. 1990. Kinetics of quartz dissolution in electrolyte solutions using a hydrothermal mixed flow reactor. Geochimica Cosmochimica Acta 54, 955-969.

Hadizadeh, J. 1994. Interaction of cataclasis and pressure solution in a low-temperature carbonate shear zone. Pure and Applied Geophysics 143, 255-280.

Jeschke, A.A.,Visbeck, K., Dreybrodt, W., 2001. Surface controlled dissolution rates of gypsum in aqueous solutions exhibit nonlinear dissolution kinetics. Geochimica Cosmochimica Acta 65, 27-34.

Karner, S.L., Marone, C., Evans, B., 1997. Laboratory study of fault healing and lithification in simulated fault gouge under hydrothermal conditions. Tectonophysics 277, 41-55.

Li, Y.G., Vidale, J.E., Aki, K., Fei, X., Burdette, T.R., 1998. Evidence of shallow fault zone strengthening after the 1992 M7.5 Landers, California, earthquake. Science 279, 217-219.

Logan, J.M., Dengo, C.A., Higgs, N.G., Wang, Z.Z., 1992. Fabrics of experimental fault zones; their development and relationship to mechanical behavior. In: Evans, B., Wong, T-F (Ed), Fault Mechanics and Transport Properties in Rocks (the Brace volume), Academic, London, pp. 33-67.

Mair, K., Marone, C.,1999. Friction of simulated fault gouge for a wide range of velocities and normal stresses. Journal of Geophysical Research 137, 28899-28914.

Marone, C., Scholz, C.H., 1989. Particle-size distribution and microstructures within simulated fault gouge. Journal of Structural Geology 11, 799-814.

Moore D.E., Lockner, D.A., Ito, H., Ikeda, R., 2000. Proceedings of the International Workshop on the Nojima Fault Core and Borehole Data Analysis. U.S.Geological Survey Open File Report 00-129, 159-165.

Olsen, M.P., Scholz, C.H., Leger, A., 1998. Healing and sealing of a simulated fault gouge under hydrothermal conditions: implications for fault healing. Journal of Geophysical Research 103, 7421-7430.

Power, W.L., Tullis, T.E., Weeks, J.D., 1988. Roughness and wear during brittle faulting. Journal of Geophysical Research 93, 15268-15278.

Raines, M.A., Dewers, T.A., 1997. Mixed transport/reaction control of gypsum dissolution kinetics in aqueous solutions and initiation of gypsum karst. Chemical Geology 140, 29-48.

Reches, Z., 1999. Mechanisms of slip nucleation during earthquake. Earth and Planetary Science Letters 170, 475-486.

Scott, T.E., Nielsen, K.C., 1991. The effects of porosity on the brittle-ductile transition in sandstone. Journal of Geophysical Research 96, 405-414.

Sleep, N.H., Blanpied, M.L., 1992. Creep, compaction, and the weak rheology of major faults. Nature 359, 687-690.

Tadokoro, K., Ando, M., Umeda, Y., 1999. S wave splitting in the aftershock region of the 1995 Hyogo-ken Nanbu earthquake. Journal of Geophysical Research 104, 981-991.

Tadokoro, K., Ando, M., 2000. Evidence for rapid fault healing derived from temporal changes in S wave splitting. EOS Transactions American Geophysical Union 2000 Fall Meeting 81, F1173.

Chapter 4

Time dependent deformation and role of fluids in sealing fault zones

Abstract

Importance of enhanced hydrocarbon recovery and emphasis on description of reservoir heterogeneity has resulted in detailed investigations of fault rocks in both nature and experiments. In mature hydrocarbon provinces such as the North Sea, a purely mechanical description of fault seals in terms of conventional clay smear analysis or shale gouge ratio has resulted in overlooking of seals that are caused by juxtaposition of reservoir units (sand against sand) across the fault. The effectiveness of time-dependent, fluid mediated deformation mechanisms in altering the petrophysical properties of fault rocks are being realized. In this chapter, the close correspondence between mechanical strength and transmissibility properties of fault zone rocks has been illustrated from an experimental investigation using precut blocks of sandstone separated by gypsum gouge. Gypsum is used as an analogue for fault zone minerals because of the fast kinetics of gypsum-water reaction that leads to observable changes within a laboratory time frame.

Behavior of water-saturated fault gouge is in marked contrast to that of dry gouge. Triaxial hold-slide-hold experiments that mimic the displacement

history along active faults indicate that the presence of a reactive fluid in fault zones leads to mechanical strengthening of fault rocks. This also leads to a reduction in permeability beyond that possible solely due to mechanical processes such as cataclasis. Multiple deformation mechanisms such as pressure solution, recrystallization, crack sealing and Ostwald ripening are collectively responsible for lithification of fault gouge after slip thereby altering its strength and petrophysical signatures. It is possible to generate seals in juxtaposed reservoir units due to the above processes and the cement can be sourced entirely from within the fault zone.

Introduction

An economic hydrocarbon accumulation involves presence of a quality reservoir rock, and vertical and lateral seals. Faults are important as lateral seals, and may create and preserve overpressures especially in complex and active extensional tectonic systems such as the US Gulf Coast and the Niger River Delta. Hydraulic properties of faults are difficult to predict as sometimes they act as petroleum migration pathways, often as barriers or baffles, and occasionally provide for oil and gas storage (Yielding et al., 1999; Dholakia et al., 1998; Losh, 1995; Knott, 1993; Bouvier et al., 1989). Risk assessment models try to address the question whether a particular fault is "sealing" or "leaky".

Secondary recovery efforts addressed towards characterization of reservoir heterogeneity need transmissibility properties of faults. Important input parameters for risk assessment models have traditionally included the relative proportion of sand and shale in the system, displacement (slip amount and timing) history of the fault, and potential for juxtaposition of sand against shale (Knipe, 1997; Yielding, et al., 1997; Berg and Avery, 1995). Seals resulting from cataclasis, grain size reduction and compaction in high porosity clastic sedimentary rocks and their effects on fluid flow and permeability have been evaluated in numerous field studies (Antonellini and Aydin, 1994; Fowles and Burley, 1994; Underhill and Woodcock, 1989; Aydin, 1978). Faults can seal not only due to juxtaposition of non-reservoir units but also due to formation of compactional or diagenetic seals during or after slip. Knipe (1997), in a review of more than twenty-five cases of seal investigations from the North Sea suggests that greater than 65% of the seals result from sand juxtaposed against sand and the seals are due to a combination of grain size reduction followed by diagenetic changes. Structural inversion or reactivation may also be responsible for 20% of the North Sea seals investigated. While diagenetic changes have been deemed to be critical on a reservoir scale their importance in changing petrophysical properties of fault rock has not been well studied. However, several investigations allude to the considerable importance of diagenetic effects on transmissibility properties of faults (Labaume and Moretti, 2001; Fisher et al., 2000; Fisher and Knipe, 1998; Sverdrup and Bjorlykke, 1992).

Production of hydrocarbons from fractured reservoirs during enhanced recovery (water-injection) efforts often involves micro-seismic activity and fault/fracture reactivation (Teufel et al., 1991; Rutledge et al., 1994). This may result in loss of permeability as a result of creation of cataclastic fault gouge. Subsequent mineral-water reaction may result in gouge strengthening and larger earthquakes that can lead to loss of wells. The integrity of deep-sea oil and gas production platforms wrestle with subsidence and enhanced compaction especially along faults that affect platform integrity; and, hence, is of considerable economic importance (Boade et al., 1989).

Cementation is thought to be integral to the process of porosity-permeability reduction in reservoir sandstones and especially along fault zones. However, opinion is divided as to whether the cement is derived locally (Bjorlykke and Egeberg, 1993; Bjorlykke, 1994; Fisher et al., 2000) or is imported from elsewhere (Gluyas and Coleman, 1992; Mcbride, 1989). The origin of silica cement has been a long-standing controversy. Geochemical models attest to the problems of transporting significant quantities of cement over a regional scale (Giles, 1997). Local processes that can generate cement are grain contact dissolution (Heald, 1959; Ramm, 1992; Bjorlykke, 1994) or preferential dissolution along stylolites or clay seams (Dewers and Ortoleva, 1990; Oelkers et al., 1996). The presence of clay minerals is thought to enhance dissolution rates or solubility while an abundance of clay possibly eliminates sites for cement precipitation.

It is clear from the above that attention needs to be devoted to non-clay smear seals that can be problematic when attacked from a conventional fault seal analysis perspective or even from a hydrocarbon production point of view. This research concentrates on the interaction between mechanical and chemical processes of fault zones that promotes fault seal development, and results in changes in mechanical properties of faults. A proper understanding of the roles of these mechanisms is necessary to predict sealing potential as secondary recovery efforts in mature petroleum provinces gain importance.

Primary objectives of this study are to investigate (a) whether faults can seal solely due to operative time-dependent chemical processes within the gouge zone, (b) the permeability evolution of laboratory faults in time, and (c) the mechanisms by which sealing is achieved and, (d) whether locally derived cement can produce effective fault seals. Functional dependencies established through this investigation may indirectly benefit risk assessment models aimed at sealing potential of faults.

Experimental Setup

A series of long term, room temperature, triaxial hold-slide-hold experiments have been conducted using calcite and gypsum as fault gouge sandwiched between 30° Berea sandstone precuts. The high permeability of the Berea sandstone allows gouge-sandstone pore pressure equilibration. Calcite and gypsum are treated as analogue fault gouge material because the kinetics of water-rock interaction for these minerals are more amenable for laboratory studies. It was demonstrated in chapter 2 that time-dependent deformation in these minerals occur much like that in quartz rich mineral systems. Samples are 6.35 cm long (including gouge) and 2.54 cm in diameter. Samples are initially loaded hydrostatically to an effective pressure (confining pressure minus pore pressure) of 13.8 MPa and pore pressure of 6.9 MPa. A schematic of the experimental apparatus is given in Figure 4.1. Axial load is applied intermittingly after the initial, hydrostatic hold cycle. Samples are held under triaxial conditions during subsequent hold periods. Permeability is determined immediately before and after slip as well as at regular intervals during the hold period by the steady-state method. An external load cell measures axial load while axial displacement is measured by a DCDT mounted outside the pressure vessel. Volumetric strain measurements are made with a calibrated manual pressure generator. Normal slide duration lasts for about 15 minutes or less, while the hold periods vary from hours to weeks.

The pressure vessel used is a one-of-a-kind design (by John Logan, formerly of Texas A&M University and David Stearns at the University of Oklahoma) and confining pressures of up to 3 Kb can be maintained. Three different hydraulic systems are used to generate confining pressure (Sprague™ pump), pore pressure (Eldex™ HPLC metering pump and Grove-Valve™ back-pressure regulator) and axial load (Enerpac™ ram and Milton Roy pump). All pore pressure tubing and fittings are made of Inconel, titanium, or PEEK and the upper and lower pistons consist of Pyromet. This allows use of corrosive synthetic brines as pore fluid at elevated temperatures.

The stress-strain data acquired during the axial loading stages permits monitoring of shear strength within the gouge during successive slip cycles. The healing behavior of the fault gouge was obtained from changes of pore fluid volume during the inter-slip periods. This was correlated with the strength data acquired during periods of sliding. Textural analysis using optical and electron microscopy was undertaken on the run products to study the deformation mechanisms related to the processes of healing and sealing of the laboratory gouge zones.

Synthetic gypsum gouge (naturally rounded gypsum sand from White Sands National Monument) having a thickness of 4 mm was used in hold-slide-hold experiments over durations of up to 8 weeks. Each experiment began with a hydrostatic hold period; during subsequent hold periods the axial stroke and confining pressure were maintained constant and the axial load was allowed to relax (due to gouge creep). In a slide stage, samples were axially shortened under axial strain rates of $2.6 \times 10^{-5} s^{-1}$ to a pre-determined strain (typically 1-2% axial shortening). The pore fluid volume was monitored using a volumometer with a resolution of $0.0047 \ cm^3$. Four experiments were run water-saturated and one nominally dry with gypsum gouge while a single experiment was run with calcite as the gouge mineral under drained conditions.

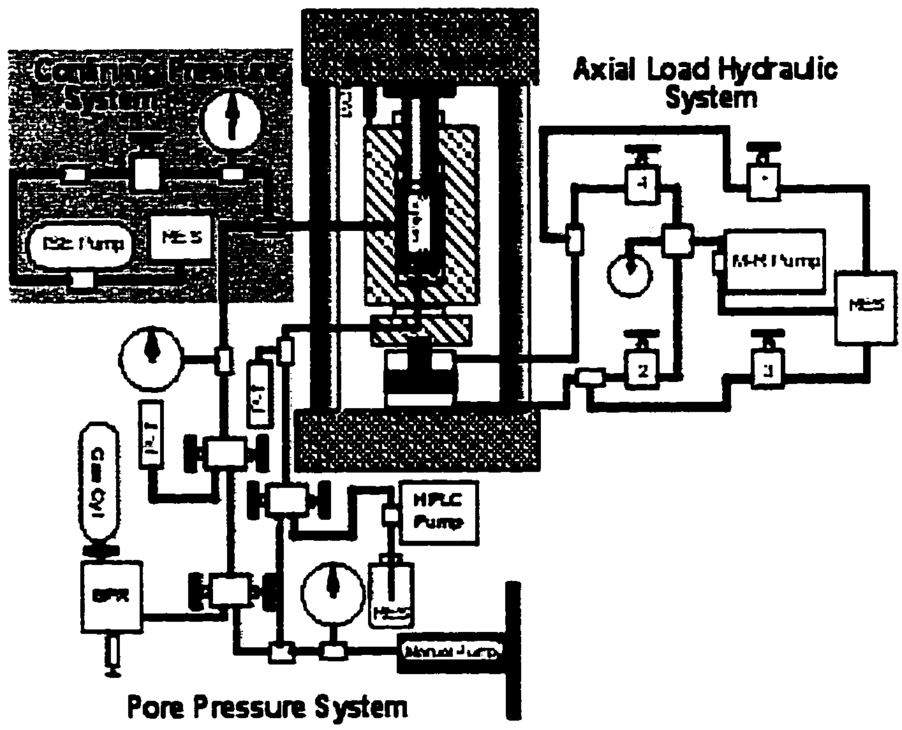

Fig. 4.1: Schematic of the experimental apparatus for long-term hold-slide hold tests [Various valves have been numbered, BPR = back pressure regulator, TP = pressure transducer, TSE pump = Sprague pump used for confining pressure, M-R pump = Milton Roy pump for ram, HPLC = high pressure liquid chromatography pump used for permeability measurements and application of pore pressure].

Results

Stress-strain data

Results from a representative experiment with 5 hold-slide cycles are shown in Figure 4.2a. Initial hydrostatic hold period for this test is about three weeks. The first slide cycle (S1) is dominated by compaction of unconsolidated gouge and hence exhibits a short linear section. Subsequent slide cycles (S2 through S5) are more typical of sliding friction experiments with gouge in that they exhibit a steep linear section until a maximum or peak strength is reached. The quasi-linear slope for the initial part of this segment is 14.5 GPa, which approximates the weighted Young's modulus of Berea Sandstone with 4mm thick gypsum gouge (see Appendix A); this slope indicates negligible inelastic gouge deformation during this segment of loading. Once peak strength was reached failure resulted in an appreciable stress drop to the level of residual strength with an associated increase of pore volume (dilatancy). The shear stress then remained at a near-constant level (the residual sliding friction strength) that reflects stable sliding within the gouge. Once the axial shortening was stopped the shear stress relaxed during the hold period. An increase in peak shear strength is observed in these experiments (e.g. compare S2 and S3) that was not commonly observed in previous short-term experiments using precut samples with an intervening layer of unconsolidated gouge. Also, there is a stress drop once the sample reaches maximum shear strength that is observable in most cycles (S2, S3 and S5). These stress drops as well as the

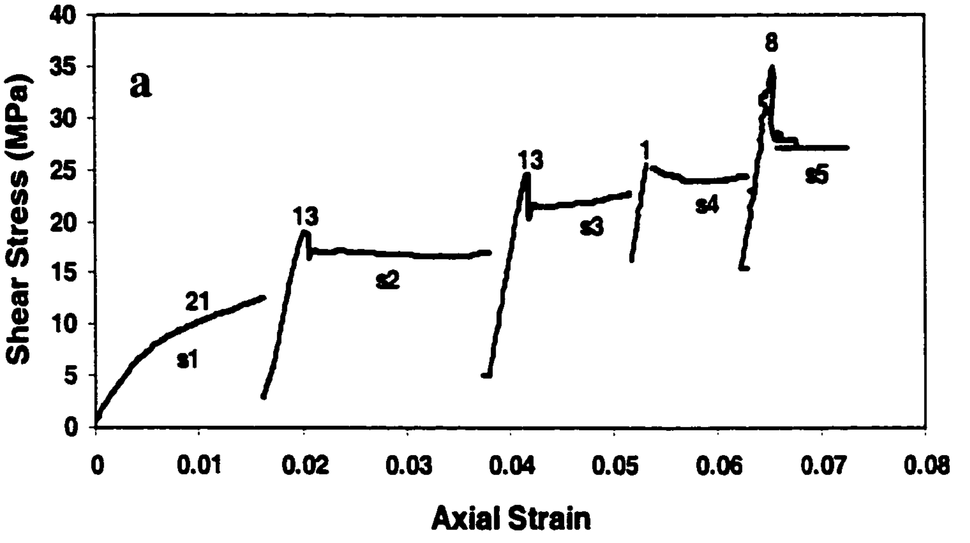

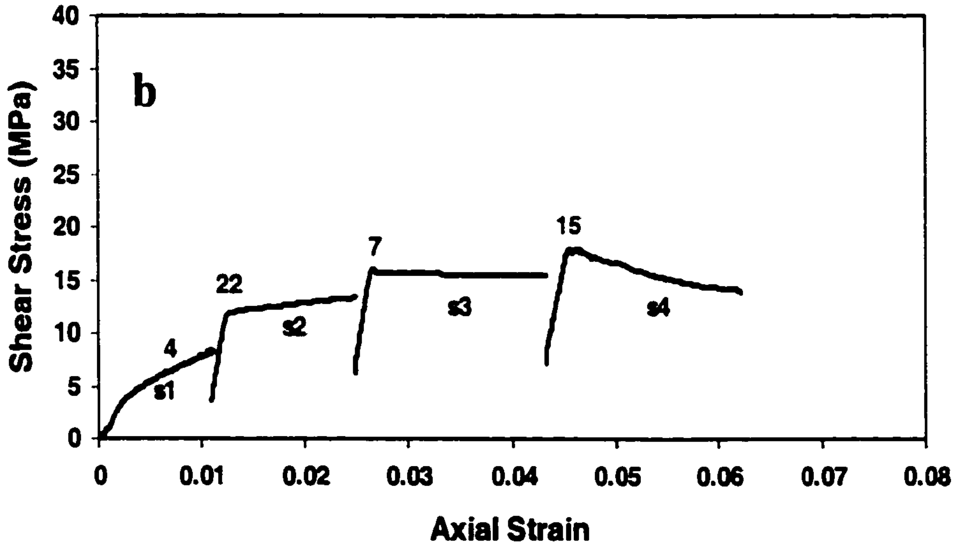

Fig. 4.2a. Above is a shear stress-axial strain plot of a long-term hold-slide-hold experiment showing 5 separate slide cycles (S1-S5) over a period of about two months. There is clear evidence for development of cohesion in the gouge (note peak strength and stress drop). Cohesion is minimal when the hold period is only one day (S4). Numbers reflect hold period in days for previous cycle. (b) Shear stress plotted against axial strain for a dry hold-slide-hold test with four slide events. In each slide cycle the shear stress builds up rapidly followed by stable sliding along the precut. In contrast to Fig. 4.2a development of any marked peak strength or stress drop (cohesion), though there is an increase in the residual strength.

increase in shear strength suggests that the fault gains cohesion or "heals" during the hold period. In one instance (S4), where the preceding hold period was about 24 hours as opposed to weeks for the other cycles, there was no observable stress drop or increase in maximum shear strength (compare to S3) indicating a time-dependence to the strengthening process.

Another experiment under identical effective pressure conditions with a room-dry dry sample was conducted at a confining pressure of 13.8 MPa (Fig. 4.2b). After an initial compaction phase, the gouge was subjected to four hold-slide cycles with hold periods between 4 and 22 days. During the initial loading phase of each cycle, the shear stress increased in a linear manner (Young's Modulus of 14.7 GPa similar to wet experiment). Following the initiation of sliding, the stress-strain slope decreased to a quasi-constant value that reflects stable sliding along the dry gouge zone. Similar stress-strain behavior is observed in many sawcut experiments with much shorter duration.

It is important to note that the peak stress and the following stress drop that dominated the previously described water-saturated tests were clearly absent in dry experiments (compare Fig. 4.2a and b). This difference can be attributed to the time-dependent chemical processes that could operate only in the water-saturated tests, whereas the mechanical processes such as grain breakage were active in both dry and water-saturated tests. Significant strengthening (increase in peak strength) occurs in a time-dependent manner in all water-saturated experiments (see Fig. 3.1a and 3.2 in Chapter 3).

Gouge compaction and permeability evolution

Pore volume changes in the gouge due to compaction both during hold and slide cycles was measured and has been shown in Figure 4.3. Pore volume changes occur due to changes in porosity concomitant with deformation. Pore volume change occurs faster immediately following every loading cycle and then slows with time i.e. the rate of change of pore volume is greater immediately following slip (steep slope immediately after S1 or S2 that decreases with time in Fig. 4.3). Various mechanisms that may lead to evolution of gouge texture such as grain inter-penetration or suturing, compaction and any cement precipitation within the gouge result in loss of porosity. The permeability decreases during the initial slide cycles (S1 and S2), but not significantly during subsequent slide cycles (S3 and S4, Fig. 4.3). This suggests that a steady-state in porosity may be reached with increased fault slip (mature faults) where the effects of additional porosity created by fracturing is negated by closure of pore throats due to fining of the grain size distribution. The permeability-time data (Fig. 4.3) shows a small but consistent decrease in permeability during all hold cycles ("sealing" of fault gouge). The decrease is more rapid in initial cycles compared to latter ones.

Pore volume loss data was used to compute gouge porosity assuming negligible deformation in the Berea sandstone enclosing the layer of gypsum gouge. As the maximum strength reached during these experiments is within the elastic limits of the stiffer sandstone this is a valid assumption to make. In Figure 4.4 the measured permeability is plotted against gouge porosity

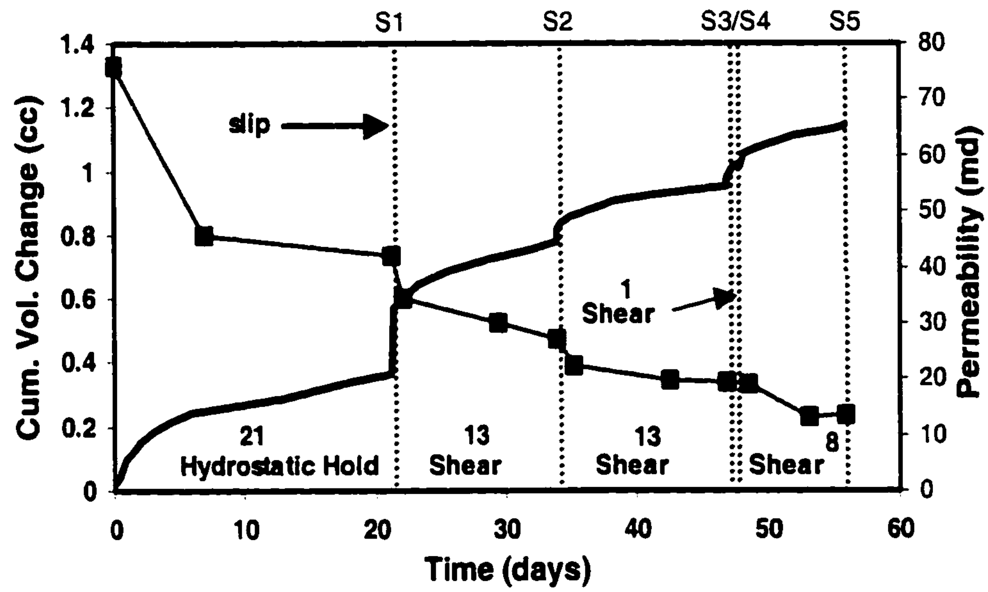

Fig. 4.3: Compaction-time (black curve) and permeability–time plot (grey curve) for the experiment in Fig. 4.2a. Cumulative pore volume change (gouge and sandstone)[1] shows the non-linear nature of time-dependent compaction during each hold period with a higher compaction-rate early in the experiment. Permeability-time relationship (secondary vertical axis) mimics the compaction trend with a decrease in permeability during the hold period. This reduction is due to time-dependent deformation described in the text. Permeability also drops during shear due to granulation but the effect is subdued at greater shear strains. S1-S5 are the shear events plotted in Fig. 4.2a. Numbers are the post post-slip hold periods in days. Note that the initial hold period is hydrostatic while the subsequent hold periods are all under shear loading.

[1] An experiment using similar precut sample geometry but no gouge was conducted at identical effective pressure conditions as above to isolate pore volume changes in the Berea sandstone. The results are not presented here. A maximum compaction (volumetric strain) of 0.02% (equivalent to 0.001 cc) was recorded during pre-peak axial loading. This is more than an order of magnitude lower than the compaction recorded in the gouge (reported above) alone. During post-peak sliding no pore volume change was recorded in the absence of gouge. No time-dependent creep in Berea sandstone in the absence of gouge was observed.

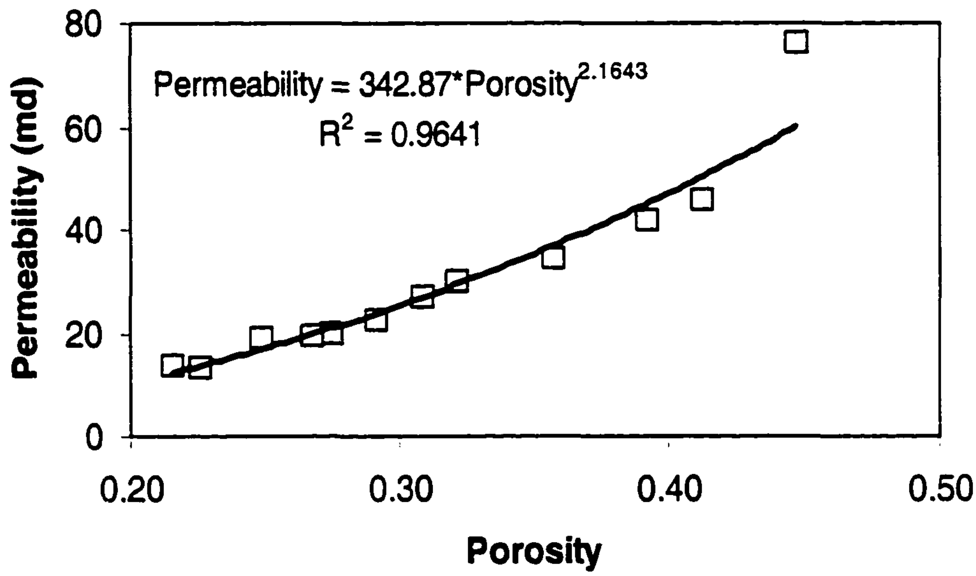

Fig. 4.4: Gouge porosity (calculated from Fig. 4.3) plotted against total effective permeability measured for a single hold-slide-hold experiment. Porosity within the gouge is computed from pore volume change data assuming an initial porosity of 40% (obtained by the water displacement technique). Permeability is measured by the steady-state method at various points during the experiment. An increase in shear strain and time results in a decrease in porosity due to changes in gouge texture. Permeability measured decreases as a power-law function of porosity in the gouge.

A consistent decrease in the permeability can be observed simultaneously with the reduction of porosity within the gouge. A power-law function adequately describes the observations and also predicts zero permeability at vanishingly small values of porosity in the fault gouge.

Deformation of calcite gouge

In order to test whether the evolution of fault strength and porosity-permeability is due to chemical control on sealing a similar experiment was also conducted under identical effective pressure and temperature conditions using calcite as the gouge. Calcite-water reaction kinetics at room temperature is slower than that of gypsum in water by about two orders of magnitude (Plummer et al., 1978; Raines and Dewers, 1997). A 4 mm calcite gouge having a grain size of 63-125 μm was used. The shear stress-axial strain plot for this experiment is shown in Figure 4.5. The results are similar to the gypsum experiments with one notable exception: the calcite experiment lacks evidence for "healing" as no increase in maximum shear strength, or a stress drop at maximum shear strength is observed. Results are similar phenomenologically to the dry gypsum experiment in that no cohesion is achieved within the wet calcite gouge (compare Fig 4.5 and 4.2b). Volumetric strain accumulated during hold cycles due to porosity loss is negligible and the data has not been reproduced here. Permeability-time data for this experiment exhibits marked reduction only during slide events but negligible changes during hold periods.

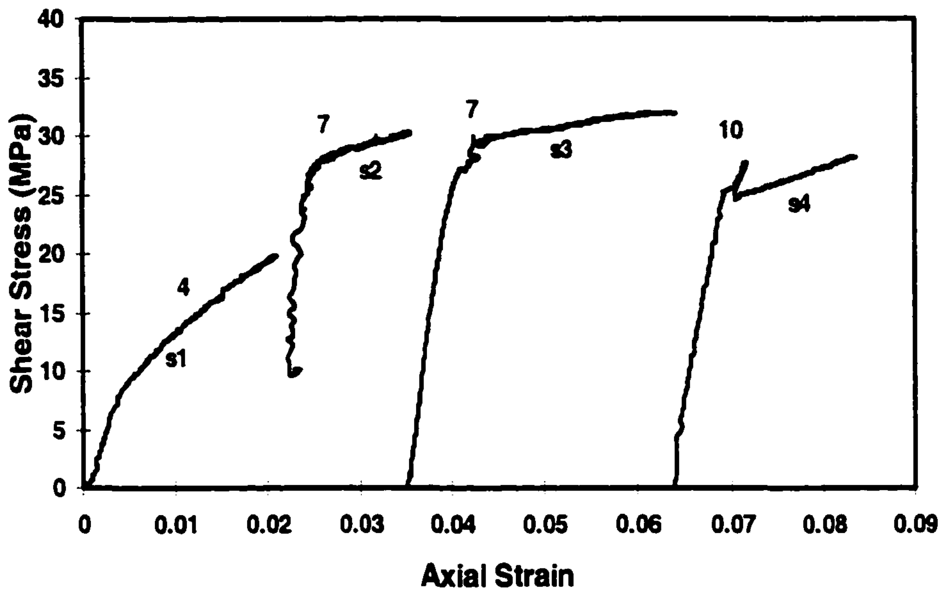

Fig. 4.5: Shear stress plotted against axial strain for a room temperature, hold-slide-hold test using calcite gouge within Berea saw-cuts. Effective pressure for the test maintained at 13.8 MPa and pore pressure held constant at 6.8 MPa. Total duration of the experiment is one month. In contrast to the gypsum experiments (Fig. 4.2a) this shows no development of cohesion or peak strength over the four slip cycles.

Deformation mechanisms

The sealing and strengthening mechanisms that led to decrease in permeability during hold periods as well as to significant increase in fault strength were further explored by microscopic analysis of gouge material from water-saturated and dry experiments. Optical and SEM photomicrographs of experimental gouge (Fig. 4.6a, Fig. 4.7 and 4.8) reveal deformation mechanisms responsible for the reduction in porosity and provide evidence for gouge lithification. Figure 4.6a and 4.6b are photomicrographs of two gouge samples deformed wet and dry, respectively. The dry gouge exhibits a smaller degree of compaction (thicker gouge, compare thickness of the gouge in Fig. 4.6a and b) even though both experiments were run over similar displacements and time. Inter-granular porosity was commonly observed in dry gouge (Fig. 4.6b) and the rounded grain boundaries were retained after deformation. In addition, open microfractures were also ubiquitous. In stark contrast, deformed wet gouge exhibits near total obliteration of porosity and lack of clearly defined grain boundaries (Fig. 4.6a). Wet gouge texture also indicates recrystallization as evident from polygonal grain contacts (Fig. 4.7a). Microfractures in the wet gouge show evidence of partial filling with cement or are present as relict fluid inclusion trails (Fig. 4.7b). These trails were probably formed due to microfracture healing or may also be due to migration of grain boundaries (Blenkinsop, 2000). Pressure solution is perhaps the most widespread fluid mediated deformation mechanism observed in the deformed wet gouge from these experiments. Welding of grain contacts (Fig. 4.8 and Fig. 4.6a) and

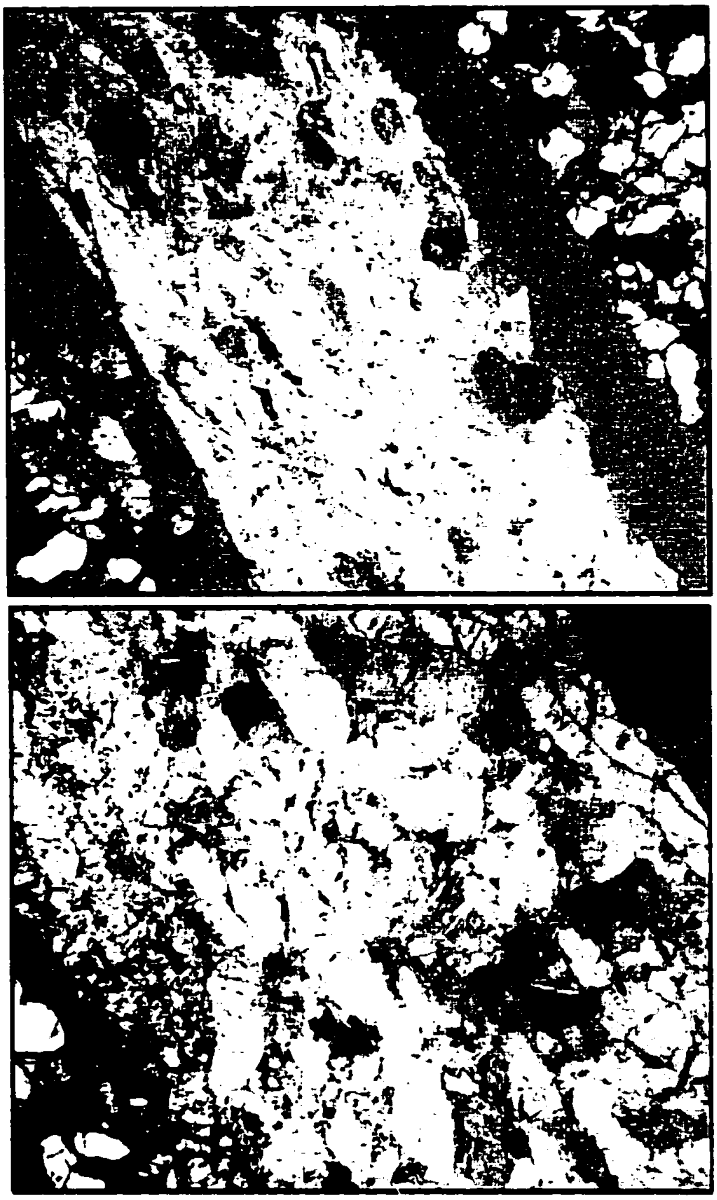

Fig. 4.6a. Optical photomicrograph taken in plane polarized light for wet gouge deformed over a period of about two months (P_e=13.8MPa, axial strain 8%). The deformed gouge zone is about 3mm wide. Notable are total absence of any inter-granular porosity and lack of clear grain contacts. (b) Photomicrograph of room dry gouge deformed under identical conditions. The gouge zone is about 4mm wide. In contrast to the wet gouge inter-granular porosity (blue dyed epoxy areas) is clearly visible and individual grain outlines are also well defined.

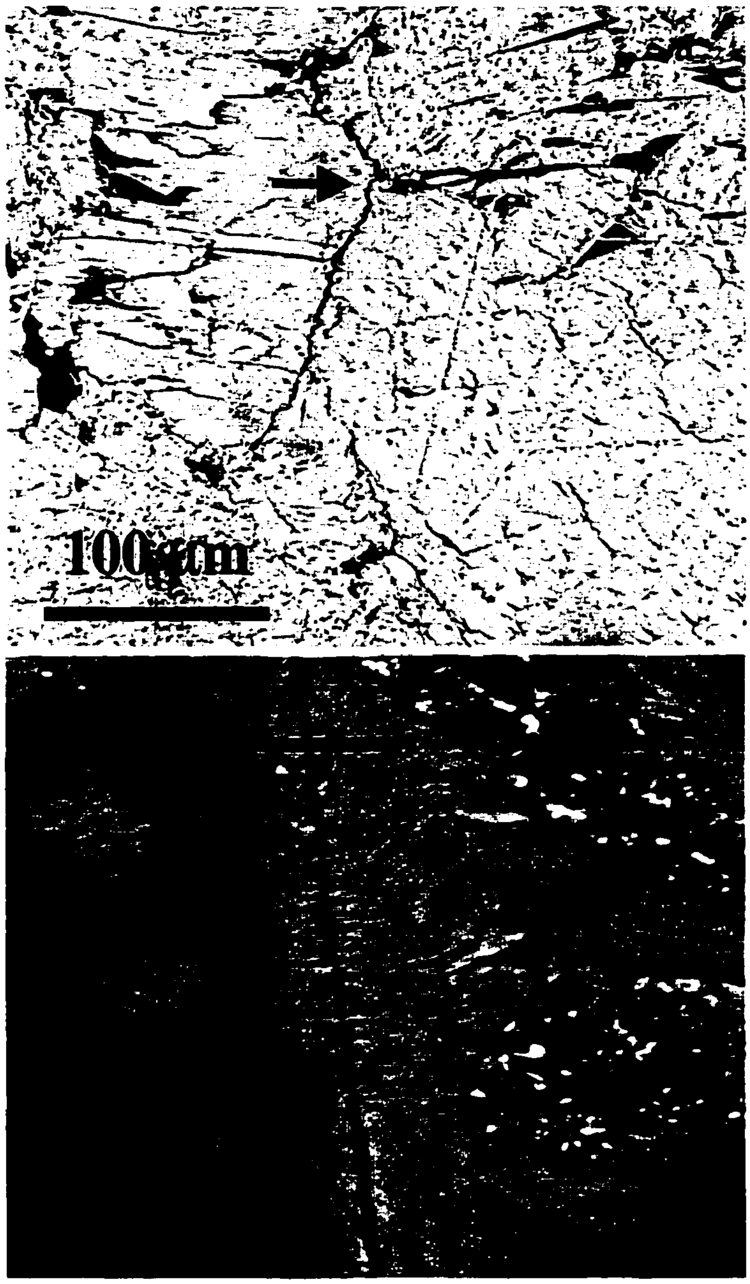

Fig. 4.7a. Back scattered electron (BSE) photomicrograph of gypsum gouge deformed under wet conditions. A triple-junction indicating recrystallization of the gouge during deformation is noted. (b) BSE image of a partially sealed microfracture within a grain of gypsum. Also note the array of fluid inclusion trails suggesting healed microfractures.

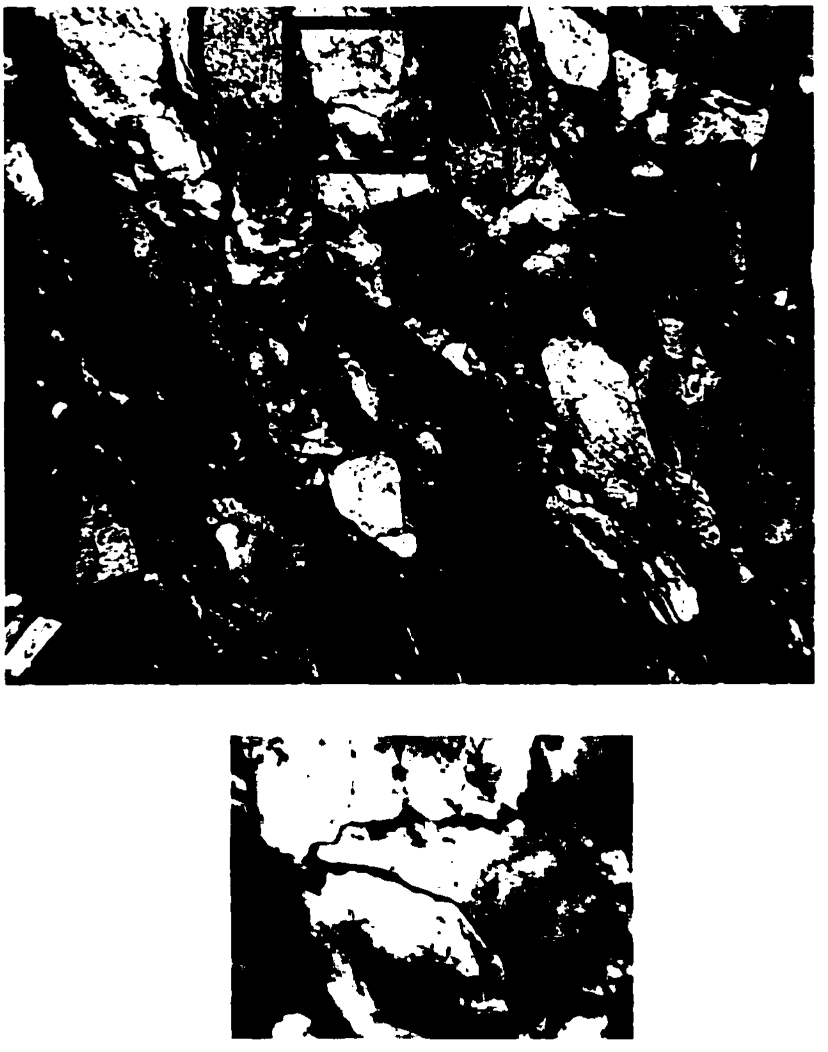

Fig. 4.8. Optical photomicrograph for wet gypsum gouge in long-term hold-slide-hold experiment. Overall texture suggests both brittle (granulation) and ductile deformation. Inset illustrates a sutured grain contact indicating pressure solution that is ubiquitous in these experiments. Field of view for the top photomicrograph is 2 mm.

intense suturing at grain boundaries are especially common (Fig. 4.8, inset). Similar features were absent in dry gouge zones. Dry gouge microstructures include extensive microfracturing and granulation as well as evidence for crystal plastic deformation such as kinks. These features, produced during slip in all experiments, were completely obliterated in the water-saturated experiments over the long hold-times involved. Similar textural evidence for pressure solution, microfracture healing, recrystallization and cementation, are common in exhumed fault rocks of all ages and tectonic regimes (Labaume and Moretti, 2001; Blenkinsop, 2000; Hadizadeh, 1994; Chester and Logan, 1987).

Discussion

Permeability destruction due to movement of solute bearing fluid through a rock body has been a commonly invoked model to explain observed cementation along fractures or fault zones (McBride, 1989; Gluyas and Coleman, 1992). This requires extensive fluid-flow along a low-permeability fault zone. According to this model the cement may be sourced by: compacting mudrocks, underlying sandstones, convective transport or even fault-related fluid-flow (Burley, 1993; Wood and Hewett, 1984). However, the problems associated with transporting large amounts of dissolved silica to explain extensive quartz cementation in nature are thought to be considerable even assuming favorable fracture networks (Giles, 1997; Fisher et al., 2000). The solubility of silica at diagenetic temperatures and flow rates typical for sedimentary basins are unfavorable for transporting large volumes of cement by advection. A number of mechanisms of "local" cement generation with minimal subsequent transport (<1m) have been identified. These include: pressure solution at grain contacts (Bjorlykke, 1994; Ramm, 1992; Heald, 1959), quartz dissolution along stylolites (Oelkers, 1996; Dewers and Ortoleva, 1990) and feldspar dissolution (Bjorlykke and Egeberg, 1993). Indeed, geochemical modeling suggests that quartz cement in North Sea Jurasssic sandstones were derived from stylolitization (Fisher et al., 2000).

Pressure solution drives material from grain contacts to free-surfaces where it precipitates as cement. Ostwald ripening can also serve as a source of cement as a high proportion of very-fine sub-micron sized particles are kinetically favored for ripening (Morse and Casey, 1988; Steefel and Van Capellen, 1990; Sleep, 1995). Fault rocks have been observed to experience enhanced cementation (Fisher and Knipe, 1998). Fisher et al., (2000) note that at least 10% of the deformed rocks from the North Sea contain more cement relative to undamaged country rock. The observations on natural fault rocks are not unique and similar processes can be noted in photomicrographs of experimentally deformed samples from this study. Welded grain contacts suggesting ubiquitous pressure solution activity (Fig. 4.6a and 4.8), evidence for recrystallization (Fig. 4.7a), partial filling of microfractures and completely healed fractures identified by fluid-inclusion trails (Fig. 4.7b) were commonly observed. In addition, most photomicrographs indicate considerable loss of porosity during deformation (Fig. 4.6a, 4.7, 4.8). An approximately eight-fold reduction in observed permeability (Fig. 4.4) over a period of couple of months is caused by the destruction of porosity. Permeability of various clay rich fault rocks (5-25% clay) in the North Sea have been observed to vary over two orders of magnitude. These rocks have a similar particle size distribution and their permeability is a function of the extent of time-dependent deformation processes (Fisher et al., 2000).

It is argued that the porosity and permeability reduction in these experiments especially at larger shear strains is due to locally sourced cementation. Cataclasis during shear events results in a reduction in grain size. Finer grain sizes are more susceptible to higher rates of pressure solution and Ostwald ripening (Maliva and Siever, 1988; Morse and Casey, 1988; Steefel and Van Capellen, 1990; Sleep, 1995). It has to be noted that clays were absent in these experiments and their presence could further enhance the rate of mass redistribution within the gouge zone. However, locally derived cements may be patchy in spatial distribution and therefore may not be capable of supporting thick hydrocarbon columns. The effectiveness of particle size reduction within the gouge is dependent on the depth of burial (mean stress) and the amount of shear strain. Shallow burial would tend to reduce the effect of cataclasis within the gouge (Logan, 1992) and require shear strains in excess of 100 (Fisher and Knipe, 1998). Moreover, the kinetics of fluid-mineral reactions is sluggish if the deformation occurs at shallow depths (<3 Km). The timing of hydrocarbon migration and any resultant contamination may result in inhibiting pressure solution due to the presence of chemically inert fluids (Worden et al., 1998).

From the above discussion it appears that locally derived cements from within the fault zone are common in both experiments and nature. Reduction in porosity leads to re-strengthening of fault zones (Fig. 4.2a) and significant changes in the permeability (Fig. 4.3, 4.4). However, field data favoring such seals as being able to support thick hydrocarbon columns is currently unavailable. Deformation at depths (>3 Km) may be more conducive for cementation fault seals to be economically important.

Conclusions

An experimental design that mimics the structural history of many fault zones in nature was used to investigate the evolution of mechanical strength, porosity and permeability. Hold-slide-hold experiments using Berea sandstone as country rock and an intervening layer of gypsum gouge suggests that mechanical strength of fault zones increase in a time-dependent manner. Mechanical test results are characterized by an increase in shear strength with time and an unstable failure suggesting development of cohesion within the gouge. This increase was only observed when a reactive pore fluid was present in the system. Time-dependent, fluid mediated chemical processes such as pressure solution, crack sealing and Ostwald ripening operating in conjunction with mechanical cataclasis promotes re-strengthening. A control experiment using calcite gouge saturated with water, exhibited deformation characteristics similar to dry gypsum.

Deformation mechanisms that lead to fault zone strengthening also lead to permeability reduction. Experimental observations suggest that time-dependent deformation processes such as pressure solution may have a greater efficiency in reducing permeability in fault zones relative to mechanical grain crushing. Similar observations have been reported from several North Sea reservoirs (Fisher and Knipe, 1998). Juxtaposed reservoir units may seal even with the presence of negligible quantities of clay minerals.

The cementation and lithification of the gouge in the experiments is driven entirely from within the fault zone and does not require long-distance solute transport through the fault. This provides independent experimental verification for "locally-derived" origin for cement (Dewers and Ortoleva, 1990; Ramm, 1992 and others). The effectiveness for cementation seals in supporting economic hydrocarbon columns need to be further evaluated especially for deeply buried fault rocks.

References

Antonellini, M.A., Aydin, A., 1994. Effect of faulting on fluid flow in porous sandstones: Petrophysical properties. American Association of Petroleum Geologists Bulletin 78, 355-377.

Aydin, A., 1978. Small faults formed as deformation bands in sandstone. Pure Applied Geophysics.116, 913-930.

Berg, R.R., Avery, A.H., 1995. Sealing properties of tertiary growth faults, Texas Gulf Coast. American Association of Petroleum Geologists Bulletin 79, 375-393.

Bjorlykke, K., 1994. Fluid-flow processes and diagenesis in sedimentary basins. In: Parnell, J. (Ed.), Geofluids:origin, migration and evolution of fluids in sedimentary basins. Geological Society Special Publication 78, 127-140.

Bjorlykke, K., Egeberg, P.K., 1993. Quartz cementation in sedimentary basins. American Association of Petroleum Geologists Bulletin 77, 1538-1548.

Blenkinsop, T., 2000. Deformation Microstructures and Mechanisms in Minerals and Rocks. Kluwer, Dordrecht, 150p.

Boade, R.R., Chin, Y.L., Seimers, W.T., 1989. Forecasting of Ekofisk reservoir compaction and subsidence by numerical simulation. Journal of Petroleum Technology, 723-728.

Bouvier, J.D., Sijpestein, K., Kleusner, D.F., Onyejekwe, C.C., Van Der Pal, R.C., 1989. Three-dimensional seismic interpretation and fault sealing investigations, Nun River field, Nigeria. Ammerican Association of Petroleum Geologists Bulletin 73, 1397-1414.

Burley, S.D., 1993. Models of burial diagenesis for deep exploration plays in Jurassic fault traps of the Central and Northern North Sea. In: Parker, J.R. (Ed.), Petroleum Geology of Northwest Europe, Geological Society of London, pp. 1353-1375.

Chester, F., Logan, J., 1987. Composite planar fabric of gouge from the Punchbowl Fault, California. Journal Structural Geology 9, 621-634.

Dewers, T.A., Ortoleva, P., 1990. A coupled reaction/transport/mechanical model for intergranular pressure solution, stylolites, and differential compaction and cementation in clean sandstones. Geochimica Cosmochimica Acta 54, 1609-1625.

Dholakia, S.K., Aydin, A., Pollard, D.D., Zoback, M.D., 1998. Fault-controlled hydrocarbon pathways in the Monterey formation, California. American Association of Petroleum Geologists Bulletin 82, 1551-1574.

Fisher, Q.J., Knipe, R.J., 1998. Fault sealing processes in siliciclastic sediments. In: Jones, G., Fisher, Q.J., Knipe, K.J. (Eds.), Faulting, Fault Sealing and Fluid Flow in Hydrocarbon Reservoirs. Geological Society of London Special Publication 147, pp. 117-134.

Fisher, Q.J., Knipe, R.J., Worden, R.H., 2000. Microstructures of deformed and non-deformed sandstones from the North Sea: implications for the origin of quartz cement in sandstones. In: Worden, R., Morad, S. (Eds), Quartz Cementation in Sandstones. International Association of Sedimentologists Special Publication 29, pp.129-146.

Fowles, J., Burley S.D., 1994. Textural and permeability characteristics of faulted, high porosity sandstones. Marine Petroleum Geology 11, 608-623.

Giles, M., 1997. Diagenesis and its Impact on Rock Properties. A Quantitative Perspective. Kluwer, Amsterdam, 520p.

Gluyas, J.G., Coleman, M., 1992. Material flux and porosity changes during sediment diagenesis. Nature 356, 52-54.

Hadizadeh, J., 1994. Interaction of cataclasis and pressure solution in a low-temperature carbonate shear zone. Pure Applied Geophysics143, 255-280.

Heald, M.T., 1959. Significance of stylolites in permeable sandstones. Journal of Sedimentary Petrology 29, 251-253.

Jaeger, J.C. Cook, N.G.W., 1979. Fundamentals of Rock Mechanics. Chapman and Hall, New York, 593p.

Knipe, R.J., 1992. Faulting processes and fault seals. In: Larsen, R.M., Brekke, H., Larsen, B.T., and Telleraas, E., (Eds.). Structural and Tectonic Modeling and its Applications to Petroleum Geology. Norwegian Petroleum Society Special Publication 1, pp. 325-342.

Knipe, R.J., 1997. Juxtaposition and seal diagrams to help analyze fault seals in hydrocarbon reservoirs. American Association of Petroleum Geologists Bulletin 81, 187-195.

Knott, S.D., 1993. Fault seal analysis in the North Sea. American Association of Petroleum Geologists Bulletin 77, 778-792.

Labaume, P., Moretti, I., 2001. Diagenesis-dependence of cataclastic thrust fault zone sealing in sandstones. Example from the Bolivian sub-Andean zone. Journal of Structural Geology 23, 1659-1675.

Logan, J.M., 1992. The influence of fluid-flow on the mechanical behavior of faults. In: Tillerson, J.R., Wawersik, W.R., (Eds), Rock Mechanics, Balkema, Rotterdam, pp. 141-149.

Losh, S., 1998. Oil migration in a major growth fault: structural analysis of the Pathfinder core, south Eugene Island Block 330, offshore Louisiana. American Association of Petroleum Geologists Bulletin 82, 1694-1710.

Maliva, R.G., Siever, R., 1988. Mechanisms and controls of silicification of fossils in limestones. Journal of Geology 96, 387-398.

McBride, E.F., 1989. Quartz cement in sandstones-a review, Earth Science Review 26, 69-112.

Mavko, G., Mukerji, T., Dvorkin, J., 1998. The Rock Physics Handbook: Tools for Seismic Analysis in Porous Media. Cambridge, New York, 329pp.

Morse, J.W., Casey, W.H., 1988. Ostwald processes and mineral assemblages in sediments. American Journal of Science 288, 537-560.

Oelkers, E.H., Bjorkum, P.A., Murphy, W.M., 1996. A petrographic and computational investigation of quartz cementation and porosity reduction in North Sea sandstones. American Journal of Science 296, 420-452.

Olgaard, D.L., Ko, S-C., Wong, T-F., 1995. Deformation and pore pressure in dehydrating gypsum under transiently drained conditions. Tectonophysics 245, 237-248.

Plummer, L.N., Wigley, M.L., Parkhurst, D.L., 1978. The kinetics of calcite dissolution in CO_2-water systems at 5-60°C and 0.0 -1.0 atm CO_2. American Journal of Science 278, 179-216.

Raines, M.A., Dewers, T.A., 1997. Mixed transport/reaction control of gypsum dissolution kinetics in aqueous solutions and initiation of gypsum karst, Chemical Geology 140, 29-48.

Ramm, M., 1992. Porosity-depth trends in reservoir sandstones: offshore Norway, Marine and Petroleum Geologists 9, 553-567.

Rutledge, J.T., Fairbanks, T.D., Albright, J.N., Boade, R.R., Dangerfield, J., Landa, G.H., 1994. Reservoir microseismicity at the Ekofisk oil field. Eurock, Balkema, Rotterdam, 589-595.

Sleep, N.H., 1995. Ductile creep, compaction, and rate and state dependent friction within major fault zones: Journal of Geophysical Research 100, 13065-13080.

Steefel, C.I., Van Cappellen, P., 1990. A new kinetic approach to modeling water-rock interaction: the role of nucleation, precursors and Ostwald ripening. Geochimica Cosmochimica Acta 54, 2657-2677.

Sverdrup, E., Bjorlykke, K., 1992. Small faults in sandstones from Spitsbergen and Haltenbanken. A study of diagenetic and deformational structures and their relation to fluid flow. In: Larsen, R.M., Brekke, H., Larsen, B.T., and Telleraas, E., (Eds), Structural and Tectonic Modeling and its Applications to Petroleum Geology. Norwegian Petroleum Society Special Publication 1, pp. 507-515.

Teufel, L., Rhett, D.W., Farrell, H.E., 1991. Effect of reservoir depletion and pore pressure drawdown on in situ stress and deformation in the Ekofisk Field, North Sea. In: Roegiers, J-C. (Ed), Rock Mechanics as a Multidisciplinary Science, Balkema, Rotterdam, pp. 63-72.

Underhill, J.R., Woodcock, N.H., 1987. Faulting mechanisms in high-porosity sandstones, New Red Sandstone, Arran, Scotland. In: Jones, M.E., and Preston, R.M.F. (Eds), Deformation of Sediments and Sedimentary Rocks. Geological Society Special Publication 29, pp. 91-105.

Wood, J.R. Hewett, T.A., 1984. Reservoir diagenesis and convective fluid flow. In: McDonald, D.A., Surdam, R.C. (Eds), Clastic Diagenesis, American Association of Petroleum Geologists Memoir 37, pp. 99-110.

Worden, R.H., Oxtoby, N.H., Smalley, P.C., 1998. Can oil emplacement stop quartz cementation in sandstones? Petroleum Geoscience 4, 129-138.

Yielding, G., Freeman, B., Needham, D.T., 1997. Quantitative fault seal prediction. American Association of Petroleum Geologists Bulletin 81, 897-917.

Yielding, G., Overland, J.A., Byberg, G., 1999. Characterization of fault zones for reservoir modeling: an example from the Gullfaks Field, northern North Sea. American Association of Petroleum Geologists Bulletin 83, 925-951.

Appendix 4A: Determination of Weighted Young's Modulus

An estimate of the weighted Young's modulus of the precut Berea sandstone gypsum sample was determined using the Voigt and Reuss effective media bounds for elastic moduli (Mavko et al., 1998). The volume fractions and Young's moduli for Berea sandstone and porous gypsum gouge are required for the determination.

The Voigt upper bound (also called the isostrain average) gives the ratio of average stress to average strain where the constituents are assumed to have undergone the same strain. Generally, the Voigt bound is stiffer than most physical systems. This is given by:

$$M_v = \sum_{i=1}^{N} f_i M_i$$

where, f_i represents the volume fraction of the constituent i and M_i the modulus. The Reuss lower bound (also called the isostress average) gives the ratio of average stress to average strain where the constituents are assumed to be under the same stress. The Reuss average describes effective moduli of suspensions or shattered fragments enclosed in pore fluid. This is given by:

$$M_R = \sum_{i=1}^{N} \frac{f_i}{M_i}$$

Another effective moduli commonly used is the Voigt-Reuss-Hill average which is the mean of the Reuss and Voigt bounds and may be more realistic in describing rocks in the crust.

The first step is to calculate the effective Young's Modulus for porous gypsum aggregate with an initial porosity of 40% in the presence of pore water. A Voigt-Reuss-Hill average was obtained using Young's modulus for intact gypsum (3% porosity, 15 GPa reported in Olgaard et al., 1995). The Young's modulus for Berea sandstone used in the study was determined to be 18 GPa. The weighted (Voigt-Reuss-Hill) average for the Young's modulus obtained using the above moduli and respective volume fractions of the sandstone and gouge was calculated to be 16.6 GPa. This value is within 2% of the observed value for a single cycle from the dry experiment (Fig. 4.2b).

Appendix 4B: Experimental Procedure

The experimental procedure followed for the hold-slide-hold experiments conducted using Berea sandstone precuts and gypsum or calcite as fault gouge is given below:

1. A 2.5 cm diameter core of Berea sandstone was cut from a pre-selected block having a porosity of about 20% and a permeability of about 100 milidarcies. Each core is about 15 cm long. Berea sandstone is chosen because it is fairly homogeneous at the scale of the samples. Moreover the high porosity and permeability allows nearly instantaneous pore fluid communication between the ends of the sample and to the gouge.
2. A 30° (to the cylinder axis) precut was put exactly in the middle of the 15 cm long core. The precut was made using a rock-cutting saw. Sliding friction envelope (in σ–τ space) for Berea sandstone suggests 28°-31.5° to be a favorable range of angles (Jaeger and Cook, 1969). Larger angles are more prone to exhibiting stick-slip like instability.
3. The surface of the precut was ground to a 60 grit finish using a motorized grinder. The precut sample was mounted on a rotating vice in order to grind the surface.
4. The ends of each precut pair was trimmed using a rock-cutting saw so that final lengths were around 6.9 cm.
5. The circular ends of the precut pair were surface ground using the motorized grinder.
6. The precut pieces were saturated in water prior to sample assembly.

7. A piece of Teflon tubing (originally 3.75 cm diameter) was cut slightly smaller than the length of the precut pair and heat shrunk down to 2.5 cm diameter. This served as the inner jacket
8. One end of the precut was inserted into the tubing.
9. A known weight (5 gm) of the gouge mineral was weighed and poured on to the surface of the inserted precut. Uniform packing was closely monitored by ensuring even thickness (4 mm) along the precut surface.
10. The other precut piece was inserted and pushed so that the mating between the gouge and the precut pieces was even.
11. A second piece of Teflon tubing was cut (about 8.5 cm long) and heat shrunk on to the sample and the Pyromet end-pieces.
12. Silicone tape was used on each end-piece to serve as a compliant seat for the wire-wrap seal.
13. Sample length was measured and recorded.
14. The pore pressure transducers, confining pressure transducer, load cell and the DCDT were calibrated before the experiments following regular calibration procedure and standards.
15. The upper piston was put in contact with the sample.
16. A small confining pressure (typically 50 psi or 0.3 MPa) was applied in the beginning of the loading process to ensure jacket integrity.
17. Once a small confining pressure was applied, pore fluid was pumped through the sample using an Eldex pump (Fig. 4.1) for about 5 minutes to drive air out of the sample and saturate the gouge.
18. A small pore pressure is applied after the downstream pore pressure end was valved off at the back-pressure regulator (Fig. 4.1).
19. Confining pressure and pore pressure were both increased to 1000 psi (6.9 MPa).
20. Confining pressure was further increased to 3000 psi (20.7 MPa). The axial load at this stage should equal the confining pressure times the sample cross-section area.

21. Sample was allowed to sit under load during hold stages. Pore volume changes were monitored by the stroke on the syringe pump (from the graduated scale on the syringe pump).
22. Permeability measurements were conducted at various points during the hold cycle by the steady state method. The Eldex pump was used to pump fluid at a constant flow rate at the upstream end of the sample. The back-pressure regulator (dome pressure set at 1000 psi or 6.9 MPa) ensured the downstream pore pressure to be at 1000 psi (6.9 MPa). The difference between the upstream and downstream pressure was noted. The flow-rate was obtained from collecting fluid through the back-pressure regulator over a period of 2 minutes. The amount of fluid was weighed using a O'Haus digital weighing balance. A density of 1 gm/cc was used for the distilled water to arrive at flow-rate. Permeability was calculated using the pressure difference, flow-rate and the viscosity of the pore fluid (water).
23. For each slide cycle the ram was advanced causing the sample to slide along the gouge.
24. Data was recorded over four channels (for axial load, axial displacement, confining pressure and pore pressure) at one-second interval. A Hewlett-Packard GPIB was used to acquire the data using a QBASIC acquisition software written by T. E. Scott.
25. The data acquired during each slide cycle was downloaded to a spreadsheet program for further analysis.
26. During unloading the axial load was removed first followed by the reduction of confining pressure to 1000 psi (6.9 MPa). The pore pressure and confining pressure was completely removed simultaneously.

Chapter 5

Shear and time-dependent particle size distribution evolution in slide-hold experiments

Abstract

Slide-hold tests using triaxially-loaded precut forcing blocks and artificial gouge were conducted to examine contrasts in gouge particle size dynamics during frictional sliding and healing stages. A series of room-dry sliding experiments were conducted to various shear strains using dry gypsum gouge in between precut steel forcing members. A separate series of experiments saturated with distilled water were conducted at a pore pressure of 6.9 MPa (effective pressure of 13.8 MPa identical to the dry tests). The latter experiments were taken to a constant shear strain but were held under shear loading for various lengths of time (0.01-10 hours) after slip. Particle size distribution (PSD) of gouge was measured using a laser particle size analyzer with a measurement range of 0.4-2000 microns. Stress-strain behavior for both dry and wet tests revealed multiple stress drops or stick-slip events and were similar suggesting no marked strengthening or weakening effect due to presence of water over the time scale of sliding. Gouge PSD's were fit to a log-normal distribution function and then analyzed in terms of the moments of mass-size distributions. The best log-normal fits were obtained in the coarser fraction of the gouge (larger than peak size). PSD means decreased with shear

while higher moments such as spread and skewness increased with shear. Particle number-size relationships computed from the mass-size distributions revealed a fractal nature of the gouge with excellent fits obtained for fine and intermediate fractions (smaller than peak size). A fractal dimension (*D*) around 2.6 consistent with previous work on both natural and experimental fault gouge was obtained. There appears to be a correlation between *D* and the amount of shear strain and an inverse relationship between D and the mean particle size. The time-dependent evolution of PSD is reported for the first time in the faulting literature. The evolution during hold phases contrasts with that during sliding. Shear displacement results in overall fining of the PSD while during hold time the PSD shows distinct evidence of coarsening. A recrystallization flow mechanism such as Ostwald ripening may drive this time-dependent coarsening. The coarsening and consequent decrease in porosity, crack sealing and lithification may drive strength recovery of fault zones. Previous workers have observed a correlation between critical-slip distance in the rate- and state-dependent friction model and mean gouge particle size or with *D*, but there have been no systematic investigations of PSD dynamics during time-dependent healing. Inasmuch as this influences critical slip distances, it should be incorporated into earthquake models.

Introduction

Localized deformation in the brittle regime is almost always associated with creation of significant cataclastic material or fault gouge. Variations in properties of the granular aggregate comprising the fault gouge has been shown to exert profound influence on the mechanics of faulting in laboratory experiments (Karner et al., 2001; Olsen et al., 1998; Blanpied et al., 1991; Ruina, 1983; Dieterich, 1979). Fault zone texture comprised in large part by particle size distribution (PSD) dictates the frictional strength, nature of slip instability, permeability characteristics of a fault zone and fault zone diagenesis. The role of particle size in governing fault zone friction has been the subject of multiple laboratory investigations (Biegel et al., 1989; Marone and Scholz, 1989, Marone et al., 1990; Chester and Logan, 1987; Byerlee et al., 1978). Since the work of Brace and Byerlee (1966), one favored mechanism for earthquake has been associated with stick-slip frictional instability reported from laboratory experiments. Stick-slip like instability was shown by Dieterich (1979) to be a result of decrease of coefficient of dynamic friction concomitant with increase in sliding velocity. He introduced the concept of characteristic displacement as the sliding distance necessary to achieve a new value of dynamic friction through a change in the population of asperity or contacts. The rate- and state-dependent friction formulation developed from these laboratory experiments relates PSD parameters such as the mean particle size or the maximum particle size (also the upper fractal limit) to critical-displacement (Sammis and Steacy, 1994; Marone and Kilgore, 1993; Biegel et al., 1989; Morrow and Byerlee 1986; Dieterich, 1992). As a consequence PSD parameters directly influence size of pre-monitory slip nucleus (Sammis and Steacy, 1994). Hydrologic properties of the fault zone may depend on PSD as permeability has been shown to depend not only on mean particle size but also its spread and skewness (Panda and Lake, 1994) all of which are affected by the magnitude of shear strain.

PSD analyses of both natural and laboratory fault gouge suggest a remarkable similarity in gouge characteristics in laboratory and nature. Fractal dimension (*D*) for both natural and laboratory fault gouge has been observed to be close to 2.6 (An and Sammis, 1989; Marone and Scholz, 1989; Sammis et al., 1986; Olgaard and Brace, 1984; Engelder, 1974). Observations both in nature and laboratory indicate a relationship between amounts of shear strain and *D* (An and Sammis, 1989; Marone and Scholz, 1989). Earlier works suggest that gouge particles obey a log-normal distribution and that the mean is inversely proportional to shear displacement (Anderson, 1980). This led to the hypothesis that fragmentation during shearing is independent of particle size (Sammis et al., 1986; also Epstein, 1947) which was later rejected (Sammis et al., 1987) in favor of a nearest neighbor size dependent fracturing probability that led to a power-law distribution with a fractal dimension of 2.6. Natural fault zones show evidence for nearest-neighbor dependent breakage with large clasts floating in a fine-grained matrix (Engelder, 1974; Hadizadeh, 1994). Incorporation of a grinding limit below which fracture probability for particles is drastically reduced does not change the fractal nature of PSD (An and Sammis, 1994).

While substantial data for PSD evolution as a function of shear exists for both natural and laboratory fault zones its evolution during inter-seismic hold periods is lacking. The purpose of this chapter is to illustrate that PSD evolution during shear is distinct from the time-dependent evolution during hold (inter-seismic) periods. It will be shown that shear displacement results in PSD fining in a manner consistent with other work (An and Sammis, 1994; Marone and Scholz, 1989; Anderson et al., 1980). In contrast, gouge PSD coarsens during the hold periods. The degree of coarsening is a function of the duration of post-slip hold period. Time-dependent evolution of PSD has not previously been reported in the faulting literature. It is argued that fault strength (and its recovery), frictional properties, the nature of slip instability, and hydraulic conductivity along fault zones are all influenced by PSD evolution during inter-seismic periods. Understanding of PSD properties during time evolution of fault gouge is therefore essential.

Representation of Particle Size Distribution

PSD data representation is primarily an exercise where discrete parameter pairings such as particle mass - size, volume - size, number - size, or number - mass are evaluated for statistical significance. Geologists, especially sedimentary petrologists, measure mass of particles passing through certain sieves and the PSD is represented either as incremental or cumulative mass-size plots. Faulting or fragmentation is often thought of as a self-similar process and thereby PSD's are cast in number-size terms. Several probability distribution functions (*pdf*) and empirical relationships that have been applied to fragmentation processes have been reviewed in Appendix 5A.

It must however be borne in mind that multiple (empirical) relationships may satisfy the same data set or more commonly parts of a data set to a good degree. It is customary to use these and other similar functions in PSD analyses. However, satisfactory representation of the data by any function by itself does not throw any light on the physical mechanisms or chemical processes that are involved in PSD evolution because of the empirical nature of some of these functions. The degree and extent of fit of each of the probability distribution functions for the data presented here will be noted in a following section.

Experimental Setup

Triaxial compression slide-hold experiments were conducted using steel forcing members with a layer of gypsum sand (White Sands National Monument, New Mexico, USA). Experiments were performed in a SBEL pressure vessel (rated to 69 MPa) using a commercially available MTS loading frame (model 318). Total sample length including a 4 mm gouge layer ranges between 6.9 – 7.1 cm. A schematic of the loading column, pressure vessel and sample geometry is given in Figure 5.1. Steel forcing members are made by a precut at 30° to the long axis of a cylinder surface ground to a planar finish at the top and bottom. A pore pressure port was bored through the center in the steel cylinder. In order to ensure that slip is not restricted to the interface between gypsum and the steel, the precut surface was prepared by rubbing on a 60 μm polishing plastic sheet (manufacturer 3M) with constant motion along

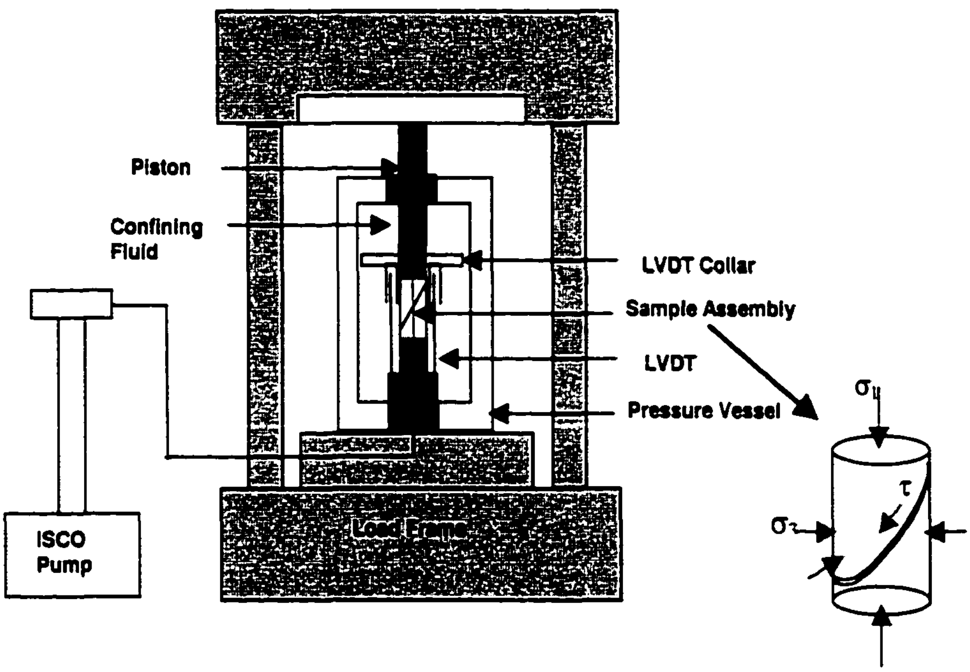

Fig. 5.1: Schematic diagram showing the loading frame, pressure vessel, pore pressure (ISCO) pump and the pre-cut sample geometry. Also shown (right) is a schematic diagram for the sample with a steel forcing members pre-cut at 30° to the maximum loading axis. A 4 mm thick gypsum gouge is sandwiched between the forcing members. The directions of the maximum (σ_1) and minimum (σ_3) principal stress axes and shear stress (τ) are indicated.

the strike direction (perpendicular to slip direction). Typically this was achieved by making grooves on the precut surface by other investigators. However, it causes a small portion of the fine-grained gouge fraction to be stuck inside the grooves early in the slip process. This fraction then takes no further part in the slip process. Samples are jacketed using two Teflon roll sleeves. The inner sleeve just extends over the precut while the outer is used to wire wrap the sample assembly and affix it to the loading column. A fixed amount (5 gm) of gypsum gouge is used. All experiments were conducted at an effective (confining minus pore) pressure of 13.8 MPa. A constant strain-rate of 5×10^{-5} s^{-1} was maintained in all tests.

Two separate series of experiments were run. In the first series, room-dry samples were taken to various shear strains (γ = 0, 0.8, 1.4, 1.7, 2.2, 2.6 and 2.8). In the second series of experiments, the samples were all taken to a constant shear strain (γ = 1), but subsequent to slip they were held under constant confining and pore pressure (20.7 and 6.9 MPa respectively) for a range of hold times (0.01, 0.1, 1, 2, 5 and 10 hours). Axial displacements were measured by two LVDT's (linear variable displacement transducer) mounted inside the pressure vessel across the length of the sample assembly. The measured axial displacements were converted into shear displacements (δs) along the precut surface using the sample geometry. Shear strain is computed in a manner similar to Marone and Scholz (1989) as $\delta s/s$ where s is the initial gouge thickness (4 mm in all cases). Pore pressure in the wet tests was applied and maintained using an ISCO (model 100DX) pump. Initial porosity within the gouge was determined by a water displacement method to be 40%. Pore-volume change during shear and also during creep was measured using the ISCO pump piston displacement. The gouge was saturated with distilled water inside the pressure vessel under a small confining pressure (to maintain jacket integrity and to aid in bleeding the air off) by flowing fluid through the forcing member-gouge assembly. Pore pressure equilibration within the gouge during test was ensured by communication between the upstream and downstream pore fluid ports outside the pressure vessel.

The run products were analyzed using a laser particle size analyzer (LPSA) manufactured by Coulter Electronics Corp. (model # LS200). Data is measured over forty-nine channels spanning a range of 0.4-2000 μm (11.25 through -0.75 on the phi scale at intervals of 0.25 phi). LPSA data has been previously used in Agrawal (1991) for PSD analyses of sediments. Advantages of using this technique are its speed, small sample size requirement and large analytical range. LPSA data is generally reported as weight per-cent for forty-nine size fractions. Data reported as weight-size distributions were computed into number-size distributions assuming a spherical shape and constant density. Present technology with the possible exception of the electro-resistive or Coulter-Counter technique (Milligan and Kranck, 1991) precludes direct counting of numbers over the entire size range reported here.

Mechanical Test Results

Shear stress-strain results for both dry and wet tests were collected during the study. In addition for wet experiments pore volume changes were monitored during shearing as well as during the post-slip hold periods. Representative shear stress-strain results are shown in Figure 5.2. Data for a typical dry experiment shows typical stick-slip type behavior that has been commonly reported for similar experiments using different gouge mineralogy (Shimamoto and Logan, 1981). The shear stress rises gradually until a γ of about 1 and then undergoes several sharp stress drops. The magnitude of stress drop increases as γ increases. Stress drops are repeated after progressively larger increments of γ. The dry experiments are also characterized by numerous small-scale stick-slip like oscillations in between large drops in shear stress. Stress-strain behavior typical of wet experiments were largely similar to that described above for dry tests. Stress-strain behavior was unstable or stick-slip like with larger but less frequent stress drops with an increase in γ. Maximum strength reached for wet experiments are comparable to dry tests. It appears that addition of water as pore fluid results in no appreciable weakening/strengthening over the time scales of these experiments. Figure 5.2 also shows pore volume change (obtained from the ISCO pump stroke) for the same wet experiment. The overall trend of the pore volume change is one of compaction due to a continuous decrease in porosity of the gouge. However, some of the large stress drop events are associated

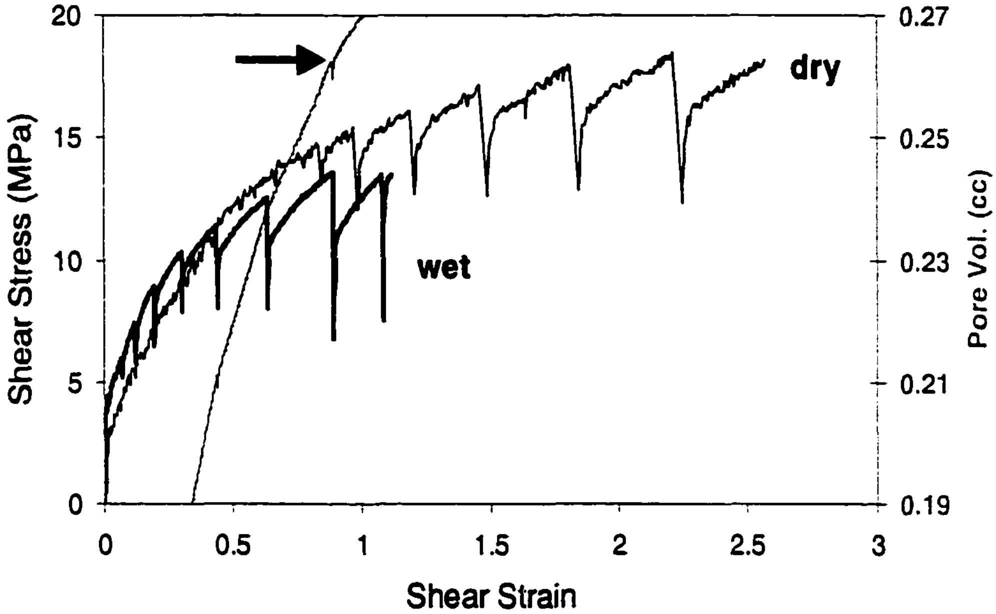

Fig. 5.2: Shear stress plotted against shear strain (see text for definition) for representative dry and wet tests conducted on gypsum gouge. The shear stress values and the overall nature of deformation (multiple stick-slip like events) are similar for both wet and dry experiments. Also plotted is the pore volume loss (compaction) during the wet test (gray). Note the excursion of the pore volume loss curve (arrow) at a stress-drop suggesting dilatant behavior of the gouge during drop in stress.

with dilatancy as characterized by a small but sharp decrease in pore volume change (note the excursion of the pore volume loss curve at the instant of a large stress drop in the wet experiment). This indicates that stress drops are associated with dilatant behavior of the gouge that can only be detected (by the ISCO pump) for the relatively large magnitude events.

Shear Dependent Particle Size Distribution Evolution

PSD evolution and grinding limit of gypsum

PSD data exhibit gradual shift of the distribution towards the fine end of the size spectrum with incremental shear strain (Fig. 5.3a and 5.3b). Several qualitative changes in PSD characteristics stand out with an increase in shear strain: (1) decrease in maximum or peak size frequency, (2) shift in the center of the distribution towards finer sizes, (3) increase in the width of the distribution (tails) and, (4) significant incremental accumulation of fine size aggregates (<10 μm as observed in Fig. 5.3b). Progressive changes in the PSD parameters (mean, spread, skewness) will be discussed later. PSD data for the finest end of the size spectrum (0-10 μm, Fig. 5.3b) in addition to an increased proportion of fine sized particles also exhibits development of a subsidiary peak at about 1.6-1.7 μm. This subsidiary peak grows in magnitude but the center remains fixed on the size axis. This suggests that there is accumulation of fine sized particles with progressive wear and grinding but the probability of fracturing is reduced significantly on reaching 1.6 -1.7 μm. This appears to be the grinding limit for crystalline gypsum.

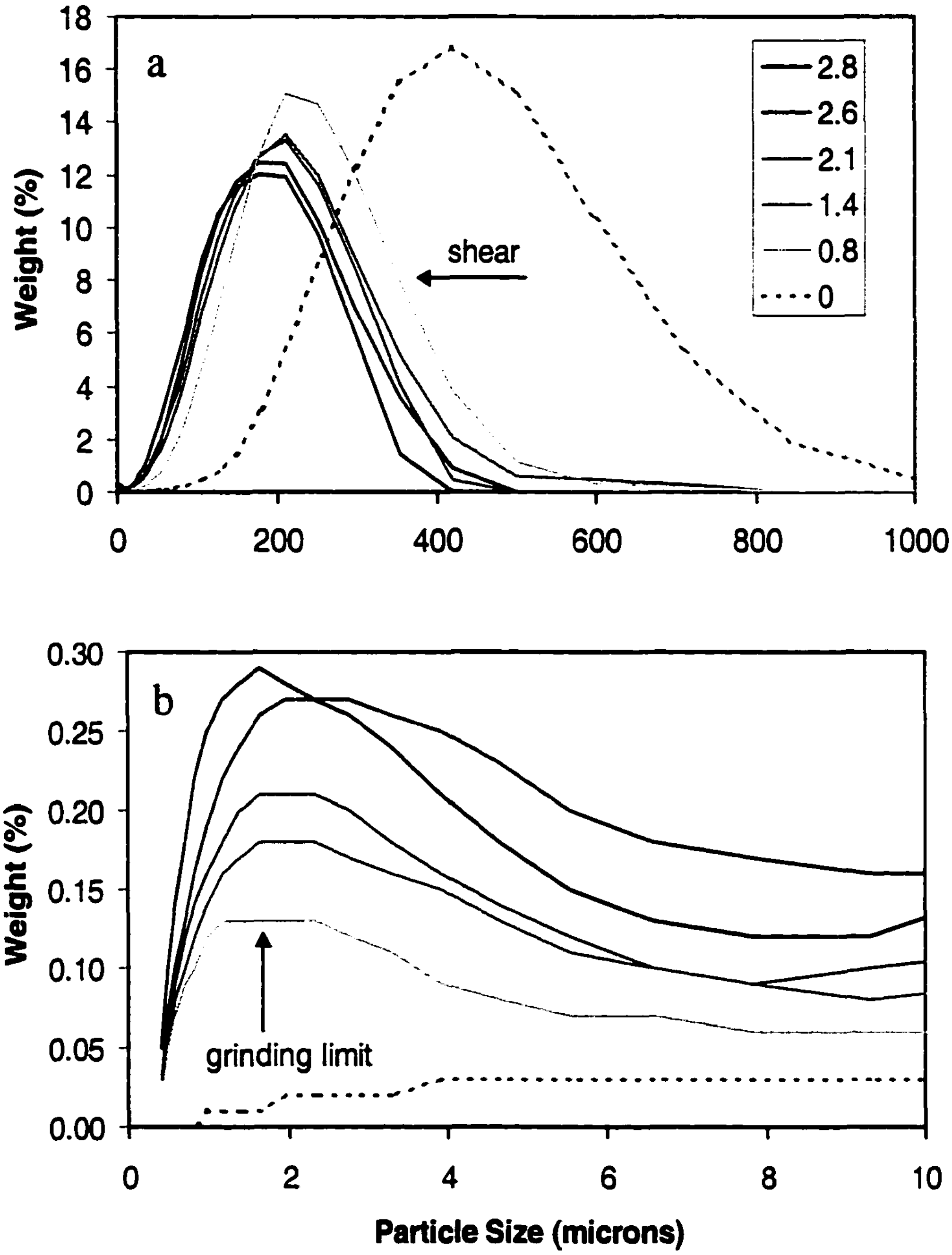

Fig. 5.3a: Particle size distribution (PSD) for dry experiments run to various shear strains (legend). The initial distribution is plotted as a broken line. Note the progressive shift of the PSD towards finer sizes with incremental shear. The apparent difference in the area under each curve arises due to plotting of observations separated by 0.25 phi on a linear scale. (b) Detailed view of the above (Fig. 5.3a) showing the accumulation of fine sizes with progressive shear. The growth of a peak with incremental shear suggests grinding limit of gypsum to be about 1.6-1.7 µm.

A grinding limit for gypsum was not found reported in the literature. The value of 1.6 -1.7 μm obtained here for gypsum is similar to those obtained for calcite (4.4 μm), quartz (1.7 μm), albite (1 μm) and amorphous silica (0.5 μm,) (Prasher, 1987; Kendall, 1978). The grinding limit is characteristic of a particular mineral and the crushing or grinding mechanism. For example, attrition mills are reported to give rise to finer sizes relative to ball mills because of the greater shear forces involved. Various arguments have been invoked for the existence of grinding limits for materials. Prasher (1987) suggests that grinding stops at a certain size characteristic for a particular material due to a transition from brittle to plastic behavior at such sizes. Another possible argument is related to a decrease in number and size of flaws as particle size becomes small. A steady-state may also be reached where rate of granulation equals rate of aggregation (Opoczky and Farnady, 1984; Prasher, 1987).

Two processes aggregation and agglomeration, both produce apparently similar signatures of coarsening. Aggregation has been related to cohesion or Van der Waals forces resulting in a reversible adherence of small particles while agglomeration is related to a chemical change causing an irreversible adherence of particles. Aggregation is said to be common in softer minerals such as gypsum while agglomeration is a feature of "hard" (to grind) minerals such as quartz (Prasher, 1987). Chemical changes can be ruled out in the dry experiments presented here thus ruling out agglomeration as an operative process. The PSD measurements reported here were conducted in water after sonicating the sample suspension to aid in dispersal and as such aggregation of particles can also be ruled out.

Log-normal distribution fits

No single distribution has generally been observed to fit PSD data. On the other hand, multiple forms have been found to fit substantial data segments. In order to characterize PSD parameters such as mean, spread and skewness, the mass-size distribution data was fit with forms 2 through 6 discussed in Appendix 5A. The Rosin-Rammler function only gave good fits for an intermediate data range. Only the very fine data segment (< 10 μm) could be fit with fractal mass-size distribution. The log-normal distribution gave generally good fits overall though it consistently over-predicted data below 50 μm. The number-size fractal distribution could fit the finest size fraction data (generally < 50 μm) in agreement with data presented by An and Sammis, (1994) on natural faults. Other distribution functions such as that of Harris or Gaudin-Meloy yielded poor representation of the data. The multiple shape parameters these distribution functions employ do not have obvious physical significance. The Weibull exponential distribution generally fit the data well except for under-predicting data less than approximately 50 μm.

In this study, PSD data was analyzed using the log-normal distribution for the coarser fraction and the fractal (number-size) relation for the finer (sub log-normal) grain size fraction in a manner similar to An and Sammis (1994). For ease of regression analysis mass-size data was fitted using a Gaussian normal distribution available in non-linear curve-fitting software that uses the Levenberg-Marquardt algorithm. The mean and standard deviation obtained from regression was converted to log-normal counterparts.

PSD mass-size data are shown plotted in semi-logarithmic space in Figure 5.4. Observed data is shown together with the fit to a log-normal distribution. Entire size range data for an experiment is fit well by the log-normal function ($R^2 = 0.96$ or higher) and has not been shown. However, this results in an overestimation of the size fraction below approximately 80 μm and also over-predicts the peak frequency. As a result only the relatively coarse fraction of the data set including the peak was included in the fit. In each case, the maximum number of data points was fitted while maintaining a high regression coefficient ($R^2 = 0.99$ or higher or chi-square value lower than critical chi-square for the required degrees of freedom at the 99% confidence level). For all shear strains a log-normal data fit is excellent for the coarse fraction of the gouge. Interestingly, an increase in shear strain results in a decrease in the lower bound of the data that fit a log-normal distribution satisfactorily (for γ of 2.8 log-normal fit is excellent up to 52 μm while for γ of 0.8, an excellent fit was achieved only up to 105 μm). PSD data (Fig. 5.3b) shows existence of a subsidiary peak at 1.6-1.7 μm due to approach towards a grinding limit for gypsum as discussed above. This would alter fit characteristics when considering the entire data range.

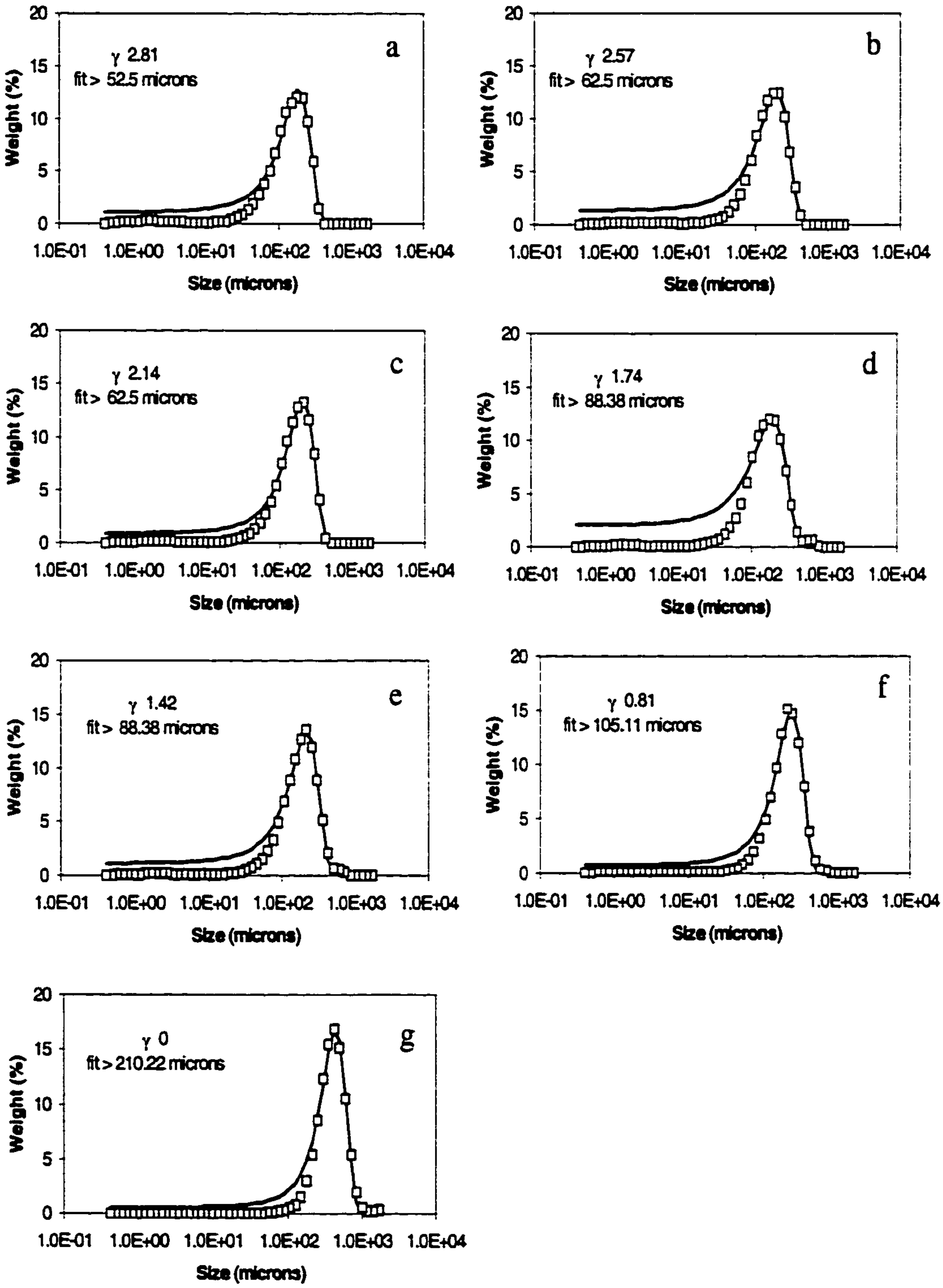

Fig. 5.4: PSD plots as weight (%) against size in microns for experiments conducted at various shear strains (γ 0-2.81). Symbols are observed values determined from LPSA measurements while curves represent log-normal fits to coarser fraction of the data.

Fractal distribution fits

PSD mass-size data was recomputed into number-size to investigate fractal number-size characteristics. In order to calculate number a constant density (2.35 gm/cm^3) for the gypsum and a spherical shape was assumed. Numbers were calculated for a mass of 100 gm. Number-size plots on log-log axes for the previous data set (Fig. 5.4) are presented in Figure 5.5. PSD number-size data typically exhibits a steady decrease in number to about 10 μm, then a slower decrease to about 100 μm and then drops rapidly. As mentioned before, a subsidiary peak developed in the mass-size distribution as the gouge approached its grinding limit (Fig. 5.3b). The decrease in mass at sizes larger than the grinding limit is manifest in the number-size plot by smaller number of particles in the segment 10 -100 μm.

The slope of a number-size plot on a log-log plot is the fractal dimension (*D*). Most values of *D* lie (especially for fragmentation processes) in the range $2 < D < 3$. The upper and lower bound of the validity of a power-law relation are the upper and lower fractal limits. The lower fractal bound identified by distinct changes in slope in number-size plots, that is associated with instrument detection limit is absent in the current analyses. The instrument detection limit is taken to be the lower fractal limit (0.4-0.5 μm). The upper fractal limit is more equivocal, though from the shape of the number-size curve (Fig. 5.5) it appears to be less than 100 μm as there is a rapid drop in the PSD beyond 100 μm.

The fractal dimension, *D*, was determined from the slope of the number-

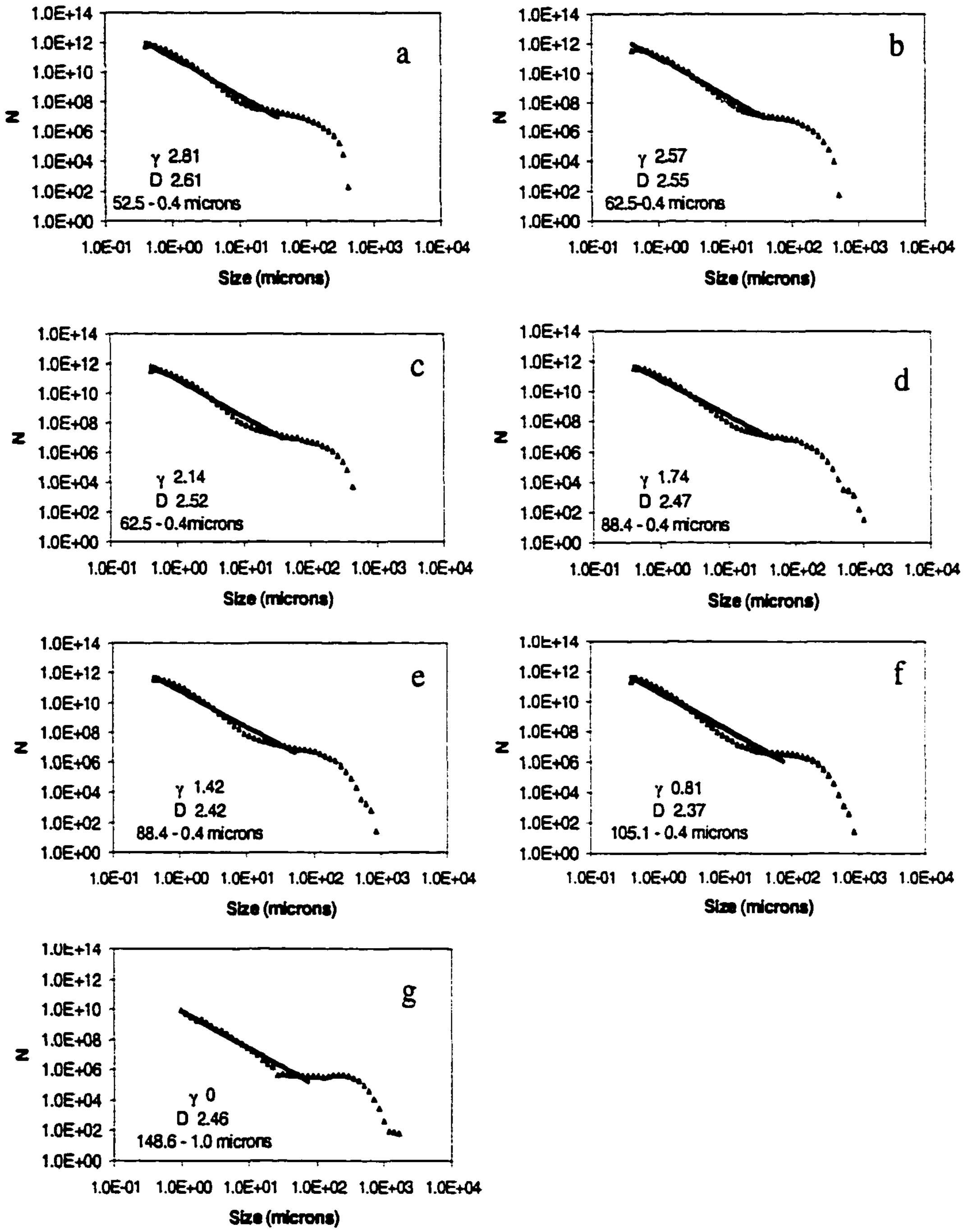

Fig. 5.5: PSD plots as log of numbers (computed from weight) against log size in microns for experiments conducted at various shear strains (γ 0-2.81). Symbols are observed values determined from LPSA measurements while lines represent power-law (fractal) fits to finer fraction of the data. The fractal dimension D and the fractal limits are noted against each figure.

size plot in logarithmic space (Fig. 5.5) with a lower fractal limit of 0.4 μm (also the detection limit) and an upper fractal limit that ranges from 53 μm to 149 μm. The upper fractal limit for each sample is taken to be the lower bound of the log-normal fit for the PSD (Fig. 5.4). The upper fractal limit appears to have a correlation with the shear strain in the gouge being lower for higher shear strains (*e.g* 53 μm for γ of 2.8 and 105 μm for γ of 0.8). *D* values determined in this manner range between 2.46 and 2.61 and exhibits an increase in the fractal dimension with an increase in shear strain. If instead of varying the upper fractal limit it is held fixed at 53 μm (the lowest determined for any of the analyzed samples), *D* is observed to be in the range 2.55 – 2.75 with no apparent correlation with the amount of shear.

Correlation between shear and PSD parameters

The correlation between shear strain and various PSD parameters such as mean, spread (coefficient of variation), skewness (asymmetry of data), kurtosis (peakedness of data) and fractal dimension (*D*) are important in depicting the evolution of PSD with an increase in amount of slip. In the following section, the functional dependencies of such parameters on shear strain is investigated. Mean, spread, skewness and kurtosis were determined from log-normal fits to the mass-size PSD. As the standard deviation and the mean are both positive for the log-normal distribution their ratio is a measure of the spread (also known as the coefficient of variation). It is a dimensionless quantity as are skewness and kurtosis.

Means determined for PSD evolve inversely with increasing shear strain (Fig. 5.6). Wear by attrition during incremental shear results in a fining trend manifest as a non-linear decrease in PSD mean. Various forms of non-linear fits such as logarithmic, exponential or power-law functions of shear strain may satisfy the data. A power-law function for the dependency of mean on shear strain has a strong correlation ($R^2 = 0.985$) and has been used previously in the literature to represent crushing and grinding processes. The spread increases with an increase in shear strain (Fig. 5.6, secondary vertical axis). Data for the spread was also fit ($R^2 = 0.95$) with a power-law function in a manner similar to the mean. Skewness (not shown), a measure of the asymmetry of the PSD data, behaves in a manner similar to the spread and exhibits a consistent increase with an increase in shear strain.

The evolution of fractal dimension *D* with an increase in shear strain has been investigated previously (Marone and Scholz, 1989). These authors observed a non-linear evolution of *D* in quartz gouge experiments with an increase in shear strain. In their experiments *D* seemed to saturate at about 2.6 after a γ of 1.3. The *D* value obtained in the dry gypsum experiments conducted for this study has been plotted against shear strain in Figure 5.7a. *D* increases linearly with shear strain and does not saturate. Investigations of natural fault gouge showed an inverse dependence of the *D* value on average particle size or the maximum particle size (An and Sammis, 1994; Blenkinsop, 1991). Laboratory data presented here (Fig. 5.7b) suggest similar behavior where

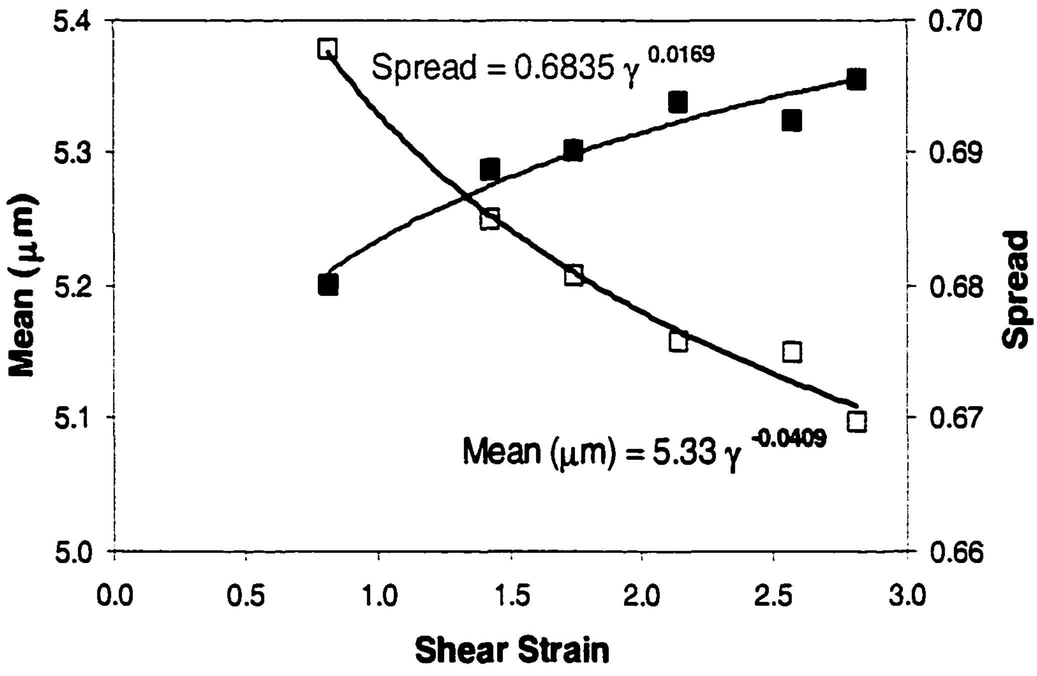

Fig. 5.6: Log-normal mean (open symbols) and spread (solid symbols) plotted against shear strain (γ) for dry experiments taken to various shear strains (γ 0.8-2.8). Mean decreases as a function of increasing γ while spread increases with γ. Power-law fits to the data is shown by dark (mean) and gray (spread) curves respectively.

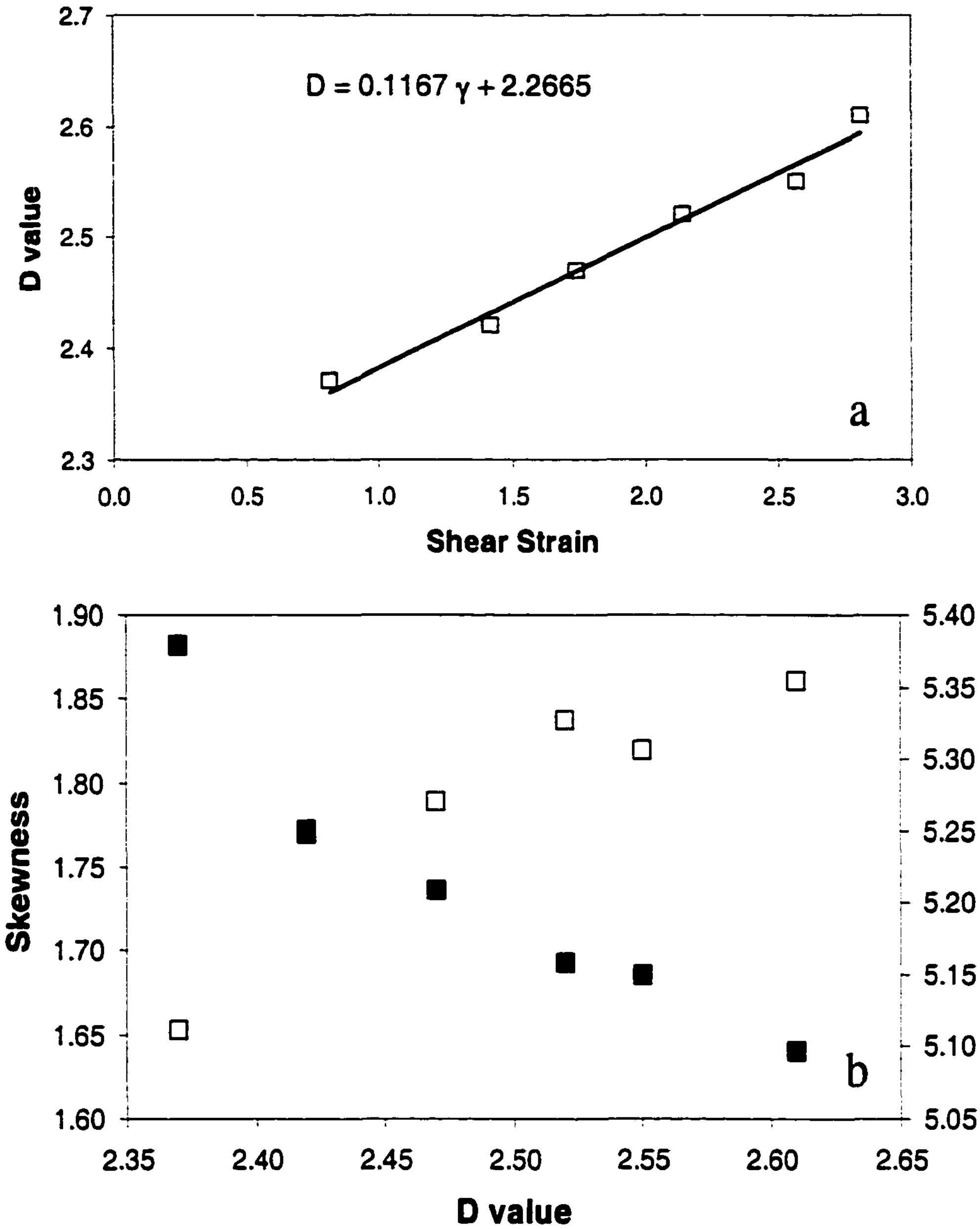

Fig. 5.7a: Fractal dimension D plotted against shear strain γ over a range 0.8-2.8. A linear fit appears to adequately represent the data. (b) Mean (solid symbols) and skewness (open symbols) determined from log-normal fits to PSD data plotted against fractal dimension (D value). D values are from Fig. 5.5. Fractal dimension, D appears to have an inverse relationship with mean. Curve-fits to data not shown as several fits to the data are statistically indistinguishable.

the mean size exhibits an inverse dependence on the fractal dimension. An increase in *D* is also associated with an increase in the skewness.

Time-dependent Particle Size Distribution Evolution

PSD data exhibits a coarsening trend as a function of increasing post-slip hold-time in sharp contrast to its evolution with increasing shear. This coarsening trend is apparent in wet experiments taken to the same shear strain (γ of 1.05) but held under triaxial conditions for post-slip hold times of 0.01, 0.1, 1, 2, 5, 10 hours (Fig. 5.8a). The change in PSD characteristics as a function of increase in hold time are evident as: (1) a progressive decrease in the size of the peak frequency with increase in hold time, (2) a shift of the distribution center towards the coarser size end, (3) an increase in data spread similar to what was observed in PSD evolution with shear, (4) a systematic development of a tail in the PSD at the coarser end, and (5) a decrease in the proportion of the finest sizes accumulated at the grinding limit (subsidiary peak centered at approximately 1.6 μm) for gypsum with time (Fig. 5.8b).

Particle size distribution fits

In a manner similar to that discussed for PSD evolution due to shear (Fig. 5.4) the PSD data for the wet fault gouge experiments were fit using a log-normal function. Fitting the entire data set resulted in over prediction of the peak and slight under prediction of both the coarse and fine tails of the PSD, though

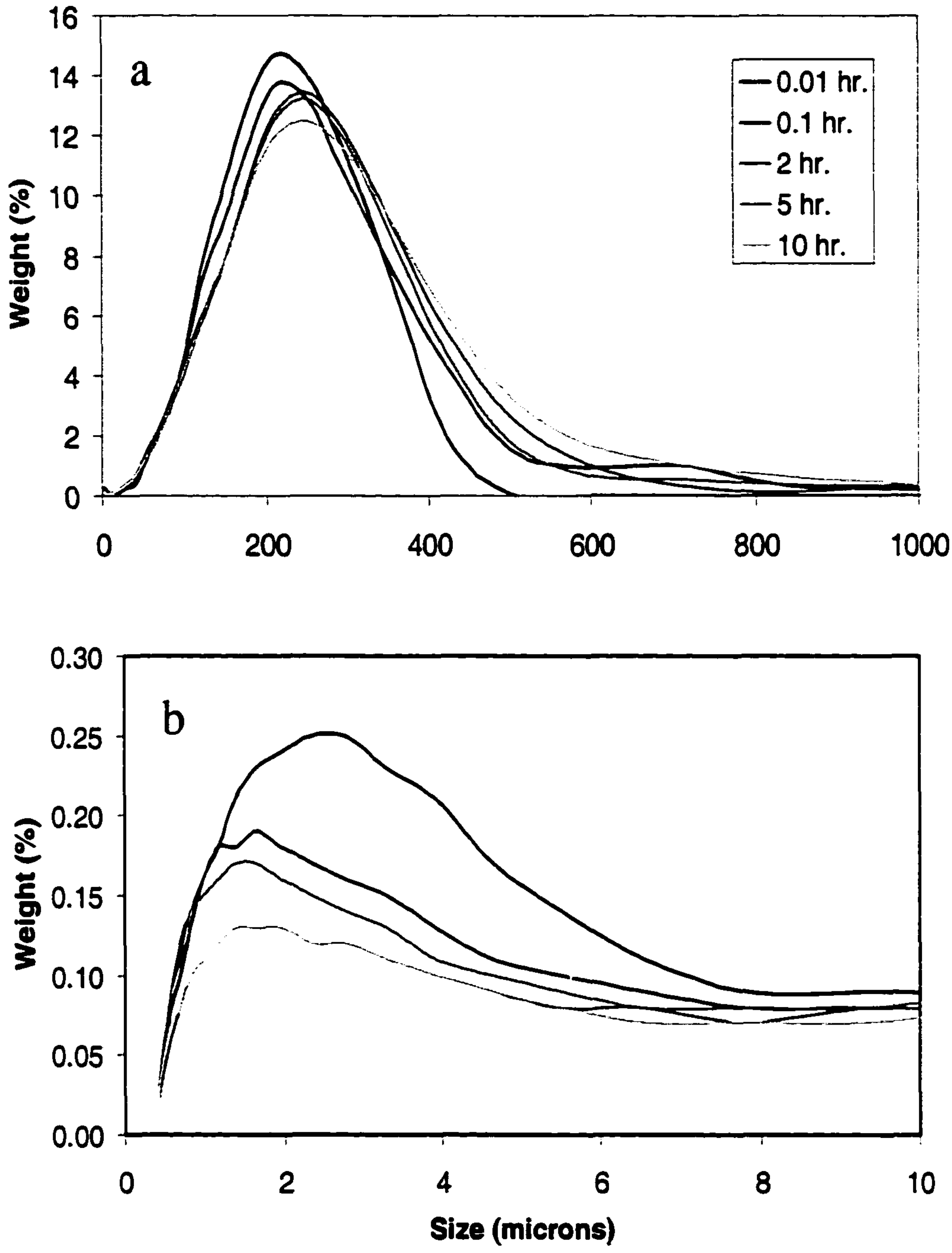

Fig. 5.8: Particle size distribution (PSD) for wet experiments run to a constant shear strain (γ 1.05) and then held for various lengths of time (0.01-10 hr., legend). Note the progressive shift of the PSD towards coarser end with increase in post-slip hold time. (b) Details of the above (Fig. 5.3a) showing the consumption of fine size particles of fine sizes with hold time.

it was statistically significant over the entire data set. In order to satisfy the coarse end of the data as well as the peak frequency only the size fraction greater than 74 μm was fit for all experiments in the series (R^2 = 0.99). The PSD data for experiments as well as the log-normal fits are presented in Figure 5.9. A constant lower bound of the log-normal fits (74 μm) was suggested by the data. This is consistent with observations from the dry experiments where the lower bound of log-normal fit appeared to be a function of the shear strain (Fig. 5.4). As before the finer fraction (< 74 μm) is under-predicted for the wet tests for all experiments.

PSD characteristics in terms of number-size data were calculated in the same manner as for the dry experiments and are shown in Figure 5.10. As suggested by the log-normal fits a constant upper fractal limit of 74 μm was used. The lower limit (0.4 μm) was maintained as the detection limit of the LPSA instrument. The slope of the number-size plot in log-log space (*D*) was determined and found to range between 2.6 – 2.4 with a systematic decrease corresponding to an increase in post-slip hold time. The nature of this change will be discussed in a later section.

Correlation between hold-time and PSD parameters

The evolution in PSD parameters such as mean, spread, skewness, and *D* as a function of incremental shear strain was investigated in Figure 5.6 and 5.7. To illustrate the marked change in characteristics of PSD evolution as a function of post-slip hold time these parameters have been analyzed and

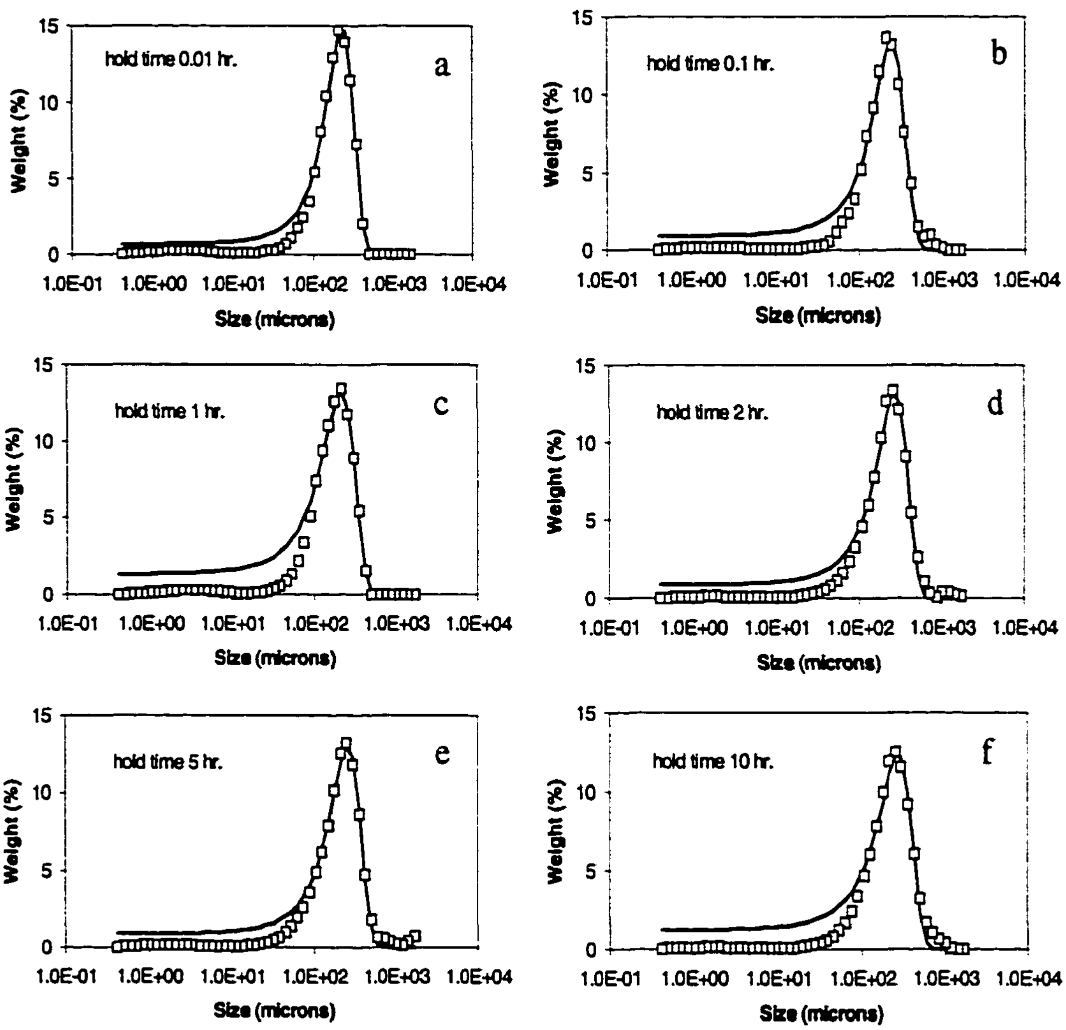

Fig. 5.9: PSD plots as weight (%) against size in microns for experiments conducted at a constant shear strain (γ 1.05) but held after slip under triaxial loading for various lengths of time (0.01 – 10 hr.). Symbols represent observed values determined from LPSA measurements while curves represent log-normal fits to coarser fraction (> 74.35 μm) of the data.

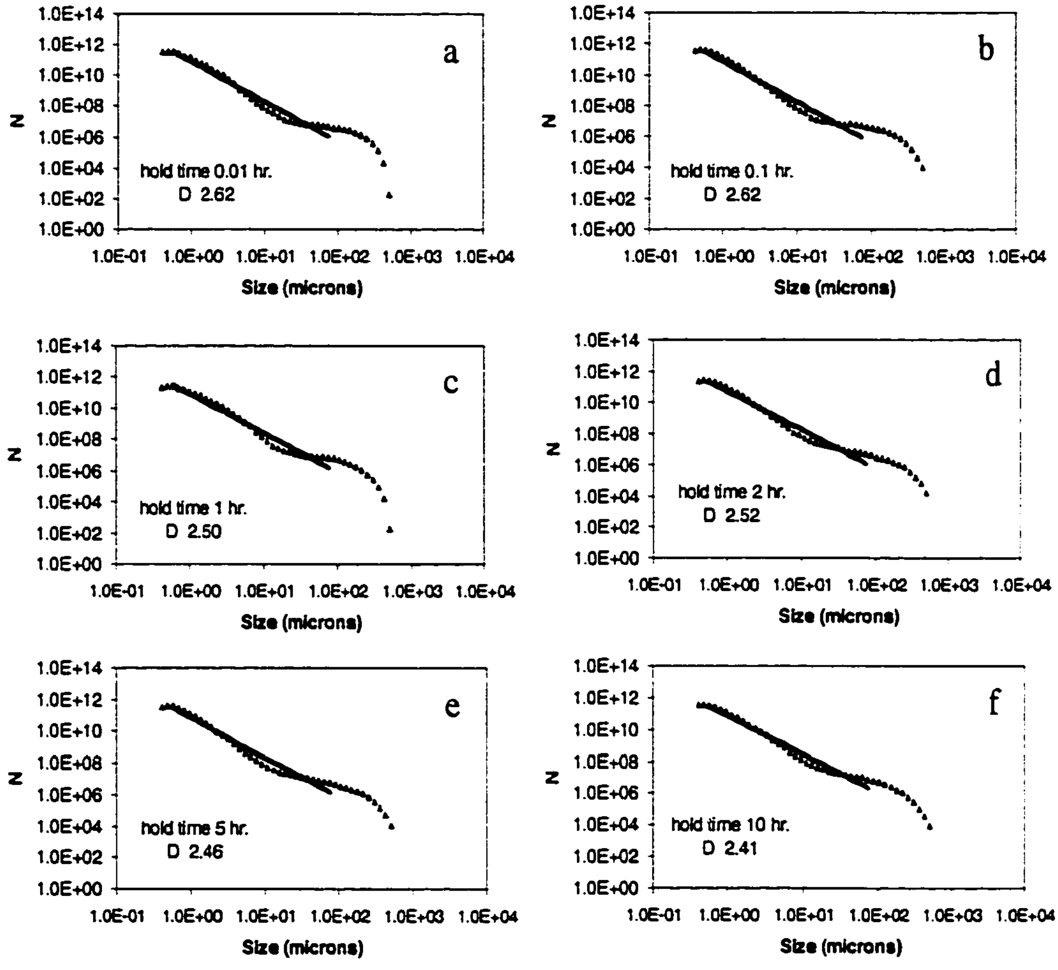

Fig. 5.10: PSD plots as numbers (computed from weight) against size in microns for experiments conducted at a constant shear strain (γ 1.05) but held after slip under triaxial loading for various lengths of time (0.01 – 10 hr.). Symbols are observed values determined from LPSA measurements while lines represent power-law (fractal) fits to data under the size 74.3 μm. The fractal dimension D is noted in each figure.

presented in Figure 5.11 and 5.12. Mean and spread for PSD data has been plotted as a function of the logarithm of hold time (Fig. 5.11) over three orders of magnitude (0.01 – 10 hr.). The mean appears to consistently increase non-linearly as a function of increasing hold time. Common non-linear forms such as a logarithmic fit or a power-law relation both fit the data and are statistically indistinguishable (R^2 = 0.93 for both). The logarithmic function (Fig. 5.11) may be reasonable as most time-dependent (creep) healing processes such as pressure solution have functional dependencies that are logarithmic with time (De Meer and Spiers, 1995; Dewers and Hajash, 1995; Spiers and Schutjens, 1990; see chapter 2). Data for the spread (coefficient of variation) appears to increase in a similar manner with an increase in hold-time (Fig. 5.11, secondary vertical axis, R^2 = 0.89). Skewness or the degree of asymmetry of the PSD also increases with an increase in hold time (not shown).

The fractal dimension (*D* values) was obtained from fits to the number-size data (Fig. 5.10) as described previously. *D* values have been plotted against logarithm of hold time to check for evolution in the fractal dimension with change in PSD (mean, spread and skewness). For an upper fractal limit of 74 μm *D* ranges between 2.68 (0.01 hr.) and 2.45 (10 hr.). *D* is observed to decrease with an increase in hold time (Fig. 5.12a). A logarithmic dependency between *D* and hold time adequately describes the data. Fractal dimensions as mentioned before depend on the upper and lower fractal bounds. If instead of 74 μm the upper fractal limit is chosen to be 31 μm the range of *D* values range

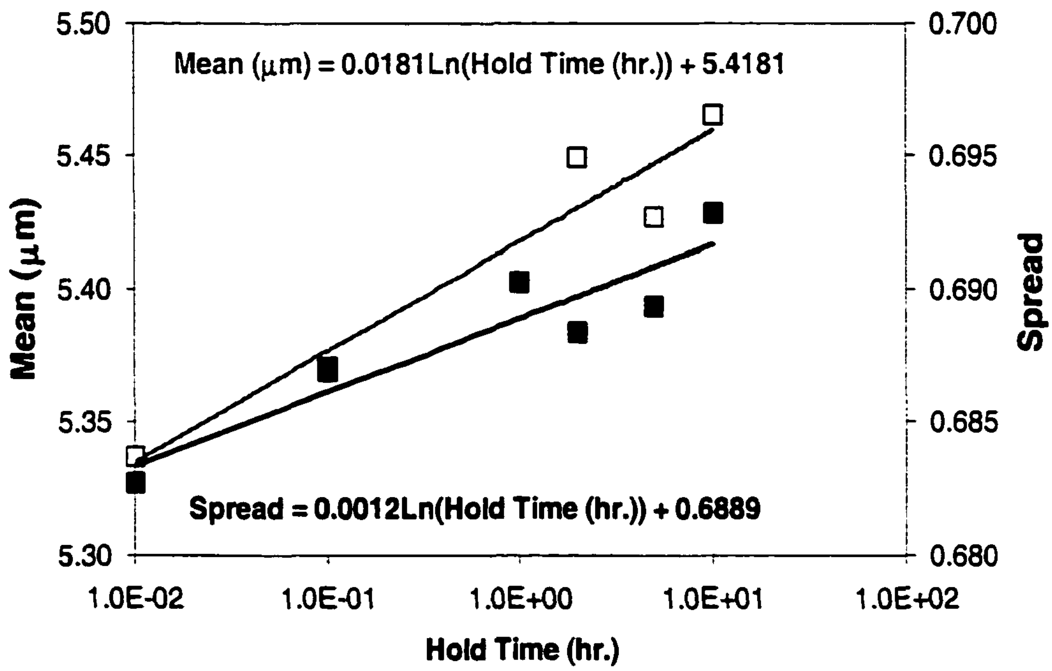

Fig. 5.11: Log-normal mean (open symbols) and spread (solid symbols) plotted against hold time for wet experiments taken to a constant shear strain (γ 1.05). Mean increases as a function of increasing hold time in contrast to Fig.5.6a. Spread also increases with hold time. Logarithmic fit to the data is shown by dark (mean) and gray (spread) curves respectively.

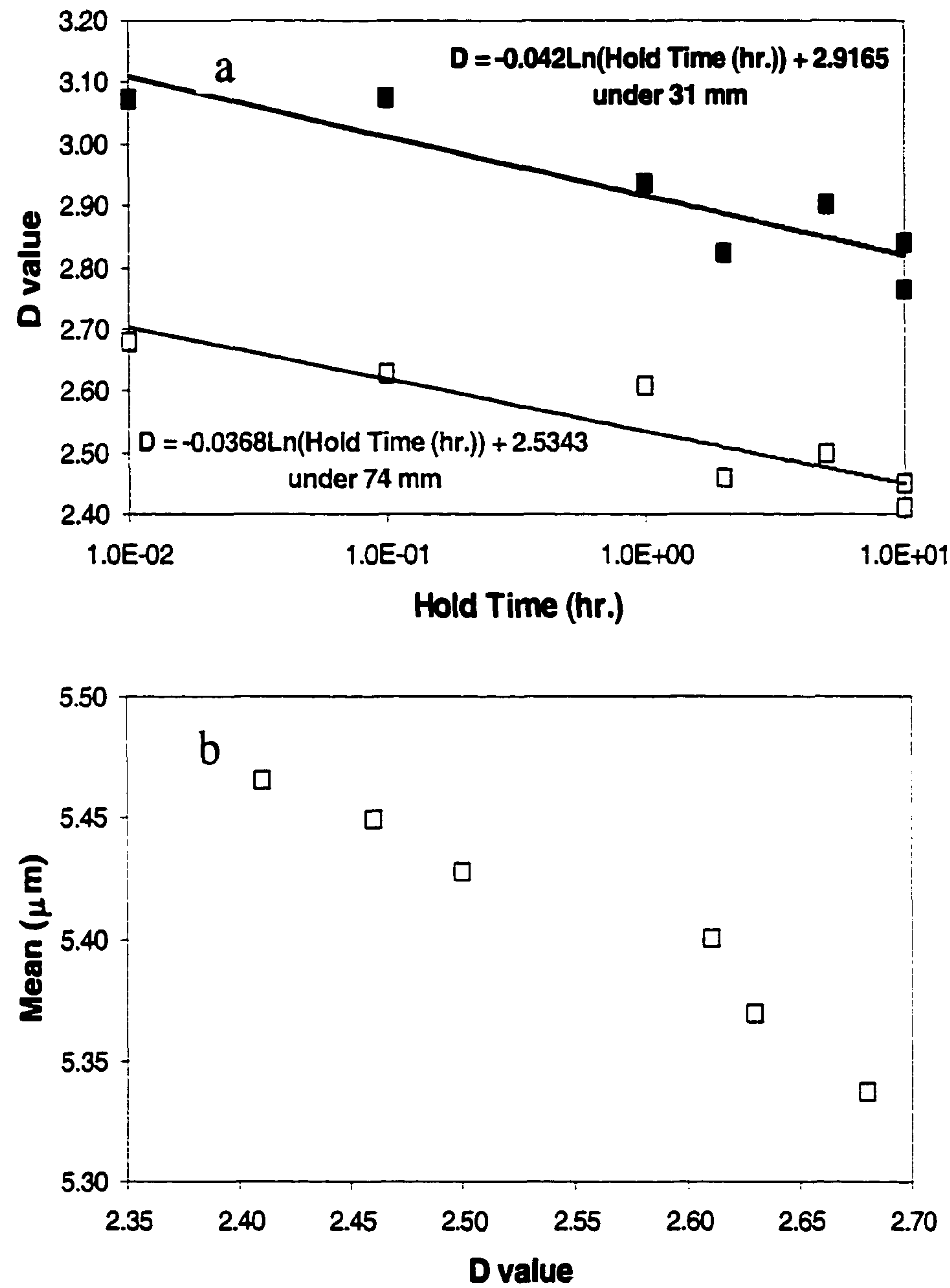

Fig. 5.12a: Fractal dimension D plotted against hold time for wet experiments. A logarithmic fit appears to adequately represent the data for the range of post-slip hold times (0.01-10 hr.). The relationship is consistent as suggested by similar forms for data under the size 74 or 31 μm. (b) Mean determined from log-normal fits to PSD data plotted against fractal dimension (D value). D values are from Fig. 5.10. Fractal dimension, D appears to have an inverse relationship with mean. Curve-fit to data not shown though a linear relationship is suggested.

between 3.07 and 2.76 but the evolution relationship with hold time remains unaltered. It was shown in Figure 5.7b that D varied inversely with the mean grain size for dry experiments that were taken to various shear strains. A similar trend is observable for the wet experiments where D increases with a decrease in mean particle size (Fig. 5.12b).

Coarsening Mechanisms

The coarsening effect observed in the PSD data as a function of increasing hold time may be due to the collective effect of pressure solution, formation of welded grain contacts, crack healing and Ostwald ripening. Ostwald ripening is a recrystallization mechanism where the high surface area - volume ratio of extremely small grains (generally < 2 – 4 µm) sets up a concentration gradient in fluid surrounding the small grains. Mass transfer along such steep concentration gradients result in consumption of the smaller grains and the consequent growth of the larger grains (Morse and Casey, 1988; Steefel and Van Capellan, 1990). Kinetics of Ostwald ripening in fault zones can be rapid due to the preponderance of small grains (Sleep, 1995) and high reactive specific surface area of the finest size fraction.

It is argued that the relatively small but consistent changes in the PSD distribution over a period of up to ten hours of hold time in the wet experiments described above (Fig. 5.8, 5.11, 5.12) can lead to larger changes over longer time periods. Textural evidence from the experimental data presented in chapter 3 is used to further this argument. These experiments were conducted over longer durations (up to eight weeks) using gypsum gouge in a similar sample geometry. The experiments were conducted under confining and pore pressure conditions identical to the present study. The total shear strain ($\gamma = 1.6$ similar to the present study) was achieved in several slide events interspersed with hold periods ranging between 1 to 21 days (hold-slide-hold tests). Backscattered SEM images for room dry and wet experiments are shown in Figure 5.13a and 5.13b respectively. The dry experiment was characterized by: distinctive grain shape and boundary, intergranular porosity, and common occurrence of open microfractures and other plastic deformation features. In comparison the wet experiment (Fig. 5.13b) exhibited: absence of distinctive grain shape and boundary, virtual obliteration of intergranular porosity, healed microfractures as observed from trails of fluid inclusions, and welded grain contacts. Besides features noted above evidence for pressure solution, recrystallization, and crack sealing is ubiquitous in these experiments with long hold times. These features are not unique to samples deformed in the laboratory but have been observed routinely in samples from exhumed natural faults (Labaume and Moretti, 2001; Hadizadeh, 1994; Chester and Logan, 1987).

In summary, the PSD evolution seen in the data presented here may be extrapolated to a longer time scales as observed in Figure 5.13a and by analogy to crustal deformation in fault zones. Deformation mechanisms such as pressure solution, crack sealing, recrystallization and Ostwald ripening that were operative in the long-term experiments (Fig. 5.13a) were also active in the

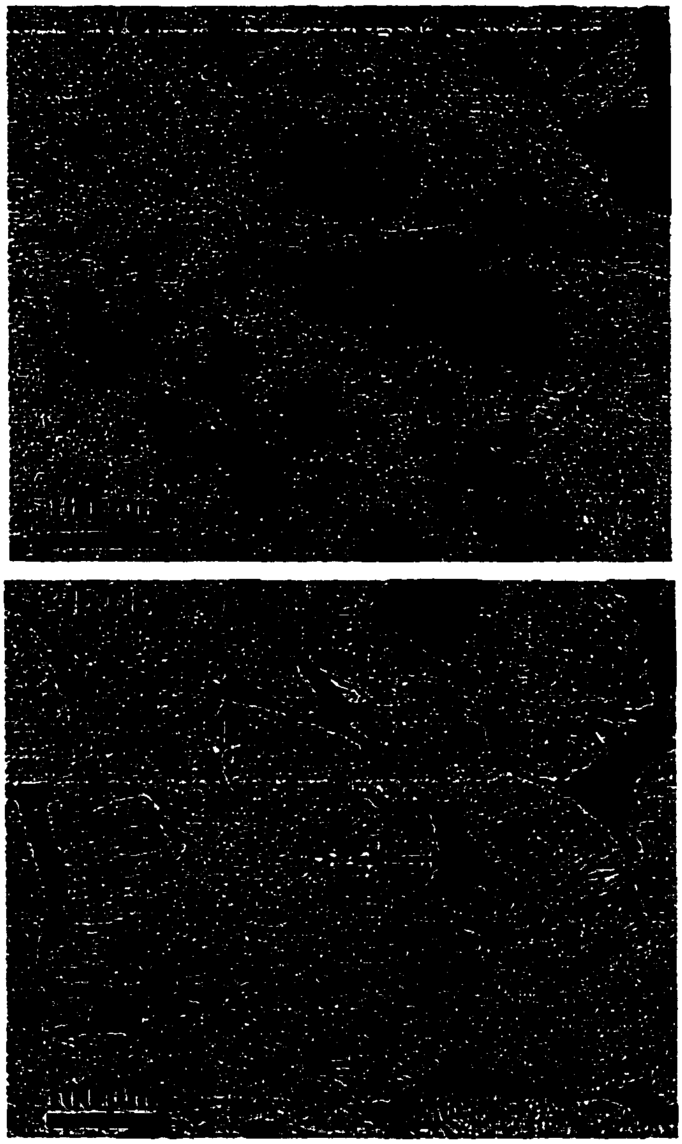

Fig 5.13: Backscattered scanning electron (SEM) photomicrograph showing contrast in texture between experimental gouge deformed wet (a) and dry (b). The wet gouge is characterized by welded grains (wb), healed microfractures indicated by fluid inclusion trails (hf) and recrystallization (c). Note distinct grain boundary (g), intergranular pore space (p) and abundant open microfractures (f) and intracrystalline deformation (i) in dry gouge and their absence in wet gouge. Deformation conditions were similar in both cases (P_e=13.8 MPa, about 60 days, and $\gamma = 1.6$).

shorter-term experiments reported here. Such mechanisms may cause the observed time-dependent PSD evolution.

Implications for Mechanics of Faulting

Most fault zones are composed of a significant quantity of rock flour or fault gouge and the relationship between particle size in the fault zone and frictional behavior has been established through detailed laboratory investigations (Biegel et al., 1989; Marone and Scholz, 1989; Sammis and Biegel, 1989; Chester and Logan, 1987; Dieterich, 1979; Byerlee et al., 1978). It has been observed that in the rate- and state-dependent friction formulation maximum or mean particle size has a strong influence on critical displacement amount (Sammis and Steacy, 1994; Dieterich, 1992). Coarsening such as that observed in this study can result in an increase in the critical displacement required during slip and this translates into an increase in the size of the slip nucleus. The size of the slip nucleus and its detection using seismological means are thought to be an integral part of earthquake prediction.

Earthquakes have also been thought of as rupture of cohesive gouge characterized by sharp stress drop at failure (Reches, 1999; chapter 3). Textural observations of two long-term laboratory hold-slide-hold experiments were discussed in the previous section (Fig. 5.13a and 5.13b). Slip characteristics for the dry (Fig. 5.13a) and wet cases (Fig 5.13b) were markedly different and have been described in chapter 3. The dry experiment resulted in stable sliding behavior with no development of cohesion while the wet experiment resulted in 25% or greater increase in cohesive shear strength and significant stress drop at failure. In the presence of pore fluid, and over long hold times, lithification through welding of grains, recrystallization and crack sealing results in a virtual obliteration of porosity (Fig. 5.13b). The textural and PSD evolution can be related to both increases in fault strength as well as the unstable nature of the slip weakening due to rupture of a cohesive gouge.

Recent evidence of rapid, time-dependent fault healing has emerged from fault zone guided waves (Li et al., 1998) and shear-wave splitting (Tadokoro et al., 1999) along active faults. These data sets suggest that rapid sealing of fractures alter fault zone properties after major seismic events. Li et al. (1998) observed a reduction in P- and S-wave velocity along the Landers fault over a two-year period that was interpreted to be due to a 1% reduction in microcrack density. Tadokoro et al. (1999) observed complete obliteration of shear fractures that formed during the 1995 Kobe earthquake within a period of 33 months. Moore et al. (2000) observed multiple episodes of fracture filling in cores recovered from the vicinity of the Nojima Fault. Observations in Figure 5.13a suggest that coarsening is accompanied by healing of fractures (see also chapter 4). Ostwald ripening drives both the coarsening and the filling of fractures in these experiments. By analogy fracture filling cement and the consequent reduction in microcrack density (Moore et al., 2000; Li et al., 1998; Tadokoro et al., 1999) may be driven by a process similar to that observed in the laboratory experiments presented here.

The permeability structure of a fault zone has been thought to be important in controlling fault strength and failure instability. Models that invoke localized failure along fault zones due to development of over pressurized compartments and subsequent rupture (Byerlee, 1993; Rice, 1992; Sleep, 1995) assume low fault zone permeability relative to that in the country rock. The evolution of permeability is thought to be a function of time-dependent creep mechanisms such as pressure solution and Ostwald ripening that drives spatially organized cementation and development of compartments. Simple models of permeability such as the Cozeny-Karman type relation or its modifications (Panda and Lake, 1994) depend on grain size parameters such as mean, variance and skewness besides the porosity. Evolution of tortousity is may also be a function of PSD parameters. The time-dependent PSD evolution as observed in the data presented may lead to marked changes in the porosity-permeability evolution in fault zones (compare Fig. 5.13a and 5.13b). Simple functional dependencies such as those established in this study between PSD parameters and shear or inter-seismic hold periods may provide a tool to address permeability evolution in fault zones during earthquake cycles.

Conclusions

A series of dry and wet experiments using gypsum gouge sandwiched between steel sliding blocks were conducted to investigate the PSD evolution as functions of incremental shear strain or hold time. Fault gouge created in the laboratory can be described by log-normal mass-size PSD for a fairly wide range of sizes especially for the coarse and medium sized fractions. However, a fractal number - size distribution provides a better representation for the extremely fine fraction. PSD data provide evidence for the existence of a grinding limit for crystalline gypsum at 1.6 - 1.7 microns.

PSD evolution during shear stands in contrast to its evolution during post-slip periods of quiescence. During shear the overall PSD experiences a fining trend due to grain breakage and wear. This is manifest as a decrease in mean particle size, increase in the spread leading to a wider range of particle sizes, and an increase in the skewness or asymmetry resulting from a creation of a fine tail. On the other hand, healing processes such as pressure solution, crack sealing and Ostwald ripening cast very different characteristics on the PSD parameters. The mean, spread and skewness of the PSD all increase as a function of hold time resulting in a coarsening of the gouge. In addition, the fractal dimension (*D*) increases with an increase in shear strain but has an inverse dependence on hold time. Fractal dimensions determined from these laboratory experiments are in agreement with that of fault gouge from natural fault zones.

The dynamics of PSD evolution carries implications for mechanical, textural and permeability evolution of fault zones. The effect of PSD dynamics in the evolution of fault zone friction or fault zone strength can have a direct bearing on current models of earthquake mechanics. Observations presented here and in chapters 3 and 4 may help explain rapid healing of active crustal faults immediately after damaging earthquakes.

References

Agterberg, F.P., 1995. Multifractal modeling of the sizes and grades of giant and supergiant deposits. International Geology Review 37, 1-8.

Anderson, J.L., Osborne, R.H., Palmer, D.F., 1980. Petrogenesis of cataclastic rocks within the San Andreas fault zone of southern California, U.S.A. Tectonophysics 67, 221-249.

Atteia, O., Kozel, R., 1997. Particle size distributions in waters from a karstic aquifer; from particles to colloids. Journal of Hydrology 201, 102-119.

An, L.J., Sammis, C.G., 1994. Particle size distribution of cataclastic fault materials from southern California: A 3-D study. Pure and Applied Geophysics.143, 203-227.

Biegel, R.L., Sammis, C.G.,.Dieterich, J. H., 1989. The frictional properties of a simulated gouge having a fractal particle distribution. Journal Structural Geology.11, 827-846.

Blanpied, M.L., Lockner, D.A., Byerlee, J.D., 1991. Fault stability inferred from granite sliding experiments at hydrothermal conditions. Geophysical Research Letters 18, 609-612.

Blenkinsop, T.G., 1991. Cataclasis and processes of particle size reduction. Pure and Applied Geophysics 136, p. 57-86.

Brace, W.F., Byerlee, J.D., 1966. Stick-slip as a mechanism for earthquakes, Science 153, 990-992.

Byerlee, J.D., 1978. Friction in rocks. Pure and Applied Geophysics 116, 718-727.

Byerlee, J., 1993. Model for episodic flow of high-pressure water in fault zones before earthquakes. Geology 21, 303-306.

Chester, F., Logan, J., 1987. Composite planar fabric of gouge from the Punchbowl Fault, California. Journal Structural Geology 9, 621-634.

Crovelli, R.A., Barton, C.C., 1993. Fractals and Pareto distribution applied to petroleum accumulation size distributions. U.S.G.S. Open File Report, 29p.

Dieterich, J.H., 1992. Earthquake nucleation on faults with rate- and state- dependent strength. Tectonophysics 211, 115-134.

Dieterich, J.H., 1979. Modeling of rock friction: 1. Experimental results and constitutive equations. Journal of Geophysical Research 84, 2161-2168.

Engelder, J.T., 1974. Cataclasis and the Generation of Fault Gouge. Geological Society of America Bulletin 85, 1515-1522.

Epstein, B., 1947. The mathematical description of certain breakage mechanisms leading to the logarithmic-normal distribution. Journal Franklin Institute 244, 471-477.

Gaudin, A.M., Meloy, T.P., 1962. Model and comminution distribution equation for repeated fracture. AIME Transactions 223, 43-50.

Hadizadeh, J., 1994. Interaction of cataclasis and pressure solution in a low-temperature carbonate shear zone. Pure Applied Geophysics 143, 255-280.

Harris, C.C., 1969. The application of size distribution equations to multi-event comminution processes. AIME Transactions 244, 343-358.

Houghton, J.C., 1988. Use of truncated shifted pareto distribution in assessing size distribution of oil and gas field. Mathematical Geology 20, 907-937.

Karner, S.L., Marone, C., 2001. Frictional restrengthening in simulated fault gouge: effect of shear load perturbations. Journal Geophysical Research 106, 19319-19337.

Kamer, S.L., Marone, C. and Evans, B., 1997. Laboratory study of fault healing and lithification in simulated fault gouge under hydrothermal conditions. Tectonophysics 277, 41-55.

Kendall, K., 1978. The impossibility of comminuting small particles by compression. Nature 272, 710-711.

Labaume, P., Moretti, I., 2001. Diagenesis-dependence of cataclastic thrust fault zone sealing in sandstones. Example from the Bolivian sub-Andean zone, Journal Structural Geology 23, 1659-1675.

Li, Y.G., Vidale, J.E., Aki, K., Fei, X., Burdette, T.R., 1998. Evidence of shallow fault zone strengthening after the 1992 M7.5 Landers, California, earthquake. Science 279, p. 217-219.

Marone, C., Scholz, C.H., 1989. Particle-size distribution and microstructures within simulated fault gouge. Journal of Structural Geology 11, 799-814.

Marone, C., Kilgore, B., 1993. Scaling of the critical slip distance for seismic faulting with shear strain in fault zones. Nature 362, 618-621.

Marone, C., Raleigh, C.B., Scholz, C.H., 1990, Frictional behavior and constitutive modeling of simulated fault gouge. Journal of Geophysical Research 95, 7007-7025.

Moore D.E., Lockner, D.A., Ito, H., Ikeda, R., 2000. Proceedings of the International Workshop on the Nojima Fault Core and Borehole Data Analysis. U.S.Geological Survey Open File Report 00-129, 159-165.

Morrow, C.A., Byerlee, J.D., 1989. Experimental studies of compaction and dilatancy during frictional sliding on faults containing gouge. Journal of Structural Geology 11, 815-825.

Morse, J.W., Casey, W.H., 1988. Ostwald processes and mineral assemblages in sediments, American Journal of Science 288, 537-560.

Olgaard, D.L., Brace, W.F. 1984. The microstructures of gouge from mining-induced seismic shear zone. International Journal Rock Mechanics, Mining Sciences, Geomechanics 20, 11-19.

Olsen, M.P., Scholz, C.H., Leger, A., 1998. Healing and sealing of a simulated fault gouge under hydrothermal conditions: implications for fault healing. Journal of Geophysical Research 103, 7421-7430.

Opoczky, L., Farnady, R. 1984. Fine grinding and states of equilibrium, Powder Technology 39, 107-115.

Panda, M.N., Lake, L.W., 1994. Estimation of single-phase permeability from parameters of particle-size distribution. American Association of Petroleum Geologists 78, 1028-1039.

Prasher, C.L., 1984. Crushing and grinding process handbook, John Wiley, 473p.

Reches, Z., 1999. Mechanisms of slip nucleation during earthquakes. Earth and Planetary Science Letters 170, 475-486.

Rice, J.R., 1992. Fault stress states, pore pressure distributions, and weakness of the San Andreas Fault. In: Evans, B., Wong, T-F., (Ed) Fault Mechanics and Transport Properties of Rocks, pp. 475-503.

Ruina, A., 1983. Slip instability and state variable friction laws. Journal of Geophysical Research 88, 10359-10370.

Sammis, C.G., Osborne, R.H., Anderson, J.L., Banerdt, M., White, P., 1986. Self-similar cataclasis in the formation of fault gouge. Pure and Applied Geophysics 124, 53-78.

Sammis, C.G., King, G., Biegel, R, 1987. Kinematics of gouge deformation. Pure and Applied Geophysics 125, 777-812.

Sammis, C.G., Biegel, R.L., 1989. Fractals, fault gouge and friction. Pure and Applied Geophysics 131, 255-271.

Sammis, C.G., Steacy, S.J., 1994. The micromechanism of friction in a granular layer. Pure and Applied Geophysics 142, 777-794.

Shimamoto, T., Logan, J.M., 1981. Effects of simulated fault gouge on the sliding behavior of Tennessee Sandstone: non-clay gouges. Journal of Geophysical Research 86, 2902-2914.

Sleep, N.H., 1995. Ductile creep, compaction, and rate and state dependent friction within major fault zones. Journal of Geophysical Research 100, 13065-13080.

Steefel, C.I., Van Cappellen, P., 1990. A new kinetic approach to modeling water-rock interaction: the role of nucleation, precursors and Ostwald ripening. Geochimica Cosmochimica Acta 54, 2657-2677.

Tadokoro, K., Ando, M., Umeda, Y., 1999. S wave splitting the aftershock region of the 1995 Hyogo-ken Nanbu earthquake. Journal of Geophysical Research 104, 981-992.

Turcotte, D.L., 1997. Fractals and chaos in geology and geophysics. Cambridge University Press, 300p.

Appendix 5A: Particle Size Distribution Representation

Normal and log-normal Distributions

One of the most commonly used statistical distributions is the normal or Gaussian (bell-shape) distribution with its distribution function of the form:

$$f(x)=\frac{1}{\sigma\,(2\pi)^{0.5}}\exp\left[-\frac{(x-\bar{x})^2}{2\sigma^2}\right] \tag{1}$$

where $\bar{x}$ is the arithmetic mean (the first moment) and σ(square root of variance, the second moment) the standard deviation. The normal distribution is symmetric about the mean, skewness (third-moment) is zero and extends to infinity. Particles that are a product of constrained comminution as in a fault zone or a ball-mill are asymmetric (skewed) with a large proportion of fines. This renders use of a log-normal function more appropriate for description of such processes. The log-normal distribution function attains the form:

$$f(x)=\frac{1}{x\sigma_y(2\pi)^{0.5}}\exp\left[-\frac{(\ln x-\bar{y})^2}{2\sigma_y^2}\right] \quad \text{for } x \geq 0 \tag{2}$$

where $\bar{y}$ and σ_y are the mean and standard deviation. Simple relations exist between these parameters and their counterparts from the normal distribution (Turcotte, 1997). It may be added that a log-normal distribution has been often observed to be representative of PSD's (mass-size) from natural fault gouge from San Andreas, San Gabriel and Lopez Canyon and other faults especially for the coarse gouge fraction (An and Sammis, 1994; Sammis et al., 1986; Olgaard and Brace, 1983; Anderson et al., 1980). Interestingly, log-normal distribution between number and size of particles have been predicted (Epstein, 1947) after multiple fracture events where fracture probability is independent of particle size. Prevalent fragmentation theories cannot explain a log-normal distribution in mass-size terms.

Fractal distributions

Fractal distributions between mass-size or number-size have been applied to describe PSD from both experimental and natural fault zones (An and Sammis, 1994; Sammis and Steacy, 1994; Blenkinsop, 1991; Biegel et al., 1989; Marone and Scholz, 1989). Numerical investigations also predict attainment of a D value close to 2.6 (Sammis et al., 1987). Mass-size fractal distribution is of the form:

$$\frac{M(x)}{M_T} = \left[\frac{x}{n}\right]^a \qquad (3)$$

where *M(x)* is cumulative mass under size *x*, M_T is the total mass, *n* is a scale parameter similar to mean, and *a* is the shape parameter. Essentially similar forms such as Gaudin-Meloy (1962) and Harris (1968) have been proposed and these provide extra parameters that offer curve-fitting flexibility. Number-size fractal relations are generally of the form:

$$N(x) \approx x^{-D} \qquad (4)$$

where D is the fractal dimension (slope of number-size plotted on logarithmic axes). Most values of D lie especially for fragmentation processes in the range $2 < D < 3$. This range of D can be related to the total volume of particles and their surface area. The upper and lower bound of the validity of a power-law relation are the upper and lower fractal limits. The upper limit is generally associated with the size of the object undergoing fragmentation and the lower limit by properties such as presence of flaws (Prasher, 1987). Often, the detection range of the instrument controls the lower limit. According to Turcotte (1997), for $0 < D < 3$ the upper limit is important as the volume (mass) of the fragments are predominantly in the larger fragments while for $D > 3$ the lower limit needs to be specified as the volume of the small fragments dominate. From a surface area point of view, for $0 < D < 2$ the upper bound need to be specified in order to constrain the surface area while for $D > 2$ the lower fractal limit is important as the surface area is dominated by the smaller fragments.

A closely associated form of the fractal distribution (number-size) is the Pareto distribution. The Pareto distribution has been previously used in analysis of aqueous suspensions of particles and colloids (Atteia and Ozel, 1997). It has also been used effectively in prediction of size of oil and gas fields or ore deposits (Houghton, 1988; Crovelli and Barton, 1993; Agterberg, 1995).

Exponential distributions

Finally, exponential relations also have been used to represent fragmentation products. A very popular form is the Weibull distribution

$$\frac{M(x)}{M_T} = 1 - \exp\left[-\frac{x}{n}\right]^a \tag{5}$$

where *n* and *a* are parameters similar to that in (3). The Rosin-Rammler is equivalent and has the form:

$$\frac{M(x)}{M_T} = \exp\left[-\frac{x}{n}\right]^a \tag{6}$$

The Weibull distribution (5) reduces to a fractal distribution (3) when *x* is small. Fractal dimension *D* (4) and *a* (3, 5,6) are related as $D = 3 - a$ (Turcotte, 1997).

Appendix 5B: Experimental and LPSA Measurement Reproducibility

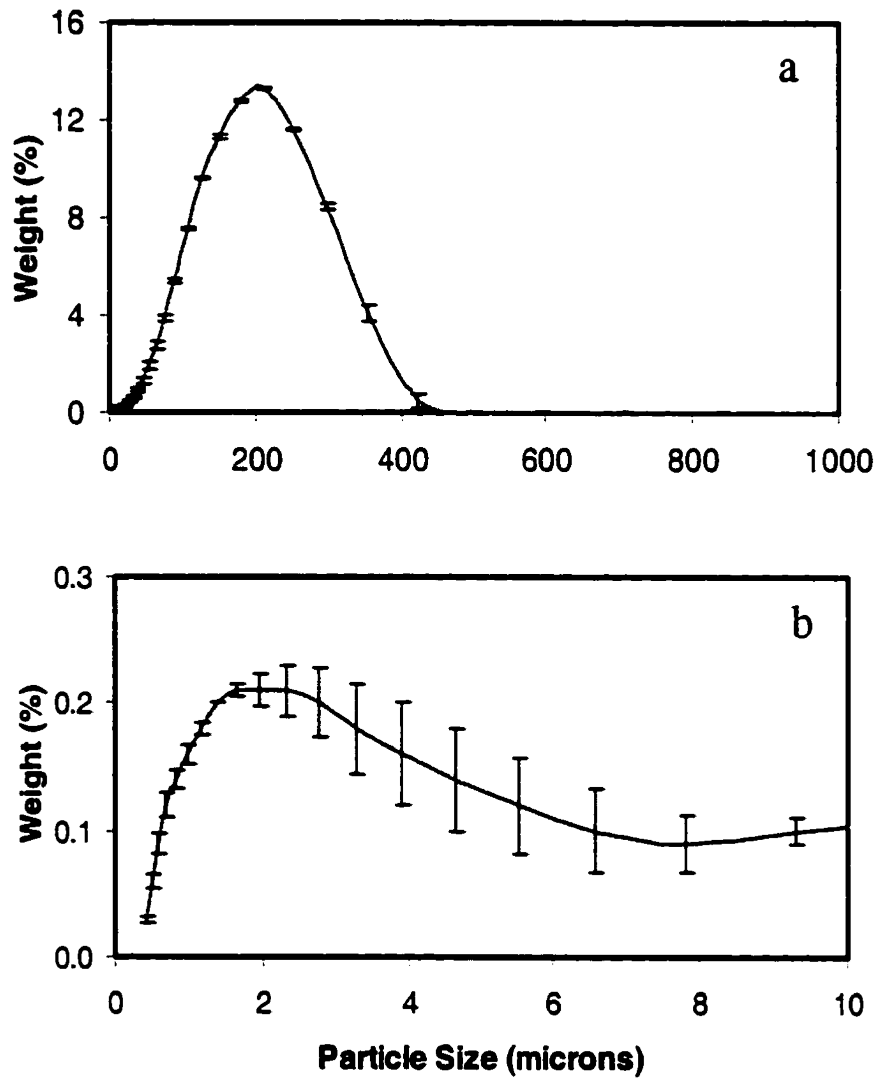

Fig. 5B.1: PSD analyses from two separate experiments using gypsum gouge under identical deformation conditions. The PSD and error bars represent a measure of the experimental variability and LPSA determination reproducibility. Note that the maximum error is smaller than the results obtained due to changes in experimental conditions. Log-normal means determined for the above data are 5.14 and 5.15 respectively. The variation is means as a function of shear strain is greater by an order of magnitude relative to this analytical error.

Chapter 6

Hydrostatic creep of wet calcite aggregates under elevated pressures and temperatures

Abstract

Hydrostatic compaction creep experiments were conducted on wet granular aggregates of calcite (Iceland Spar) at elevated pressures up to 6.9 MPa and temperatures ranging between 20°C and 200°C. All experiments were run at a pore pressure of 13.8 MPa. Four different initial grain sizes coarse (500-1000 μm), medium (250-500 μm), fine (125-250 μm) and very fine (63-125 μm) were used. Application of effective pressure resulted in a large accumulation of volume strain early in the loading history at lower temperatures. SEM observations and PSD data analyses suggest intense fracturing and granulation during this phase. The rapid increase in volume strain was however not instantaneous but took place over a duration of 1-2 hours. Subsequent strain accumulation was at much lower strain rates. High temperature experiments suggest an Arrhenius dependence at least for some grain size fractions though some ambiguity exists possibly due to the retrograde calcite solubility with temperature. In general, finer grain sizes exhibit higher strain rates at a given temperature. Initial grain size-creep rate systematics is not very well established due to intense granulation in the early loading process.

Nevertheless, grain size exponents ranging between –1.2 and –0.4 were obtained. SEM observations show dissolution textures such as etch pits, spiral dislocation lines, dissolution grooves along twin lamellae to be common. The abundance of dissolution features may explain grain size exponents near –1 in a reaction controlled creep system.

Time-dependent creep in the experiments presented here largely operates on a PSD that is much finer, poorly sorted and skewed relative to the initial grain size. Deformation mechanisms that alter PSD such as granulation early in the loading process leading to PSD fining or coarsening and lithification during later creep can exert a profound influence on creep rates. Further work is needed to isolate these effects in the creep process.

Introduction

Creep rates have been determined from aggregate, granular, hydrostatic compaction of silicate minerals such as quartz, albite, or quartz clay mixtures (Dewers and Hajash, 1995; Raj, 1982; Elias and Hajash, 1992), halite (Spiers and Schutjens, 1990), and gypsum (de Meer and Spiers, 1995). Several investigators reported creep data on limestone or marble under high temperatures and pressure (Robertson, 1960; Rutter, 1974). Results of hydrostatic creep experiments show fracturing and subsequent healing to be principal creep mechanism in limestone (Robertson, 1960). Dislocation creep under high-temperature for calcite single crystals has been reported (Wang et al., 1996; De Bresser, 1996). Although calcite is a major mineral in the shallow crust, low-temperature creep data on calcite is scarce.

Data on granular creep of calcite aggregates especially under diagenetic conditions may have several potential application areas. Firstly, limestone is an important stratigraphic member of deformed rocks of all geological ages from late pre-cambrian to recent. It is thus necessary to understand time-dependent deformational characteristics and geomechanical response of such rocks. Secondly, huge hydrocarbon reserves exist within carbonate reservoirs and unlike clastic rocks porosity evolution of limestone during burial in basinal-settings has not been a subject of frequent investigation. Carbonate reservoirs often preserve unusually high matrix porosity (Teufel et al., 1991) and creep of unconsolidated, granular calcite may be occurring in such reservoirs. Thirdly, compaction and creep in weak carbonate reservoirs such as the Ekofisk field has resulted in extensive damage to offshore platform facilities requiring extensive remedial work (Boade et al., 19989; Menghini, 1989). Finally, common deformation mechanisms such as cataclastic flow, pressure solution, dislocation flow, intracrystalline plastic flow via twinning and recrystallization are common in calcite at diagenetic temperatures and pressures. Fault zones in limestones are common and often mineralized with calcite (Hadizadeh, 1994; Kennedy and Logan, 1997) and flow of granular calcite is important to the understanding of the evolution of mechanical strength, texture, porosity and permeability of such fault zones.

Dewers and Hajash (1995) formulated a creep law for deformation of quartz aggregates. The form of the law linking volume strain rate to experimental variables of effective pressure (P_e), temperature (T), volume strain (ε) and grain size(d) is given by

$$\varepsilon = \frac{A}{d^n(1-\varepsilon)}\exp\left(-\frac{E_a}{RT}\right)\{\exp(\alpha Pe)-1\}\exp\left(-\frac{\varepsilon}{a}\right) \qquad (1)$$

A is the pre-exponential factor in the Arrhenius law, E_a is the activation energy, α measures the strength of the effective pressure dependence, R is the gas constant and n a grain size exponent determined from curve fits.

Hydrostatic granular creep experiments on angular Iceland spar calcite is reported in this chapter as a function of varying effective pressure, temperature and initial grain size. This is an initial step towards development of a creep law for granular calcite aggregates under elevated temperatures and pressures similar to equation (1). In addition to mechanical results multiple mechanisms such as microfracturing and pressure solution by which volume strain is accumulated in these experiments and their effect on evolution of grain size or particle size distribution (PSD) are also discussed.

Experimental Method

All the experiments were conducted with crushed Iceland spar calcite that was sieved into separate grain size fractions: 500-1000 μm (coarse), 250 – 500 μm (medium), 125-250 μm (fine), and 63-125 μm (very fine). The sieved fractions were washed repeatedly with distilled water to remove ultra-fine particles and oven-dried at 40°C. A known weight of the calcite granular aggregate was jacketed with heat-shrink Teflon sleeves into cylindrical samples (1.25 cm in diameter and about 5 cm long). Compaction experiments were conducted in a flow through pressure vessel capable of confining pressures up to 103 MPa and temperature of 500°C (Fig. 6.1). Sample end-pieces are made from a chemically inert alloy (Pyromet). Confining pressure was applied by a Sprague pump, while pore pressure was maintained by a graduated manual pressure generator capable of pore pressure up to 69 MPa. Pore volume measurements were also made with this pressure generator (resolution 0.0047 cm^3). Effective pressure for the experiments was 2.1, 3.4, 4.8 and 6.9 MPa commonly at a constant pore pressure of 13.8 MPa using distilled water as the pore fluid. Pore fluid withdrawn during compaction in order to maintain constant pore pressure was computed into volume strain. In addition to room temperature tests, higher temperature experiments were conducted at 70°C, 130°C and 200°C. Initial porosity was determined from the weight of calcite, sample length and diameter. This was checked using a water displacement technique and Helium porosimetry. The three techniques gave initial porosity values that are within 5% of one another. Sample loading involved: (a) an initial application of a small confining pressure (usually about 0.4 MPa) to maintain jacket integrity; (b) introduction of pore fluid into the sample at the upstream-end to drive all the air out and saturate the pore space with distilled water; (c) increase of pore pressure to the test conditions maintaining a small effective

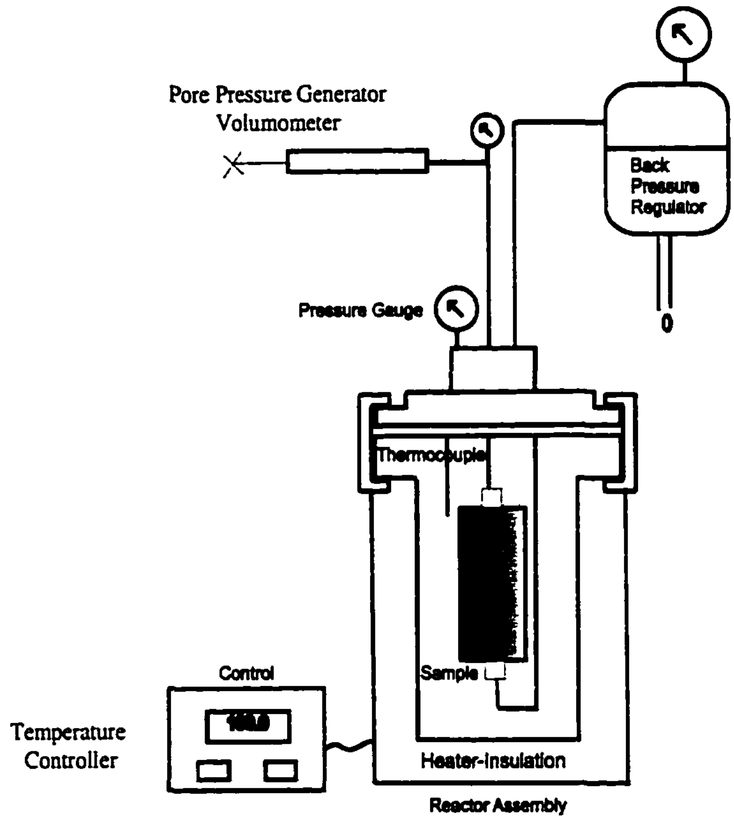

Fig. 6.1: Schematic diagram of the setup used for the calcite granular aggregate creep experiments. See text for description.

pressure for jacket integrity; (d) increase in confining pressure to the test pressure. While the room temperature experiments were loaded in the above manner elevated temperature experiments were taken to the temperature for the test at a rate of about 10°C/hr before application of effective pressure (between steps c and d). Deformed samples were observed under SEM or epoxied for preparation of optical thin-sections. Some deformed aggregates were analyzed for PSD using a laser particle size analyzer (Coulter Electronics Model LS 200 capable of analyzing particles within a size range 0.4-2000 μm).

Results

Role of effective pressure in calcite creep

Hydrostatic compaction creep experiments were run on a medium grained (250-500 μm) calcite aggregate typically over durations of 5-7 days, at room temperature. A constant pore pressure of 13.8 MPa was applied. Effective pressures of 2.1, 3.4, 4.8 and 6.9 MPa were used for the tests either as stress-steps on single samples or for individual experiments run at constant effective pressure. Experiments typically exhibit a rapid accumulation of volume strain within the first couple of hours followed by much slower increase over the next several days (Fig. 6.2a). Volume strain – time plots for tests at 2.1, 3.4, 4.8 and 6.9 MPa indicate a consistent strain-time relationship with effective pressure. A progressive increase in volume strain at successively higher effective pressures is observed (Fig. 6.2a). In a separate stress-stepping experiment over the same

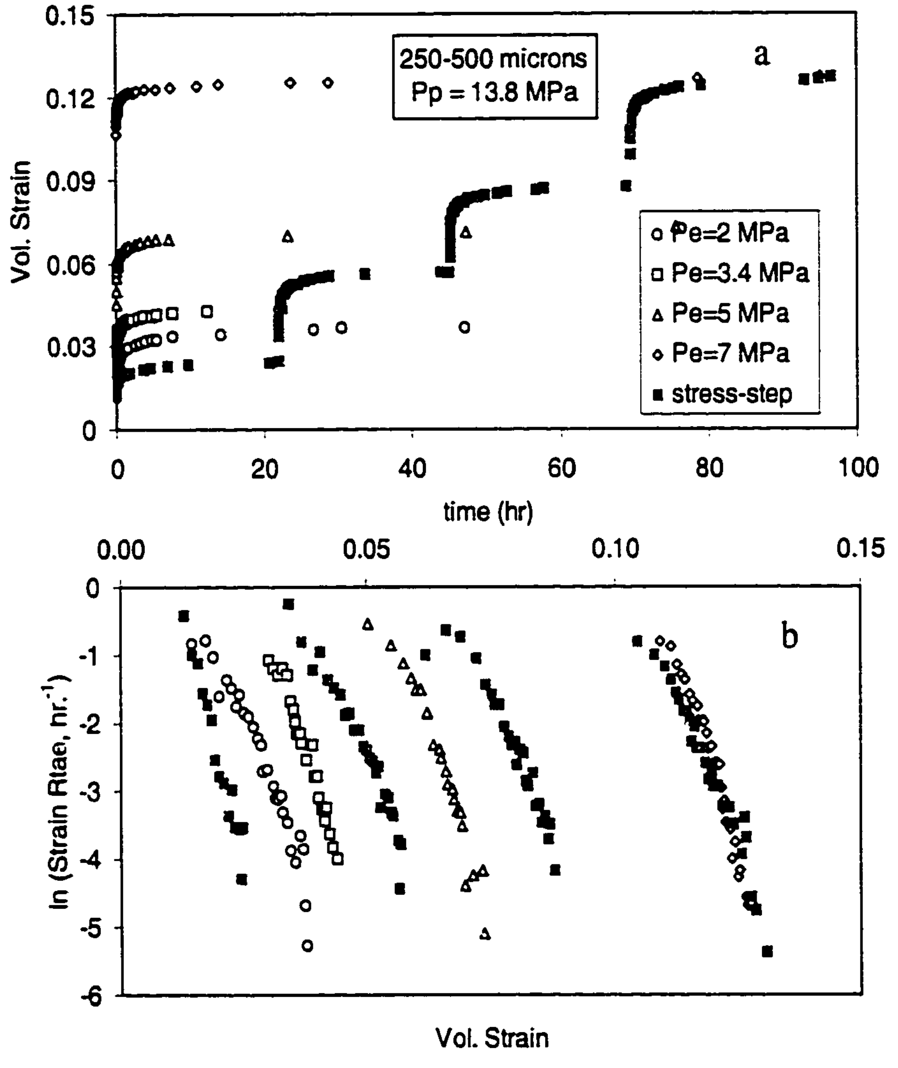

Fig. 6.2a:Volume strain – time plot for room-temperature experiments using medium grained (250-500 μm) aggregates at effective pressures 2.1-6.9 MPa and pore pressure of 13.8 MPa. A stress-stepping experiment at same effective pressure conditions has been included in the same plot (solid symbols). Note the progressive increase in volume strain at successively higher effective pressures.(b) ln (strain rate) plotted against volume strain for the same data set. The initial part of the curves exhibits a non-linear segment that is characterized by grain boundary sliding, fracturing and twinning. The slopes at higher strains in each effective pressure step are fairly linear and consistent.

effective pressure steps volume strain accumulates in a similar manner as a function of time (Fig. 6.2a, stress-stepping curve). The initial rapid increase is not entirely instantaneous plastic strain and occurs over a period of two or more hours and clearly exhibits time-dependency. The same data when plotted in ln(strain rate) – volume strain space reveals the two distinct phases of volume strain accumulation (Fig. 6.2b). The early strain rate is higher (gentler slope) followed by a progressive change in slope to a lower strain rate (steeper slope) deformation.

The PSD for the above suite of tests is presented in Figure 6.3. An increase in effective pressure results in: (a) decrease in the peak frequency, (b) shift of the center of the PSD towards finer sizes, (c) an increase in the spread of the distribution and, (d) an increase in skewness (Fig. 6.3b). This suggests that fracturing and granulation is one of the dominant deformation mechanisms of volume strain accumulation.

This is further corroborated by SEM investigation of the deformed granular aggregates (Fig. 6.4). Initially undeformed and clean grain surfaces devoid of any debris (Fig. 6.4a) become progressively covered with finer grained calcite that is a result of grain breakage at elevated effective pressures (Fig. 6.4b and 6.4c).

Empirical strain rate formulation

Experiments with other minerals such as quartz (Dewers and Hajash, 1995) or halite and gypsum (chapter 2) often exhibit a linear trend in ln(strain

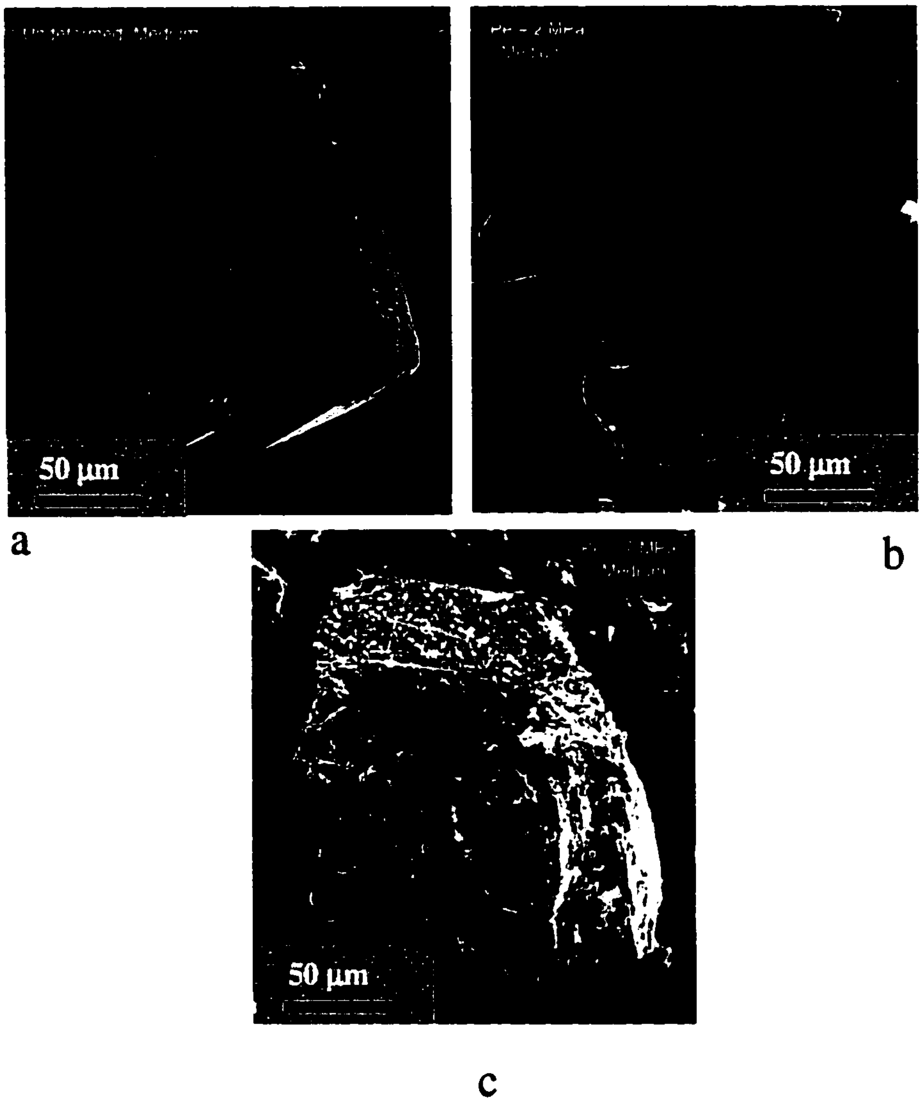

Fig. 6.3: SEM photomicrographs of surface features of individual calcite grain. (a) Top left is an undeformed grain with a clean and featureless surface. (b) Top right figure represents an individual grain deformed at P_e=2 MPa. Surface is fairly clean and the arrow indicates a grain contact fracture surface. (C) Bottom figure is for calcite deformed at 7 MPa effective pressure. The clean part of the surface (arrow) represents a grain contact where some pressure solution possibly occurred. Remainder of the surface is covered with calcite debris derived due to breakage of surrounding grains. Also note twin lamellae on surface of the grain.

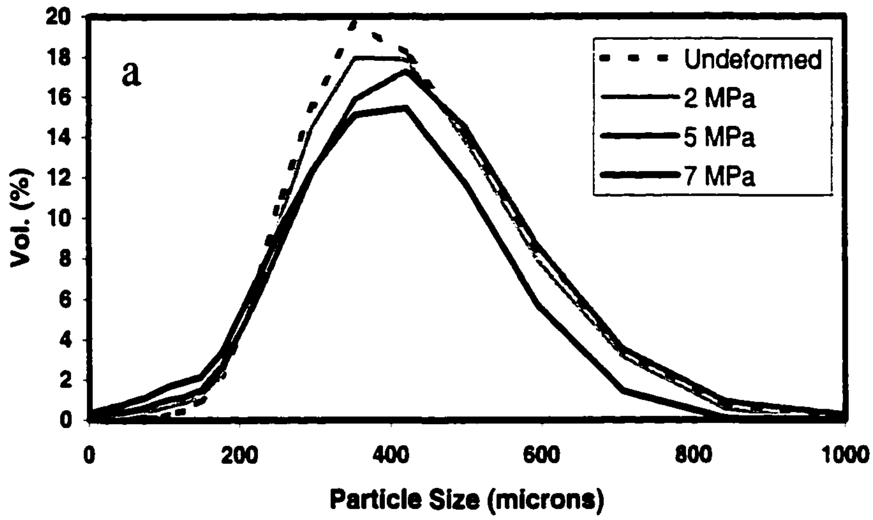

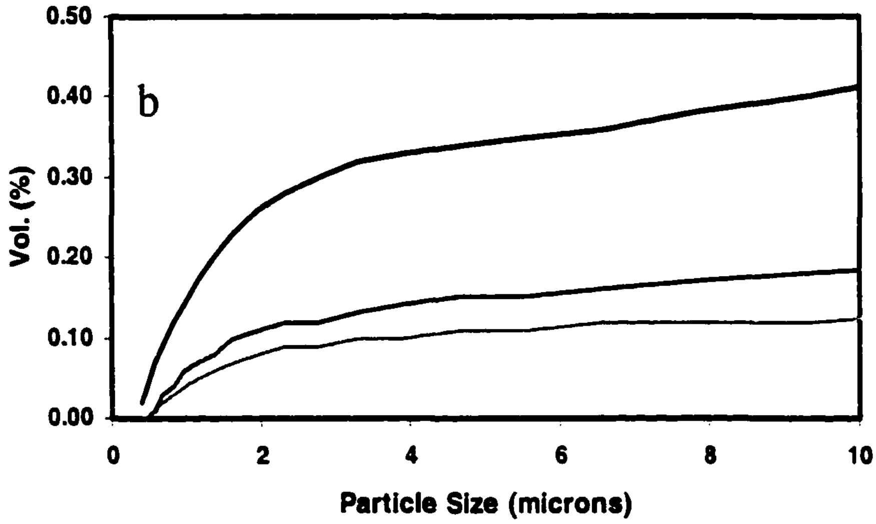

Fig. 6.4: Particle size distribution (PSD) evolution during aggregate granular hydrostatic creep of calcite aggregates. Figure represents volume percent of grain size fractions plotted against particle size diameter (in microns) and indicates progressive fining as a function of higher effective pressure. Note the decrease in peak, mean and an increase in standard deviation with increasing effective pressure. (b) Blow up of the finer grain size part of the plot showing the relatively large proportion of fines in higher effective pressure tests.

rate) – volume strain space. A linear slope is assumed to represent a single creep mechanism commonly pressure solution. Calcite is unique in that it commonly exhibits intracrystalline flow (twinning), fracturing and pressure solution over the range of temperatures and pressures in this investigation (Fig. 6.3, 6.4). Twinning and grain fracturing is especially common in the early strain history of the stressed aggregate but does not appear to be entirely instantaneous.

Dewers and Hajash (1995) arrived at an empirical strain rate formulation from experiments conducted with granular aggregates of quartz. It was based on the observation that volume strain accumulated at a constantly decreasing rate according to the following expression:

$$\varepsilon_v - \varepsilon_v^{\ 0} = a \ln(1 + \frac{t - t_0}{b}) \tag{2}$$

where, ε_v and ε_v^0 are volume strains at times t, and t_O respectively, and '*a*' and '*b*' are curve-fit coefficients. Differentiating equation (2) with respect to time yields the following for the time rate of change of strain:

$$\frac{d\varepsilon_v}{dt} = \frac{a}{b+t} = \frac{a}{b}\exp\{-\frac{\varepsilon_v - \varepsilon_v^{\ 0}}{a}\} \tag{3}$$

The above shows that the rate of volume strain decreases with the exponential of volume strain. It also indicates that the time rate of change of total strain is separable into strain-dependent and strain-independent parts. Letting ε_v^{lim} represent the "limiting" rate of volume change, i.e. that initial rate at zero strain, (3) can be expressed as:

$$\frac{d\varepsilon_v}{dt} = \varepsilon_v^{\lim} \exp(\frac{-\varepsilon_v}{a}) \quad \text{where } \varepsilon_v^{\lim} \equiv \frac{a}{b}\exp(\frac{\varepsilon_v^{0}}{a}) \tag{4}$$

Equation (4) yields a linear relationship when plotted as ln(strain rate) versus strain; examples of this are shown in Figure 2.1. In volumetric creep of fine grained quartz and calcite aggregates, a linear relationship is obtained, with a y-intercept equaling the $ln(\varepsilon_v^{lim})$ and slope of a^{-1} as defined in equation (4). Deviations from this behavior are observed for coarser grained aggregates, or for aggregates deformed at higher effective pressures. A combination of multiple deformation mechanisms that are operative simultaneously may introduce a non-linearity in the results when plotted in ln(strain rate) – volume strain space.

In order to isolate effects of multiple deformation mechanisms a modification is introduced to the rate formulation by addition of a first order rate term in equation (4). It can be written as:

$$\frac{d\varepsilon_v}{dt} = -k(\varepsilon_v - \varepsilon_b) \tag{5}$$

where k is the first-order rate coefficient and ε_b is a saturating value of volume strain that may be thought of as a sum total of poroelastic, and purely plastic or the instantaneous strain response due to loading. A first order rate term has been used for characterizing flow of solids previously (Gangi, 1981). Integrating the above with respect to time with the initial conditions of $\varepsilon_v = \varepsilon_v^0$ and time $t = t_0$ one arrives at:

$$\varepsilon_v = \varepsilon_b + (\varepsilon_v^0 - \varepsilon_b)\exp\{-k(t - t_0)\} \tag{6}$$

The sum of strain rates of equations (4) and (5) can then be written as:

$$\frac{d\varepsilon_v}{dt} = -k(\varepsilon_v - \varepsilon_b) + \varepsilon_v^{\lim} \exp(\frac{-\varepsilon_v}{a}) \quad (7)$$

The approach for analyses of the observed creep data was based on two primary steps. In the first step, early strain – time data was analyzed using equation (6) to obtain values for ε_b and k respectively. Subtracting ε_b from the measured value resets the volume strain data to reflect time-dependent strain only. In the second step, the data was cast as ln (strain rate) – volume strain and analyzed using equation (4). Use of this two-step approach avoids the use of equation (6) in a non-linear regression of strain rate – volume strain data. The essential part of data analyses involves characterization of ε_b, k, ε_v^{lim} and a^{-1} for their dependencies on effective pressure, temperature and grain size.

Analyses of the stress-stepping data for medium grained aggregate presented in Figure 6.2 suggests that ε_b is independent of effective pressure or the effective pressure increment. The rate coefficient k systematically decreases with an increase in effective pressure (Fig. 6.5). The possibility that the rate coefficient may decrease due to progressively lower porosities at every effective pressure step was also considered. Lower porosities are caused by the imposed strain history on the granular aggregate. In order to test this experiments were conducted with bimodal mixtures comprising of varying proportions of coarse and fine grain size fractions. Bimodal mixtures ensured a range of porosities. Observations on these experiments, not shown here, suggest that the first order rate coefficient k is independent of porosity.

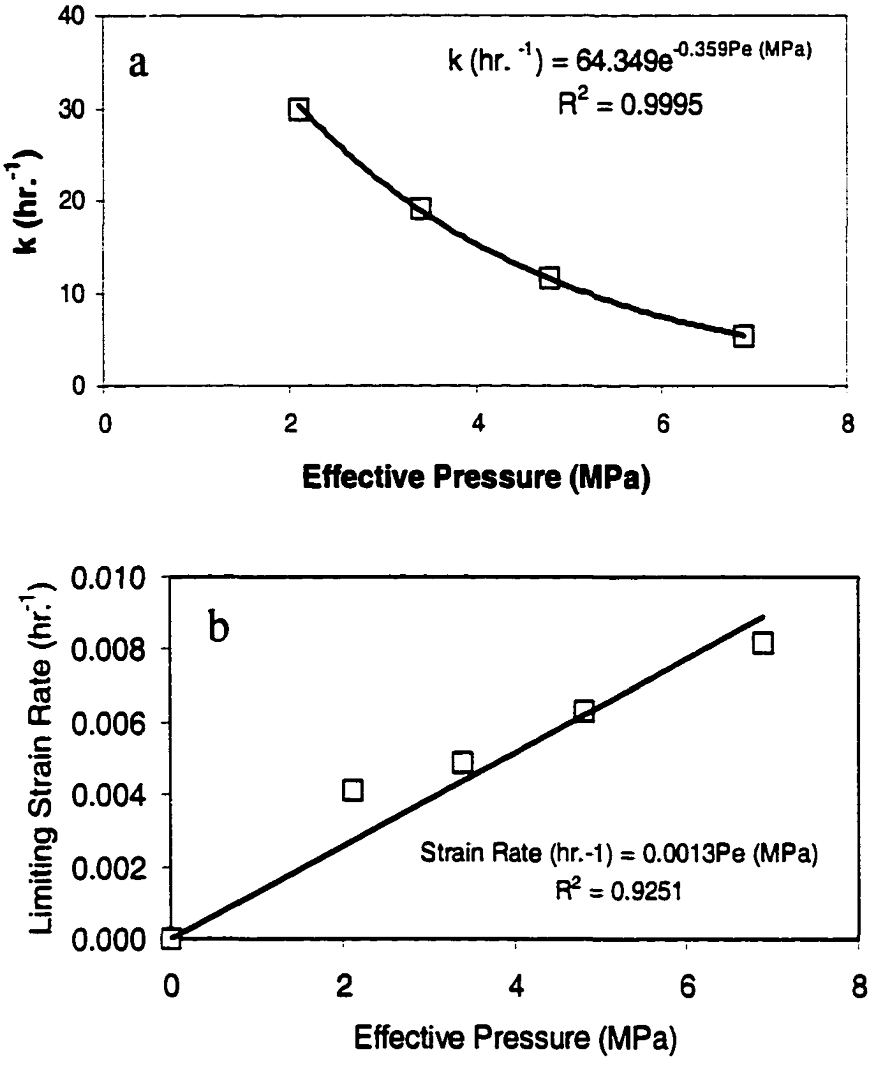

Fig.6.5a: The first order rate coefficient *k* plotted against effective pressure. The rate coefficient decreases with an increase in effective pressure. The curve fit function is noted. (b) Limiting strain rate versus effective pressure for creep of medium grain size fraction (250-500 μm) at room temperature and pore pressure of 13.8 MPa. A linear fit to the observed data is shown.

Time-dependent volume strain in excess of ε_b was analyzed in ln (strain rate) – volume strain space. The dependence of the strain rate (ε_v^{lim}) on effective pressure was determined by using a constant slope (a^{-1}) for all stress-steps. Dewers and Hajash (1995) observed that in experiments conducted with the same grain size and temperature a^{-1} was constant. The resulting intercepts are the initial strain rates (ε_v^{lim}). This data when analyzed exhibits a linear dependence of the limiting strain rate on effective pressure (Fig. 6.5b). The observations on creep of wet calcite reported previously (Fig. 2.3, chapter 2) exhibited an exponential dependence of the limiting strain rate on effective pressure for calcite and several other minerals. In this study, the maximum effective pressure applied is 6.9 MPa while the experiments reported in chapter 2 were loaded in effective pressure steps of 0.7 MPa to a maximum of 3.4 MPa. It appears that the exponential dependence observed in chapter 2 may be restricted to lower effective pressures.

Role of temperature

The influence of temperature on rates of kinetic data is commonly portrayed by the Arrhenius relationship. In this form the rate of a process (strain rate in this case) is proportional to exp($-E_a/RT$) where E_a is the activation energy, R the universal gas constant and, T the absolute temperature (in ^oK). In Figure 6.7 the Arrhenius dependence of the limiting strain rate is tested. Two different grain sizes, coarse (500-1000 μm) and fine (250-500 μm), are plotted. Both grain sizes exhibit a linear dependence of the limiting strain rate on

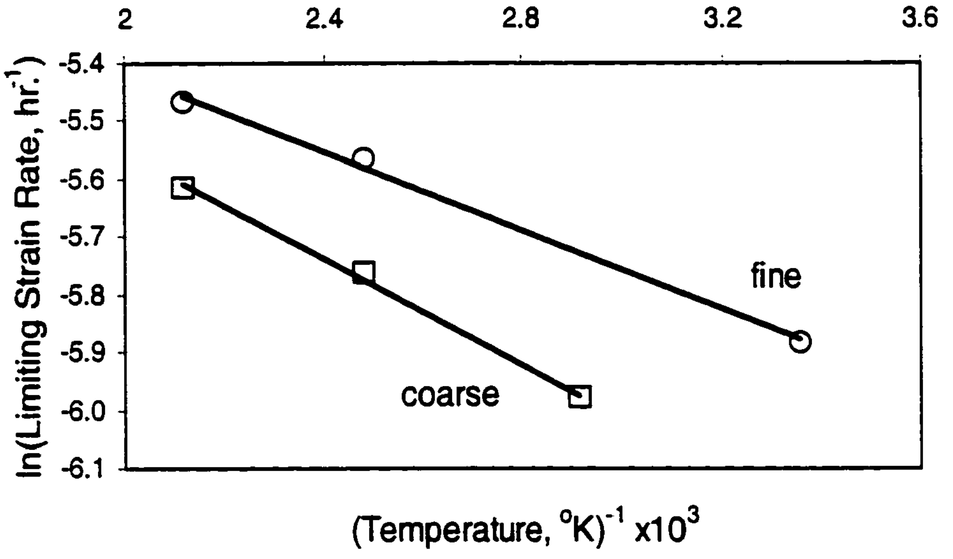

Fig. 6.6: Arrhenius plot of ln (limiting strain rate) versus reciprocal temperature for coarse and fine grain size aggregates. Experiments conducted at effective pressure of 3.4 MPa and pore pressure of 13.8 MPa. Lines represent linear fits to the data (slopes 456.9 and 338.9 for coarse and fine sizes respectively).

inverse absolute temperature with slightly higher strain rates for the finer grain size fraction. The slope of a linear fit in this type of plot equals the negative of the activation energy divided by the universal gas constant. This yields an apparent activation energy of 3-4 KJ/mole for the two grain size fractions analyzed. Activation energy determined from dissolution experiments for calcite-water reaction kinetics is higher by an order of magnitude then the values reported here (Plummer et al., 1978). The experiments conducted by Plummer and others were in an open system and over a smaller temperature range (15-48°C). Moreover, dissolution of calcite is controlled by different elementary reactions under varying pH and pCO_2 regimes. Different rate constants dominate dissolution in these regimes. The experiments in this study were all deformed under a closed system and the effect of atmospheric pCO_2 dissolved in the pore fluid at elevated temperatures inside the pressure vessel was ignored. More work is therefore needed to analyze the activation energy results in light of dissolution/precipitation kinetics data from the literature.

Role of initial grain size

Grain size data was analyzed to investigate the creep rate systematics at various temperatures. Strain rate – volume strain plots are presented in Figure 6.7. Strain rate – volume strain relationship between the various grain sizes are somewhat ambiguous at room temperature (Fig. 6.7a). Trends for the grain size fractions plotted are parallel suggesting no apparent differences in rates of volume strain accumulation. Creep rate systematics for the different grain sizes

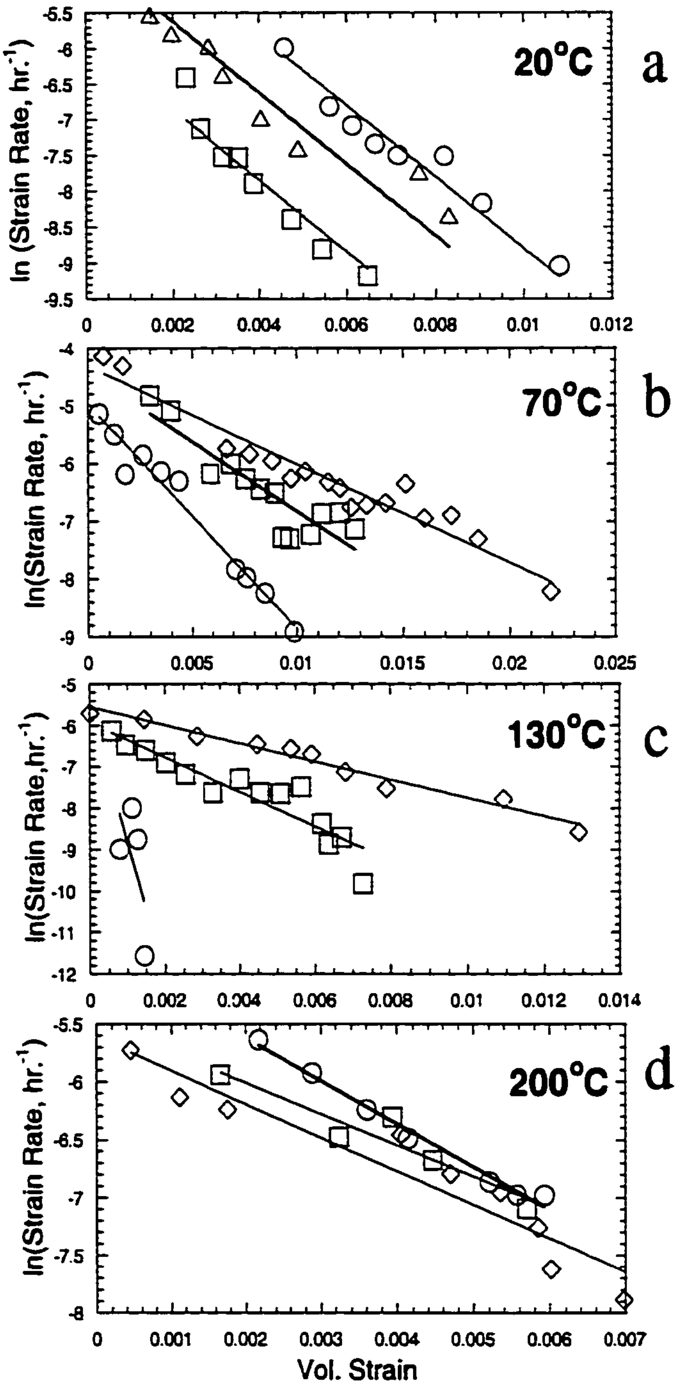

Fig. 6.7: A plot of ln(strain rate) against volume strain for various grain sizes at temperatures shown. Experiments conducted at 3.4 MPa and 13.8 MPa effective and pore pressures respectively. Lines represent linear fits to the data. (Symbols: circles-coarse; squares-medium; diamonds-fine; triangles-very fine).

are better established for higher temperature experiments (Fig. 6.7b at 70°C and Fig. 6.7c at 130°C). In these plots the various grain sizes exhibit distinctly diverging trends at longer times with finer sizes accumulating higher strains. The slopes grow progressively less steep for the finer sizes indicating higher rate of strain accumulation for the finer grain size fractions. At 200°C (Fig. 6.7d) the divergence at longer times or higher strains is subdued. This may be due to either a coarsening effect in the grain size distribution or may be attributed to incipient lithification or cementation at grain contacts.

Details of the creep process in light of the empirical formulation described previously (equations 4, 5 and 7) are given in Figure 6.8 and 6.9. The first order rate coefficient (*k*) shows a consistent linear increase with grain size for both room temperature and elevated temperature experiments with an apparent increase in slope with temperature (Fig. 6.8a). The slope (a^{-1}) for time-dependent creep increases with decrease in grain size. Strain rates are higher for finer grain sizes (Fig. 6.8b). Strain rates at elevated temperatures increase for the coarse and fine sizes (Fig. 6.6) while for the medium grain size strain rates tend to decrease with increase in temperature (less negative slopes at 70°C Fig. 6.8b). Strain rate – grain size trends at different temperatures are presented in logarithmic space in Figure 6.9. Results from experiments at 20°C, 70°C 130°C and 200°C are included in this plot. The slope in logarithmic space represents the grain size exponent in equation 1. It was shown in chapter 2 that for aggregates of calcite at room temperature the grain size exponent for creep

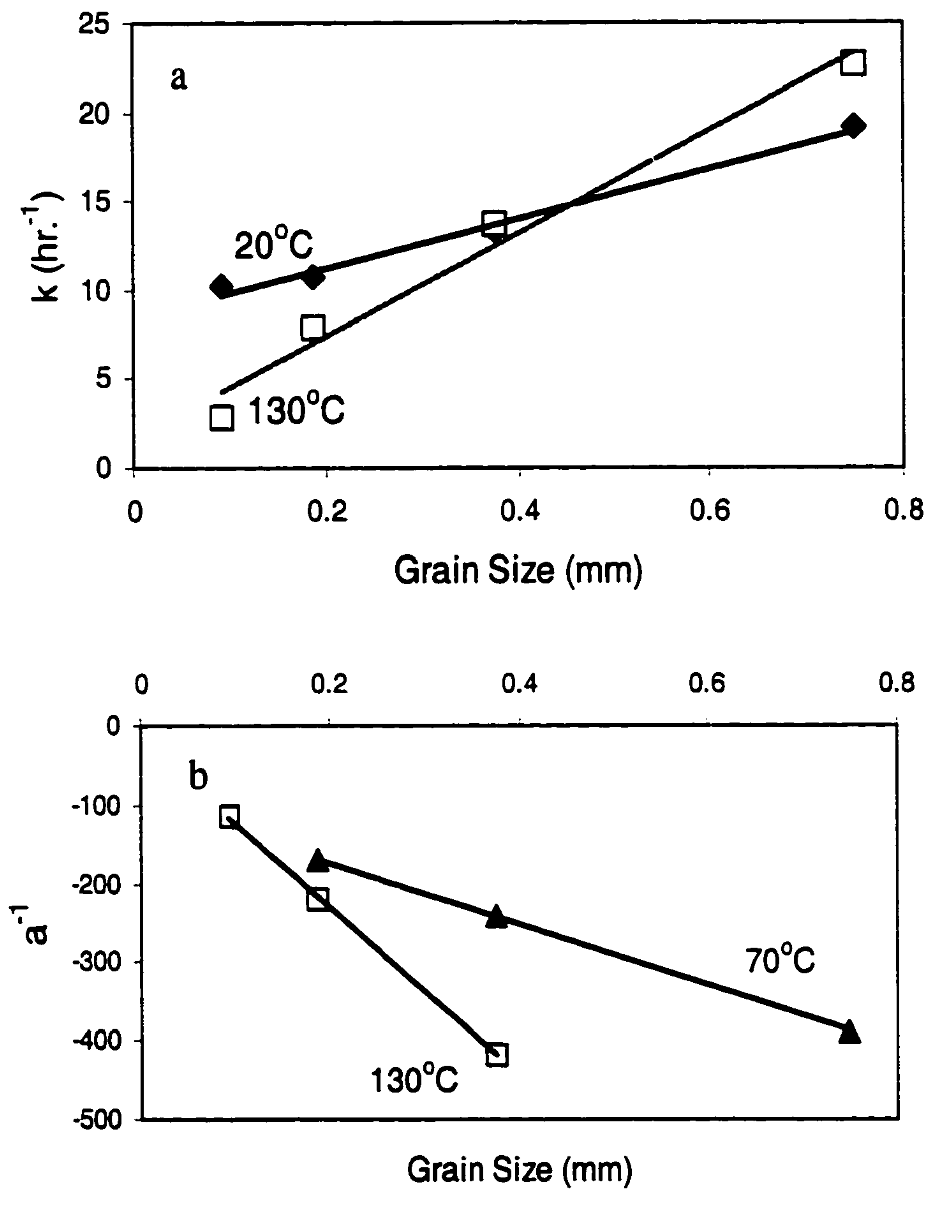

Fig. 6.8a:The first order rate coefficient (k) with increase in grain size at 20°C and 130°C, k increases with grain size for both temperatures. (b) Slope (a-1) of strain rate - vol. strain trend plotted against grain size for 70°C and 130°C experiments. The slope decreases with an increase in grain size. The lines represent linear fits to the data.

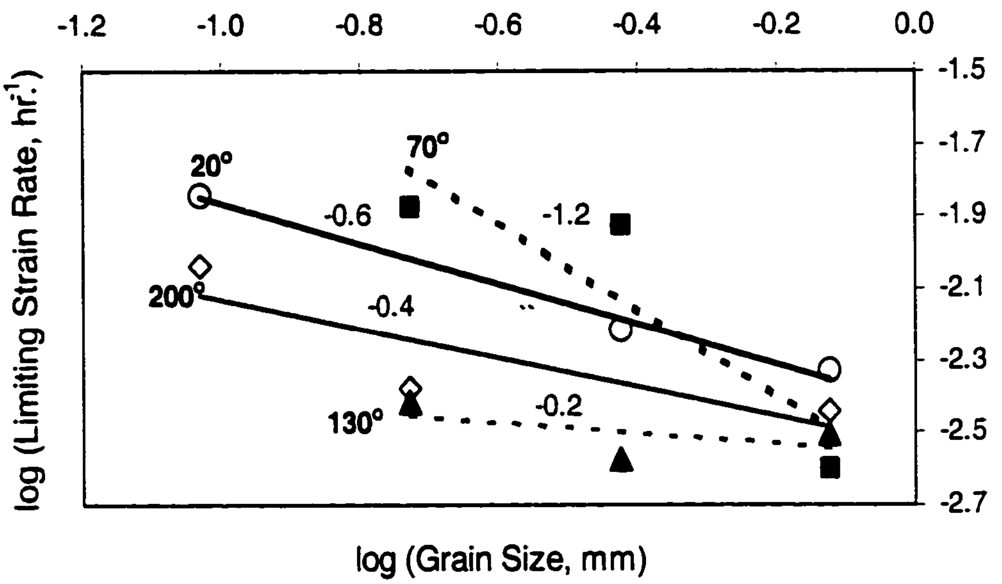

Fig. 6.9: Log (limiting strain rate) plotted against log(grain size) for various temperatures (°C). Effective pressure for experiments was 3.4 MPa and pore pressure 13.8 MPa. The lines represent fit to the data sets with the grain size exponent noted against each.

at lower effective stresses than experiments reported here is –2.3. The grain size exponents determined from Figure 6.9 range between -0.4 and -1.2. The exact cause of a much lower value of the exponent compared to the room temperature data is yet unknown. de Meer and Spiers (1997) reported a grain size exponent near -1 for uniaxial compaction of gypsum. A reaction-controlled mechanism is normally argued for a grain size exponent value close to 1 (de Meer and Spiers, 1997; Blenkinsop, 2000). This could suggest a change in mechanism for creep of calcite aggregates at elevated temperatures. In the following section evidence for extensive dissolution textures will be shown that may argue in favor of a grain size exponent close to –1.

Deformation mechanisms

Several primary deformation mechanisms were identified from examination of the deformed aggregates under the scanning electron microprobe (SEM). The deformation mechanisms may be broadly categorized into early-time loading related microfracturing and twinning and those related to longer-time dissolution of calcite. Twinning was more apparent in low temperature experiments and in coarser grain sizes (Fig. 6.3c). In nature twinning has been reported to be more common in coarse-grained sediments (Railsback, 1992; Newman, 1993). Microfracturing was ubiquitous in all the deformed samples especially in those deformed at room temperature. Samples were covered with ultra-fine debris from angular corners that spalled during initial application of effective pressure. Higher effective pressures led to a larger fraction of ultra-fine particles as observed in Figure 6.3c (SEM photomicrograph) and Figure 6.4b (PSD plot). PSD trends as a function of effective pressure exhibits a drop in peak frequency, a shift of the mean towards finer sizes and an increase in the skewness of the distribution. Tensile fractures with wing crack like extensions were observed (Fig. 6.10a). Intragranular microfractures were also observed and some of these may be due to time-dependent, sub-critical fracturing (Fig. 6.10b). Interestingly, experiments at elevated temperatures resulted in longer intragranular fractures than were observed in room temperature experiments.

Polygonal dissolution etch pits on the surface of the deformed grains were common and extended up to 10 μm in size (Fig. 6.11). Their morphology varied from being fairly smooth and angular at lower temperatures (Fig. 6.11a) to being much more irregular at elevated temperatures (Fig. 6.11b). A surface-damage halo was associated with dissolution pits formed at 130°C and 200°C (Fig. 6.11b). Twin lamellae were often observed to be the site of enhanced dissolution with material removal resulting in grooves along them. Pressure solution contacts were difficult to identify but appeared to be relatively smoother (and debris free) relative to the surrounding grain surface and also devoid of etch pits, striations or spiral dislocation lines (Fig. 6.12a). Intricate step-like dissolution patterns were observed on the surface (Fig. 6.12b) similar to that reported from atomic force microscopy (Blenkinsop, 2000; Gratz, 1991). Incipient lithification was commonly observed for experiments at 130°C or

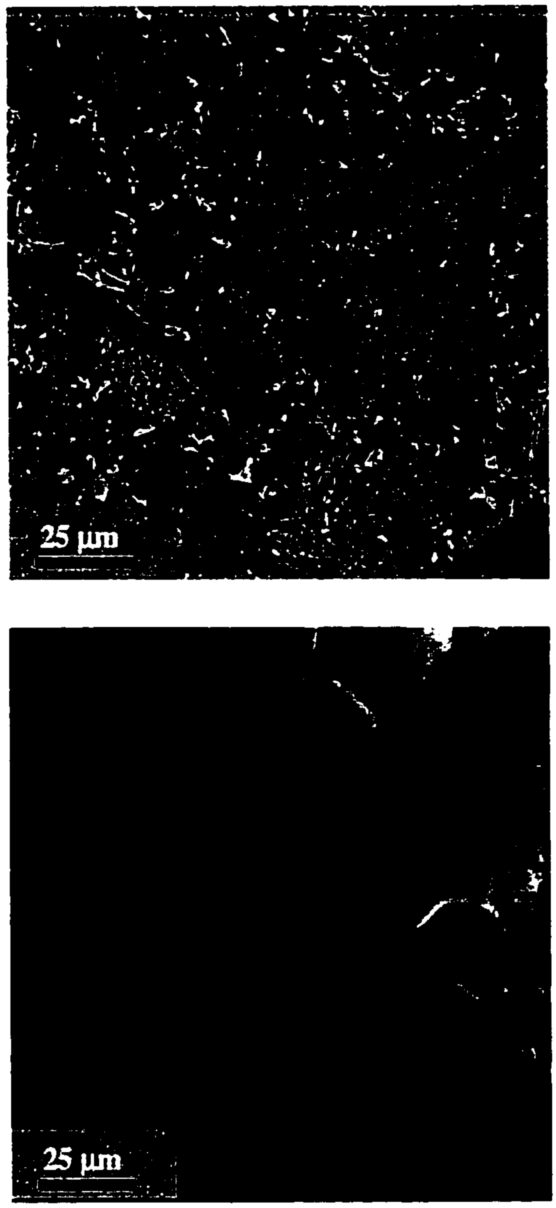

a

b

Fig. 6.10: SEM photomicrographs showing (a) tension (Griffith like) fractures developed in a coarse (500-1000 µm) calcite grain deformed at 130°C for a period of two weeks (arrow). Also note the vertical striations formed by dissolution on the grain surface. (b) Intragranular microfracture in a medium grained (250-500 µm) calcite deformed at 130°C.

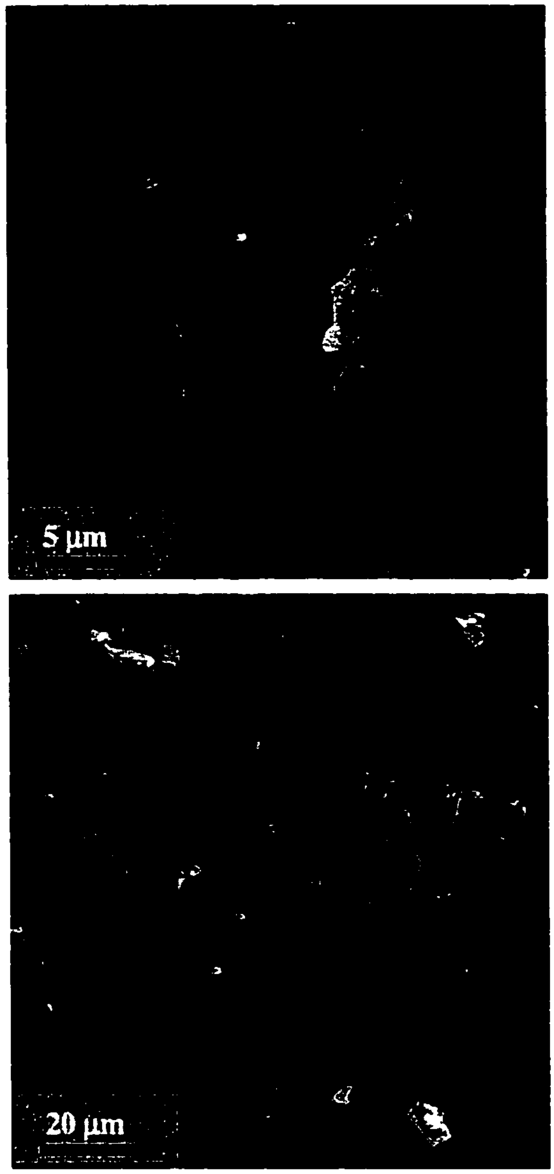

Fig. 6.11a: Polygonal dissolution etch pit (arrow) in very fine grained (63-125 µm) calcite grain deformed at 130°C. Dissolution may have been caused by impingement of an adjacent calcite grain. (b) Multiple dissolution pits formed on the surface of coarse (500-1000 µm) calcite grain deformed at 70°C.

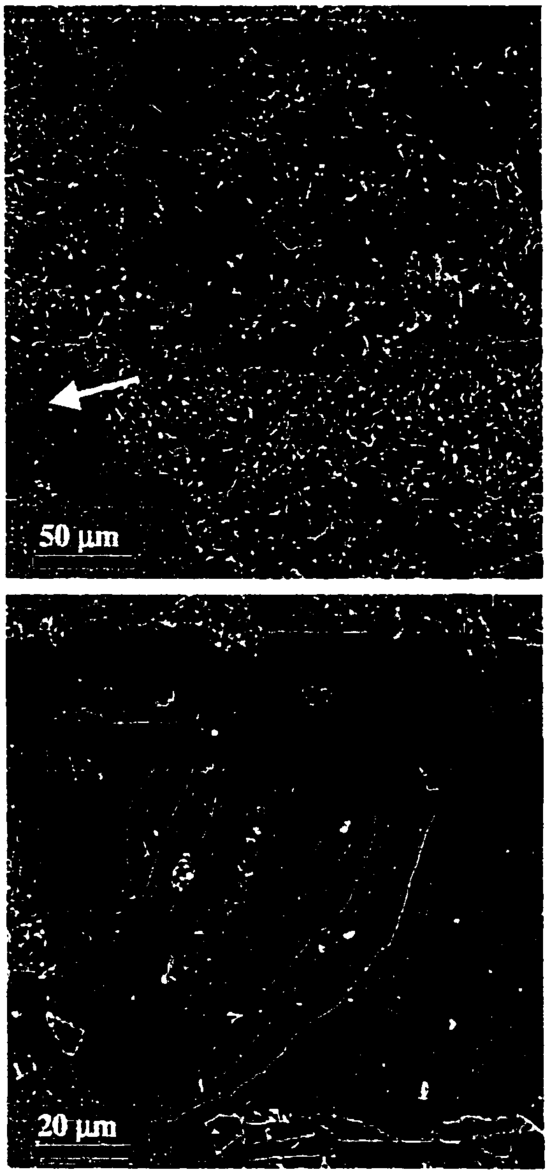

a

b

Fig. 6.12a: Coarse (500-1000 µm) grained calcite deformed at 130°C. Surface exhibits some granulation zones that are inferred to be along grain contacts (dark arrow). The relatively smooth surface may reflect pressure solution contact (light arrow). (b) Intricate step like feature formed due to dissolution of calcite deformed under identical conditions as in (a).

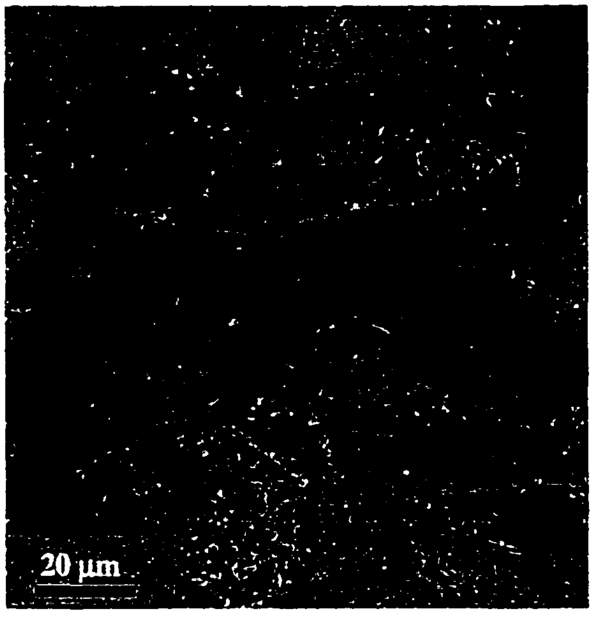

Fig. 6.13: SEM photomicrograph of an experiment conducted on coarse-grained aggregate at 130°C over 2 weeks. Effective pressure maintained at 3.4 MPa. Grains appear to be cemented together. Pronounced dissolution along the grain boundaries in the form of spiral dislocation lines can be seen (arrow).

200°C especially those that were conducted for longer periods (Fig. 6.13). Each grain cluster would typically be comprised of 5-10 grains. Spiral dislocation lines were often associated with such grains (Fig. 6.13). PSD data reflects incipient lithification and bonding together of grains (Fig. 6.14). Apparent coarsening is observed in PSD plots of very fine aggregates (initial size 63-125 μm) at elevated temperatures with marked increase in proportion of sizes beyond 150 μm. This coarsening is absent in experiments at low temperature. The coarsening may be due to cementation of grains (Fig. 6.13). The cement may be sourced from dissolution along free-faces of the calcite grains in contact with the pore fluid or Ostwald ripening of the ultra-fine debris that are developed during the process of initial loading (chapter 5).

Summary

Hydrostatic creep experiments of wet calcite aggregates were conducted at effective pressures higher than reported before (chapter 2) and at elevated temperatures (up to 200°C). Room temperature experiments at effective pressures up to 6.9 MPa resulted in significant volume strains within the first few hours of loading followed by slower strain accumulation over a period of days. The rapid initial strain is not instantaneous. In contrast to experiments on calcite described earlier (chapter 2) these resulted in non-linear trends when plotted in ln (strain-rate) – volume strain space. Deformed samples were characterized by ultra-fine debris resulting from spalled corners and edges. PSD data clearly showed evidence of cataclasis with creation of a skewed

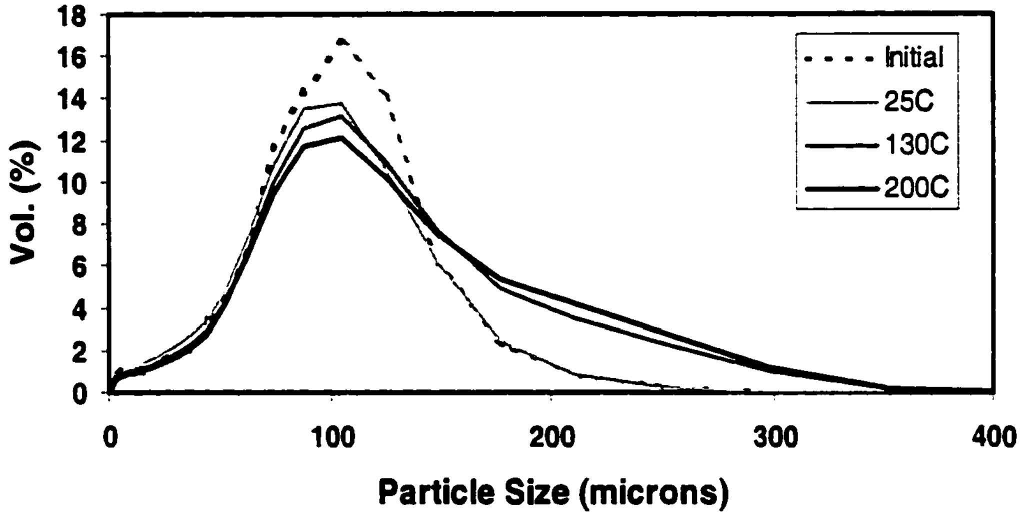

Fig. 6.14: Particle size distribution evolution (PSD) for the previously plotted data experiment set. In the volume (%) particle size plot there appears to be coarsening with an increase in temperature. It can be noted that experiments at 130°C and 200°C exhibits marked increase in vol(%) of sizes beyond150 μm, while the room temperature experiment shows no observable coarsening effect.

distribution with significant proportions of ultra-fine particles. The limiting strain rate obtained from stress-stepping experiments exhibited linear dependence on effective pressure unlike the exponential dependence previously observed at lower stresses. Certain grain sizes showed an Arrhenius dependence with reciprocal temperature. At elevated temperatures especially at 70°C and 130°C higher strain rates were obtained for finer grain sizes. Strain rates at room temperature were similar for all grain sizes. A grain size exponent ranging between −1.2 and −0.4 was determined from these experiments compared to −2.3 from the earlier study. Dissolution textures such as etch-pits, spiral dislocation lines and dissolution along steps were commonly observed. Pressure solution features were difficult to identify but may be present though less commonly than textures generated by dissolution. The textural characteristics suggest a reaction controlled creep process.

Extensive fracturing early in the loading process creates a poorly sorted aggregate with a wide PSD rather than a starting aggregate with a narrow size distribution. The granular aggregate undergoing time-dependent creep has very different textural characteristics relative to the starting material. The initial grain size –creep rate systematics is affected as a result. At higher temperatures the PSD or the nature of the grain contact may be altered due to processes such as Ostwald ripening resulting in incipient lithification. In addition, at high temperatures calcite solubility is retrograde with temperature. Although not yet established this may be responsible for some ambiguity in the high-temperature data presented here.

References

Blenkinsop, T., 2000. Deformation Microstructures and Mechanisms in Minerals and Rocks Kluwer, Dordrecht, 150p.

Boade, R.R., Chin, Y.L., Seimers, W.T., 1989. Forecasting of Ekofisk reservoir compaction and subsidence by numerical simulation. Journal of Petroleum Technology, 723-728.

De Bresser, J.H.P., 1996. Steady state dislocation densities in experimentally deformed calcite materials; single crystals versus polycrystals. Journal of Geophysical Research 101, 22189-22201.

de Meer, S., Spiers, C., 1995. Creep of wet gypsum aggregates under hydrostatic loading conditions. Tectonophysics 245, 171-183.

de Meer, S., Spiers, C., 1997. Uniaxial compaction of wet gypsum aggregates. Journal of Geophysical Research 102, 875-891.

Dewers, T.A., Hajash, A., 1995. Rate laws for water-assisted compaction and stress-induced water-rock interaction in sandstones. Journal of Geophysical Research 100, 13,093-13,112.

Elias, B.P., Hajash, A., 1992. Changes in quartz solubility due to effective stress: An experimental investigation of pressure solution. Geology 20, 451-454.

Gangi, A.F., 1981. A constitutive equation for one-dimensional transient and steady state flow of solids. In: Carter, N.L., Friedman, M., Logan. J.M. Stearns, D.W. (Eds), Mechanical Behavior of Crustal Rocks: The Handin Volume. American Geophysical Union Monograph 24, pp. 275-285.

Gratz, A.J., 1991. Solution-transfer compaction of quartzites; progress toward a rate law. Geology 19, 901-904.

Hadizadeh, J., 1994. Interaction of cataclasis and pressure solution in a low-temperature carbonate shear zone. Pure and Applied Geophysics 143, 255-280.

Kennedy, L.A., Logan, J.M., 1997. The role of veining and dissolution in the evolution of fine grained mylonites; the McConnell Thurst, Alberta. Journal of Structural Geology 19, 785-797.

Menghini, M.L., 1989. Compaction monitoring in the Ekofisk area chalk fields. Journal of Petroleum Technology, 735-739.

Newman, J., 1994. The influence of grain size and grain size distribution on methods for estimating paleostresses from twinning in carbonates. Journal of Structural Geology 16, 1589-1601.

Plummer, L.N., Wigley, M.L., Parkhurst, D.L., 1978. The kinetics of calcite dissolution in CO_2-water systems at 5° to 60°C and 0.0 to 12.0 atm CO_2. American Journal of Science 278, 179-216.

Railsback, B., 1993. Control of crystal shape and size on formation of twin lamellae in calcite: implications for deep burial diagenetic fabrics in limestones. Carbonates and Evaporites 8, 156-162.

Raj, R., 1982. Creep in polycrystalline aggregates by matter transport through a liquid phase. Journal of Geophysical Research 87, 4731-4739.

Robertson, E.C., 1960. Creep of Solenhofen limestone under moderate hydrostatic pressure. In: Griggs, D.T. (Ed), Rock Deformation-A Symposium, Geological Society of America Memoir, pp. 227-244.

Rutter, E.H., 1974. the influence of temperature, strain rate and interstitial water in the experimental deformation of calcite rocks. Tectonophysics 22, 311-334.

Spiers, C.J., Schutjens, P.M.T.M., 1990. Densification of crystalline aggregates by fluid-phase diffusional creep. In: Barber, D.J., Meredith, P.G. (Eds), Deformation Processes in Minerals, Ceramics and Rocks, Unwin-Hyman, Boston, pp. 334-353.

Teufel, L., Rhett, D.W., Farrell, H.E., 1991. Effect of reservoir depletion and pore pressure drawdown on in situ stress and deformation in the Ekofisk Field, North Sea. In: Roegiers, J-C. (Ed). Rock mechanics as a Multidisciplinary Science, Balkema, Rotterdam, pp. 63-72.

Wang, Z.C., Bai, Q., Dresen, G., Writh, R., Evans, B., 1996. High temperature deformation of calcite single crystals. Journal of Geophysical Research 101, 22189-22201.

Appendix 6A: Experimental Procedure

The experimental procedure followed for the granular aggregate creep experiments conducted with calcite (Iceland Spar) is given below:

1. Crushed calcite was sieved into separate grain size fractions.
2. Each sieved grain size fraction was washed repeatedly with water to remove ultra-fines and then oven dried at 40°C.
3. A 5 cm long piece of Teflon tubing (originally 3.75 cm in diameter) was cut and then heat-shrunk to 2.5 cm diameter by sliding the un-shrunk tubing on to a 2.5 cm diameter aluminum pipe.
4. After the shrunk Teflon tubing cooled this was then slid and fit on to a Pyromet end-piece by using a compression ring fitting as illustrated in Fig. 6A.1. The fit should be fairly square to ensure proper seal. The taper on the end-piece ensures proper fit using a compression ring.
5. About 40 gm of the sample aggregate was weighed and poured into the tubing that was fit at one-end with a Pyromet end-piece.

6. The sample was sealed by compression fitting of the second end-piece on to the Teflon tube holding the sample aggregate.
7. Sample height was measured and recorded together with the sample weight.
8. The sample was attached to the top-piece of the pressure vessel with the help of the upstream and downstream pore-pressure fittings.
9. The top piece of the pressure vessel with the sample attached is lowered inside the body of the pressure vessel filled with distilled water (confining medium).
10. The pressure vessel top is torqued down using a torque wrench set at a maximum of 35 lb./ft in increments. The torque steps followed were 15, 25, 30 and 35 lb/ft.
11. The pressure vessel is lowered into the loading assembly into the pressure vessel slot (Fig. 6A.1).
12. Confining pressure and upstream pore pressure port connections from the loading assembly to the pressure vessel were made.
13. A 20-40 psi (0.14-0.28 MPa) confining pressure was applied to maintain jacket integrity during flow-through.
14. The pore pressure system (cart Fig. 6A.1) was hooked up at the upstream end of the sample.
15. Pore fluid (distilled water) was flown through the sample for about 5 minutes to ensure complete saturation of the sample using the Eldex pump.
16. The downstream pore pressure connection was made (sample at this stage is closed to the atmosphere).
17. A small pore pressure of about 20 psi (0.14 MPa) was applied using either the Eldex pump or the syringe pump. The vernier scale on the pore pressure syringe pump (pore volume stroke) was recorded at every stage from this point onwards.
18. Both confining and pore pressure (with the syringe pump after valving off the Eldex pump on the cart) was increased to 2000 psi (13.8 MPa).

19. System was allowed to sit at nearly zero effective pressure for a few minutes to check for leaks.
20. Temperature was increased (in the case of elevated temperature experiment) using the temperature controller on the loading assembly (rate about 10°C/hr).
21. The back-pressure regulator at the downstream pore pressure end (dome pressurized to 2000 psi or 13.8 MPa) was used to continuously drain pore fluid due to increase in temperature. The confining pressure needs to be reduced from time to time to maintain nearly zero effective pressure on the sample during temperature increase.
22. Effective pressure for the experiment was applied by increasing the confining pressure.
23. Pore pressure was kept constant at 2000 psi (13.8 MPa) for the entire experiment. Pore volume stroke from the syringe pump was recorded every half or one minute for the first ten minutes, then stroke was recorded as per the intensity of change in pore pressure to ensure a smooth and representative volume strain-time data.
24. Unloading involved reduction in temperature followed by pore and confining pressure in a way so that no additional volume strain was imposed during the unloading process.
25. The pore volume stroke-time data was analyzed on a spreadsheet program.
26. Initial porosity for each grain size was determined by a water displacement technique.

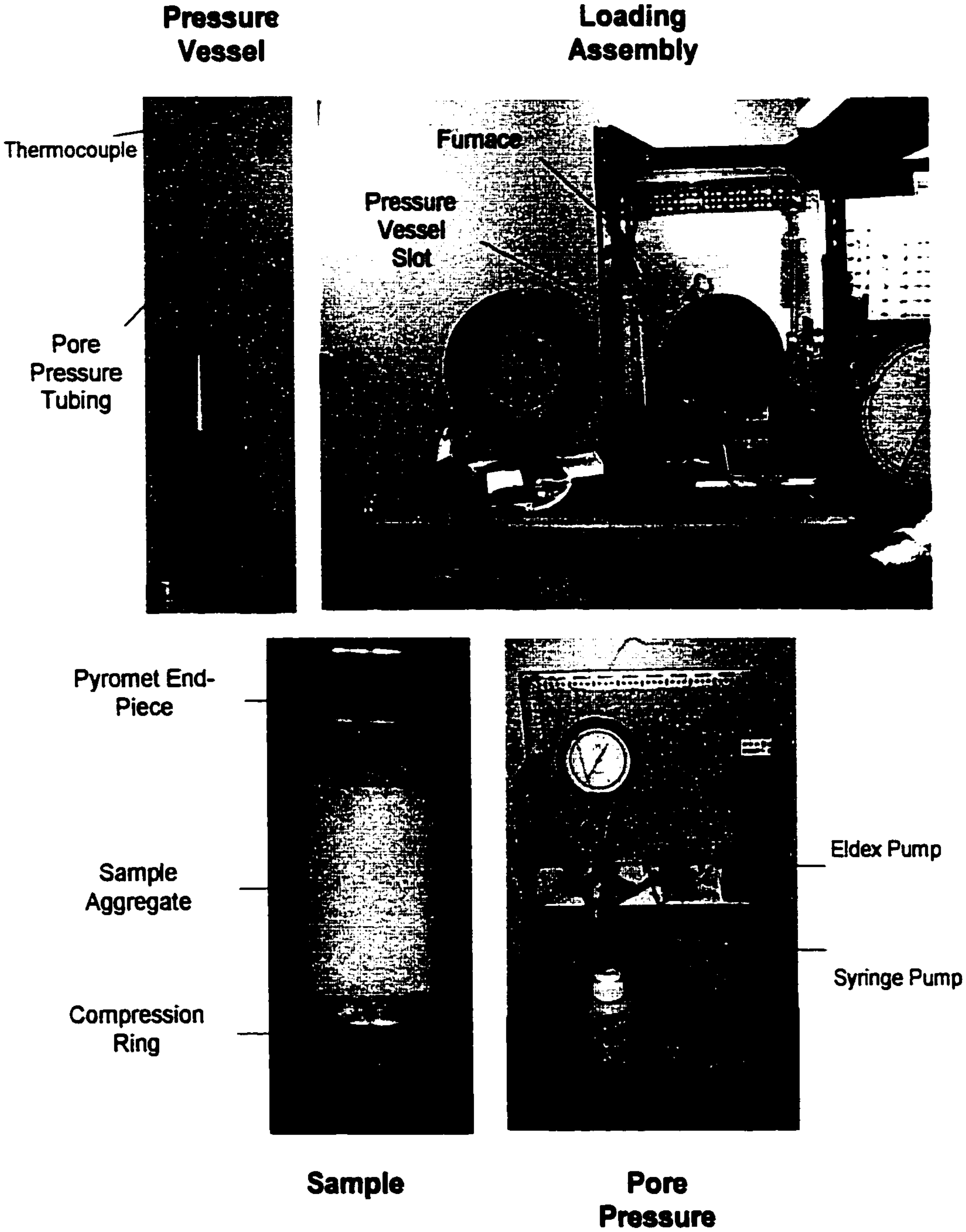

Fig. 6A.1: Photographs of the parts of the creep experimental assembly showing (clockwise from top left) the pressure vessel (15 cm across at the bottom), loading assembly, pore pressure system and the sample (2.5 cm across).

Chapter 7

Conclusions

Apparently diverse topics such as behavior of fault gouge and transformation of high-porosity unconsolidated sediments into lower-porosity lithified rock deal with multiple time-dependent, fluid mediated deformation mechanisms. The regeneration of strength in fault rocks and its subsequent breakdown is a function of interactions of the relative rates of mechanical (generally time-independent) and chemical processes. The response of granular media to stresses, temperature and fluids prevailing in the earth's crust is central to evolution of strength, petrophysical and textural characteristics. Various aspects of time-dependent deformation of granular aggregates in the presence of a pore fluid were investigated in this study either in bulk aggregate creep experiments or as synthetic fault zones composed of country rock enclosing fault gouge. The major conclusions have been summarized below.

1. Wet granular creep in quartz, halite, gypsum from the literature coupled with new data on creep of calcite aggregates under isotropic loading at low effective pressures exhibit similar functional dependencies in spite of the differences in solubility or physical properties. The same empirical rate law was successfully applied to all four minerals. Volume strain in these experiments is accommodated as a logarithmic function of time.

The strain rate shows an exponential dependence on effective pressure and an inverse dependence on grain size raised to the exponent 2.3 for all four minerals.

2. A series of long-term (up to two months), hold-slide-hold experiments using precut Berea sandstone forcing members and natural gypsum gouge were conducted to investigate strength evolution as a function of hold time and strengthening mechanisms. Experiments with water-saturated gouge display: (a) systematic increase of gouge shear strength; (b) unstable yielding and associated large stress drops; (c) common evidence for cementation, crack sealing, recrystallization, porosity reduction and grain welding in gouge loaded for long hold times; and (d) non-linear time-dependent increase of stress drop magnitudes. All these features were absent in identical tests with dry gypsum gouge. Gypsum was used as an analogue material but the dissolution rates for gypsum at room temperature and quartz at 300°C are within two orders of magnitude. Recent field and experimental evidence suggest that crustal faults heal in a rapid but time-dependent manner following large seismic events. The results from experiments reported here coupled with evidence of rapid time-dependent strengthening associated with crustal earthquakes suggest that earthquake nucleation and rupture may be essentially similar to rupture of intact rocks. Immediately after a seismic event rates for time-dependent deformation mechanisms such as pressure solution, Ostwald ripening and crack sealing are higher

(chapters 2, 3, 5 and 6). This leads to a strengthening via modifications of grain texture (grain contact welding, suturing etc.) coupled with reduction in porosity. However, due to the non-linear nature of the above mechanisms their rates tend to become lower during the inter-seismic periods. As the relative rates of tectonic loading and cementation along fault zones approach one-another rupture nucleation and propagation may take place resulting in earthquakes. This model for earthquake mechanics has been schematically illustrated in Figure 7.1.

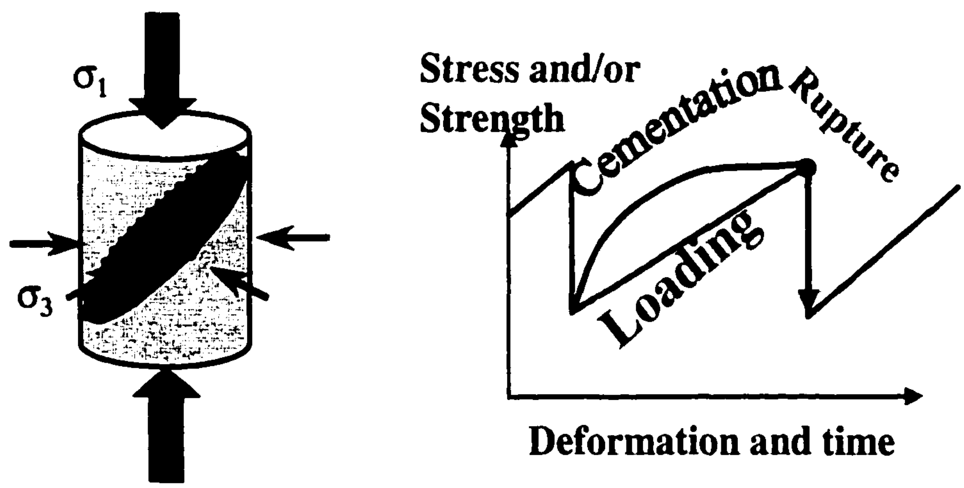

Fig. 7.1: Schematic illustration of a conceptual model for earthquake nucleation based on results reported in the study. Immediately after a seismic event cementation rates are higher than tectonic loading rates and impart mechanical strength to the fault zone. The rates of individual deformation mechanisms such as compaction, pressure solution and Ostwald ripening are high initially but tend to become lower with inter-seismic time. As the rates of cementation and tectonic loading approach each other earthquake rupture may nucleate.

3. Identical deformation mechanisms influences both strengthening of fault zones as well as promotes fault sealing. The influence of time-dependent deformation mechanisms in altering the permeability characteristics in fault zones was evaluated. Common models of fault seal development in hydrocarbon reservoirs are based on juxtaposition of sand and shale or due to cataclastic gouge generation. A large number of seals in hydrocarbon provinces worldwide are formed where reservoir units are juxtaposed. Experiments conducted in this study suggest that deformation mechanisms such as pressure solution, crack sealing and recrystallization can reduce fault zone permeability. This reduction may be at times more efficient than that entirely due to mechanical processes. These mechanisms can generate the cement sufficient to cause fault sealing and no influx of external solute laden fluids is necessary.
4. Slide-hold experiments were conducted using gypsum as fault gouge to investigate the contrasting signatures of shear- and time-dependent particle size distribution (PSD) evolution. Increasing shear resulted in an overall fining PSD evolution trend characterized by: (a) decrease in mean, (b) increase in spread and skewness and (c) an increase in the fractal dimension. Fractal dimensions around 2.6 obtained from these experiments are similar to those previously obtained in other experimental and field investigations. Time-dependent PSD evolution exhibits a coarsening trend as evident from: (a) increase in mean, (b)

increase in spread and skewness and, (c) a decrease in fractal dimension. Ostwald ripening appears to be the dominant mechanism responsible for the time-dependent PSD coarsening as suggested by a preferential consumption of the finest particle size fractions (< 5 μm). Destruction of fault zone porosity during inter-seismic creep due to such recrystallization may explain fault zone strengthening. A time-dependent coarsening is not accounted for in prevailing models relating frictional parameters such as the critical slip distance to radius of slip nucleus. These observations suggest larger slip nuclei may result solely from PSD coarsening.

5. Hydrostatic creep of granular calcite aggregates at elevated pressures and temperatures exhibit multiple deformation mechanisms. Results are in contrast to the experiments conducted at low effective pressures (chapter 2). Fracturing is the dominant mechanism at high effective pressures early in the strain history. Solution related deformation is active at elevated temperatures and high strains. Finer grain sizes generally show higher strain rates. An Arrhenius dependence of strain rate on temperature was observed for certain grain sizes. An inverse grain size exponent lower than 1 suggests a reaction controlled creep process in line with textural evidence. PSD and SEM observations indicate coarsening and lithification at elevated temperatures over long times.

Recommendations for Future Work

A conceptual model for nucleation of crustal earthquakes has been developed (Fig. 7.1) from the results of experiments conducted in this study along with evidence of fault healing from other data sources (chapter 1). In order to test this model further experimental work is needed. Hold-slide-hold experiments reported here mimic the displacement history along mature fault zones. However, slip was artificially imposed for these experiments. Slow and continuous tectonic loading can be experimentally duplicated by slow and constant displacement precut experiments (similar in geometry to those used here) over periods of weeks. Low displacement rates may permit artificial fault zone minerals like gypsum to strengthen considerably in the presence of reactive fluids. Due to the non-linear nature of the strengthening process slip instability (rupture) may nucleate in a manner similar to that schematically presented in Figure 7.1 when the loading and cementation rates are comparable. Significantly higher displacement rates would exhibit stable sliding behavior without any observable slip instability.

This study was aimed at investigating the basic mechanics of strengthening in crustal fault zones due to mineral-water interaction. Multiple deformation mechanisms with distinct driving forces and rates that could cause re-strengthening were identified. A growing body of evidence from diverse data sources is documenting rapid, time-dependent, post-seismic healing in the vicinity of active fault zones. Mechanisms and phenomenology of fault strengthening obtained from this study may further the understanding of the earthquake process by relating laboratory observations to field data. Future work aimed at investigation of active fault zones to determine healing rates from independent remote sensing (seismic, radar and GPS) methods or high-resolution dating techniques on fault zones cements are needed to test the applicability of the laboratory results presented here. Progress in work on the Nojima fault in Japan with impending work on drilling the San Andreas promises to generate data that can be used to test hypothesis arising out of this and other experimental work.